The Astrophysical Journal Supplement Series, 229:28 (42pp), 2017 April https://doi.org/10.3847/1538-4365/229/2/28

Star Formation In Nearby Clouds (SFiNCs): X-Ray and Infrared Source Catalogs and Membership

Konstantin V. Getman[1], Patrick S. Broos[1], Michael A. Kuhn[2,3], Eric D. Feigelson[1], Alexander J. W. Richert[1], Yosuke Ota[1], Matthew R. Bate[4], and Gordon P. Garmire[5]
[1] Department of Astronomy & Astrophysics, 525 Davey Laboratory, Pennsylvania State University, University Park, PA 16802, USA
[2] Instituto de Fisica y Astronomia, Universidad de Valparaiso, Gran Bretana 1111, Playa Ancha, Valparaiso, Chile; Millennium Institute of Astrophysics, MAS, Chile
[3] Millenium Institute of Astrophysics, Avenue Vicuna Mackenna 4860, 782-0436 Macul, Santiago, Chile
[4] Department of Physics and Astronomy, University of Exeter, Stocker Road, Exeter, Devon EX4 4SB, UK
[5] Huntingdon Institute for X-Ray Astronomy, LLC, 10677 Franks Road, Huntingdon, PA 16652, USA

Received 2016 June 7; revised 2016 December 2; accepted 2016 December 15; published 2017 March 29

Abstract

The Star Formation in Nearby Clouds (SFiNCs) project is aimed at providing a detailed study of the young stellar populations and of star cluster formation in the nearby 22 star-forming regions (SFRs) for comparison with our earlier MYStIX survey of richer, more distant clusters. As a foundation for the SFiNCs science studies, here, homogeneous data analyses of the *Chandra* X-ray and *Spitzer* mid-infrared archival SFiNCs data are described, and the resulting catalogs of over 15,300 X-ray and over 1,630,000 mid-infrared point sources are presented. On the basis of their X-ray/infrared properties and spatial distributions, nearly 8500 point sources have been identified as probable young stellar members of the SFiNCs regions. Compared to the existing X-ray/mid-infrared publications, the SFiNCs member list increases the census of YSO members by 6%–200% for individual SFRs and by 40% for the merged sample of all 22 SFiNCs SFRs.

Key words: infrared: stars – open clusters and associations: general – stars: early-type – stars: formation – stars: pre-main sequence – X-rays: stars

Supporting material: figure sets, machine-readable tables

1. Introduction

1.1. Motivation for SFiNCs

Most stars today, like our Sun, are field stars. Yet, examination of star formation in molecular clouds shows that most form in compact bound clusters with 10^2–10^4 members (Lada & Lada 2003) or in distributed, unbound stellar associations (Kruijssen 2012). Most young stellar structures rapidly disperse, often when the gravitational potential decreases due to the dispersal of the molecular cloud material (Tutukov 1978; Hills 1980) or due to the tidal interactions with other giant molecular clouds (Kruijssen et al. 2012). Although these basic concepts seem physically reasonable, we have a poor empirical characterization, and hence an uncertain astrophysical understanding of the detailed processes of cluster formation and early evolution. Do clusters form "top-down," rapidly in a dense molecular cloud core (Clarke et al. 2000)? Or, since clouds are turbulent, do clusters form "bottom-up" by merging subclusters produced in small kinematically distinct molecular structures (Bonnell et al. 2003; McMillan et al. 2007; Bate 2009)? Do clusters principally form in elongated molecular structures such as cold infrared dark clouds (Krumholz & Tan 2007) and filaments found to be pervasive in giant molecular clouds by the Herschel satellite (André et al. 2010)? Do massive stars form early in the life cycle of a stellar cluster or are they the last to form, halting further star formation (Zinnecker & Yorke 2007)? How important is the role of the feedback by young stars (such as protostellar outflows) or, for the more massive clusters with hot OB stars, by ultraviolet radiation and stellar winds on star cluster formation processes (Krumholz et al. 2014)?

One of the central reasons for slow progress in resolving these questions is the lack of homogeneous and reliable census of young stellar object (YSO) members for a wide range of star-forming environments. Early studies focused on stars with Hα emission (which arises in accreting columns) and/or photometric variability. Such variability is due to rotational modulation of cool magnetic and hot accretion spots and variable obscuration from circumstellar dust (e.g., Herbig & Bell 1988; Herbst et al. 1994). More recent studies of young stellar populations identify the disk-bearing stellar subpopulations that are easily found through their photometric infrared (IR) excess arising from blackbody emission of the protoplanetary disk. Most studies focus on single star-forming regions (SFRs). However, due to the heterogeneity of the analysis procedures and resulting YSO data sets in such studies, it is not trivial to compare stellar populations of SFRs with different distances and absorptions.

Recent progress, by our group and others, has been made by combining the selection of young stars through the synergy of X-ray and infrared (IR) surveys. For instance, 2MASS, UKIDSS near-IR (NIR), and *Spitzer* mid-IR (MIR) surveys can cover large areas, readily identifying young Class I protostars embedded in cloud cores as well as older accreting Class II (or "classical T Tauri") stars (e.g., Gutermuth et al. 2009; Megeath et al. 2012). These IR surveys are effectively restricted to stars with IR excesses from dusty protoplanetary disks; disk-free young stars appear in the IR photometric catalogs but are indistinguishable from foreground and background Galactic field stars.

X-ray surveys have different selection criteria based on magnetic reconnection flaring near the stellar surface; they efficiently capture disk-free (Class III or "weak-lined T Tauri" stars) stars as well as a good fraction of Class I and II stars (e.g., Feigelson & Montmerle 1999; Feigelson et al. 2013). Since X-ray emission from old Galactic stars is reduced by factors of 10^{2-3} below that of pre-main sequence (PMS) stars (Preibisch & Feigelson 2005), field star contamination in the X-ray images of SFRs is significantly smaller than that of IR and optical images. Quasars, principal contaminants in nearby SFRs (Section 3.6), are easily removed by the faintness and red colors of their IR counterparts. Class III cluster members can be individually identified (e.g., Getman et al. 2011; Broos et al. 2013). An additional advantage of the X-ray surveys of young stellar clusters is that the X-ray Luminosity Function (XLF) of PMS stars is empirically found to be nearly universal and is closely linked to the stellar initial mass function (IMF; e.g., Getman et al. 2012; Kuhn et al. 2015b), so that X-ray samples obtained at a known sensitivity are roughly complete to a specific mass; albeit, the scatter in the X-ray luminosity versus mass relationship differs in various studies (Preibisch et al. 2005; Getman et al. 2006; Telleschi et al. 2007).

We are now engaged in an effort called MYStIX, Massive Young Star-forming Complex Study in Infrared and X-ray (Feigelson et al. 2013, http://astro.psu.edu/mystix). It combines a reanalysis of the *Chandra* data archive with new reductions of UKIRT+2MASS NIR and *Spitzer* MIR surveys to identify young stars in a wide range of evolutionary stages, from protostars to disk-free pre-main-sequence stars, in 20 massive SFRs at distances from 0.4 to 3.6 kpc. Stars with published spectra indicative of OB spectral types are added to the sample. Each MYStIX region was chosen to have a rich OB-dominated cluster. By combining X-ray selected and infrared-excess selected stars, and using sophisticated statistical methods to reduce field star and quasar contamination, MYStIX obtained a uniquely rich sample of >30,000 young stars in the 20 massive SFRs. MYStIX is briefly reviewed in Section 1.2.

The SFiNCs project extends the MYStIX effort to an archive study of 22 generally nearer and smaller SFRs where the stellar clusters are often dominated by a single massive star—typically a late-O or early-B—rather than by numerous O stars as in the MYStIX fields. The SFiNCs science goals are closely tied to the diverse MYStIX science program. Both projects are committed to comparative study of a reasonably large sample of SFRs with stellar populations derived from X-ray and IR surveys using uniform methodologies.

The scientific goals of SFiNCs could be simply stated: to perform analyses similar to those of MYStIX in order to examine whether the behaviors of clustered star formation are similar—or different—in smaller (SFiNCs) and giant (MYStIX) molecular clouds. The two projects together will establish, in a uniform fashion, empirical properties and correlations among properties for ∼200 subclusters, each with 10–3000 detected stars, in SFRs on scales of 0.1–30 pc. Do the SFiNC's subclusters occupy the same loci in parameter space as MYStIX subclusters? Do they show similar spatio-temporal gradients? Are certain stellar cluster properties different due to reduced turbulence in smaller molecular clouds, or are population characteristics absent in SFiNCs SFRs due to the absence of OB star feedback that play important roles in MYStIX regions? It is possible, for example, that smaller molecular clouds have less turbulence and thus produce small clusters in single events with simple structure, rather than clusters with complicated substructure suggesting subcluster mergers, as seen in many MYStIX SFRs. It is possible that smaller clusters are formed with different initial central star densities and expand at different times or rates.

1.2. *MYStIX as a Foundation for SFiNCs*

Since the SFiNCs and MYStIX programs are closely tied, it is important to review the status of the MYStIX project. The MYStIX studies will serve as the foundation for various SFiNCs efforts.

MYStIX has recently emerged with eight technical/catalog papers, seven published science papers, and two science papers that are nearing completion. The technical papers, reviewed in Feigelson et al. (2013), describe the following innovative methods designed for crowded and nebular star-forming regions that are often found lying near the Galactic Plane: *Chandra* X-ray, *Spitzer* MIR, UKIRT NIR data reduction (King et al. 2013; Kuhn et al. 2013a, 2013b; Townsley et al. 2014); X-ray/IR source matching (Naylor et al. 2013); and X-ray/IR membership classifications (Broos et al. 2013; Povich et al. 2013).

In the current work, the same MYStIX-based X-ray and MIR data analysis methods are used for the re-analyses of the archived SFiNCs *Chandra* and *Spitzer* data (Section 3). However, SFiNCs can simplify the MYStIX analysis workflow in two ways. First, since SFiNCs stars are on average brighter (due to the proximity of the SFRs) and suffer less Galactic field star contamination (due to higher Galactic latitudes), infrared counterpart identification can be achieved using traditional proximity methods. That is, the closest IR star to a *Chandra* source is a reliable counterpart in most cases (Section 3.5). The more complicated Bayesian probabilistic counterpart identification method developed for MYStIX (Naylor et al. 2013) is not needed. Second, again because field star contamination is greatly reduced, MYStIX's complex naive Bayes source classification method (Broos et al. 2013) is not needed here, and a simpler approach based on a decision tree classification is used instead (Section 4.1).

The current major MYStIX science results include: identification of over 140 MYStIX stellar subclusters and demonstration of their diverse morphologies from simple ellipsoids to elongated, clumpy substructures (Kuhn et al. 2014); development of an X-ray/IR age stellar chronometer and demonstration of spatio-age gradients on scales of ∼1–30 pc (Getman et al. 2014a); discovery of core-halo age gradients within two rich nearby clusters on scales $\leqslant 1$ pc (Getman et al. 2014b); demonstration of a universal XLF and discovery of wide ranges of the surface stellar density distribution in young stellar clusters (Kuhn et al. 2015b); demonstration of correlations among subcluster properties providing empirical signs of dynamical evolution and cluster expansion (Kuhn et al. 2015a); and no evidence for protoplanetary destruction by OB stars in the MYStIX clusters (Richert et al. 2015). Complementary to the MYStIX sample of >30,000 probable cluster members (Broos et al. 2013), Romine et al. (2016) provide the catalog of >1000 MYStIX candidate Class I protostars. The science studies on stellar mass segregation (M. A. Kuhn et al. 2017, in preparation) and the catalog of probable new OB stars (M. S. Povich et al. 2017, in preparation) are underway.

The MYStIX methods and data will be effectively used in the following future planned SFiNCs science efforts. Identification of SFiNCs subclusters, derivation of their apparent properties, and comparison of these properties to those of the MYStIX subclusters; the effort is in many respects reminiscent of the MYStIX work of Kuhn et al. (2014). Examination of age gradients within the SFiNCs SFRs and subclusters; this is analogous to the MYStIX studies of Getman et al. (2014a, 2014b). Derivation of intrinsic properties of the SFiNCs subclusters, their comparison with MYStIX, and examination of implications for dynamical evolution and cluster expansion, similar to Kuhn et al. (2015a, 2015b). Revision of the longevities of protoplanetary disks using homogeneous rich data sets of ages and disk fractions for the MYStIX+SFiNCs subclusters with a proper account for stellar mass completeness and relative sensitivity to different clusters in IR and X-ray bands. Comparison of the multivariate MYStIX+SFiNCs cluster properties to astrophysical models of cluster formation and early dynamical evolution in search of empirical constraints on a variety of predictions made by theoretical models.

1.3. Outline of This Paper

As a foundation for the SFiNCs science studies, here, homogeneous data and YSO membership analyses are described and the resulting catalogs of X-ray/IR point sources and YSO members of the SFiNCs SFRs are presented. The SFiNCs sample is introduced in Section 2. The paper further describes *Chandra*-ACIS X-ray and *Spitzer*-IRAC MIR observations and their data reduction, source detection and characterization (Section 3), cross matching among the 2MASS NIR, IRAC, and ACIS source catalogs (Section 3.5). These are followed by disk classification and YSO membership (Section 4.1), spatial distribution of the YSOs (Section 4.3), IR/optical diagrams and global properties of the YSOs (Sections 4.4, 4.5), comparison between bright and faint X-ray YSOs (Section 4.6), and comparison with the previous member lists from the literature (Section 5). Extensive tables of the SFiNCs X-ray/IR sources and YSO members and their properties, as well as a visual atlas with various YSO's characteristics (Appendix B) are provided. Other SFiNCs papers will discuss various science issues emerging from these data.

2. SFiNCs Sample Selection

The *Chandra X-ray Observatory* mission has observed several dozen SFRs in the nearby Galaxy. A large portion of massive SFRs with typical distances in the range 0.4 to 3.6 kpc was treated in MYStIX (Table 1 in Feigelson et al. 2013). Here we have selected 22 generally smaller SFRs with the following criteria: nearby $0.2 < d \lesssim 1$ kpc; young (cluster ages $\lesssim 10$ Myr, when estimated); populations typically dominated by B-type stars; archived *Chandra* observations sensitive (but not complete) down to $\log(L_X) \lesssim 29.5$ erg s^{-1} corresponding to PMS stars with $\lesssim 0.3\ M_\odot$; archived *Spitzer*-IRAC data are available. The properties of the 22 SFiNCs targets are given in Table 1. Note that we do not set a criterion based on obscuration because the X-ray emission of many (although not all) young stars is often hard enough to penetrate $A_V > 10$–20 mag of obscuration, which is comparable to that of the NIR 2MASS survey. Half of our targets are in the Lada & Lada (2003) catalog of nearby embedded star clusters. Unlike the MYStIX SFRs, all but two SFiNCs SFRs lie away from the Galactic Plane. Note that as for MYStIX (Table 1 in Feigelson et al. 2013), here we omit reporting heterogeneous SFiNCs age estimates published in the literature. A homogeneous set of median ages for individual SFiNCs clusters, using the cluster and age methods of Kuhn et al. (2014) and Getman et al. (2014a), will be reported in a future SFiNCs publication.

The nearest ($d < 0.2$ kpc) SFRs are omitted from SFiNCs because on the sky they often subtend areas much greater than the *Chandra* detector. Excellent *Chandra* exposures are available for the two cluster regions in the Perseus cloud, IC 348 and NGC 1333 at ~300 pc. Two single exposures are available for the Serpens core cloud and Serpens South cluster; both are parts of the Serpens-Aquila Rift region at ~400 pc. We proceed to the Orion clouds at a distance of ~400 pc. Single *Chandra* exposures are available for the regions adjacent to the Orion Nebula Cluster (ONC) in the Orion A cloud (ONC Flank S, ONC Flank N, and OMC 2-3). Multiple *Chandra* exposures/pointings exist for the NGC 2068-2071 complex in the Orion B cloud. Two famous rich clusters in the Orion region, ONC and Flame Nebula, are in the MYStIX sample. Two parts of the Monoceros R2 cloud (Mon R2 and GGD 12-15) at a distance of ~800 pc are covered by single *Chandra* exposures. Three parts of the large Cepheus cloud (Cep OB3b, Cep A, and Cep C) at a distance of ~700 pc and two parts of the large Cepheus Loop H II bubble (NGC 7822 and IRAS 00013+6817) at a distance of ~900 pc are covered, as well as a variety of isolated SFRs.

3. *Chandra*-ACIS and *Spitzer*-IRAC Observations and Data Reduction

3.1. X-Ray Data

For many SFiNCs SFRs, the *Chandra Source Catalog* (CSC; current release version 1.1[6]) provides catalogs of X-ray point sources and their X-ray properties. However, the CSC v1.1 is limited to relatively bright X-ray sources and does not adequately treat multiple ObsID mosaics. Our experience with MYStIX (Feigelson et al. 2013; Kuhn et al. 2013a) suggested that our SFiNCs X-ray catalogs would have 2–3 times the population as the CSC v1.1. We do not use published X-ray source catalogs either, because they were produced with heterogeneous methods that are often less sensitive to point sources than the MYStIX-based methods (see Section 4 in Kuhn et al. 2013a), and they often do not provide the absorption and X-ray luminosity measurements for faint X-ray PMS stars needed for our age and population analyses. Instead, we opted to re-analyze the archive *Chandra* data using the MYStIX-based methods.

Sixty five X-ray observations for the 22 SFiNCs SFRs, made with the imaging array on the Advanced CCD Imaging Spectrometer (ACIS Weisskopf et al. 2002; Garmire et al. 2003), were pulled from the *Chandra* archive.[7] The details on these observations are provided in Table 2. For half of the SFiNCs regions, multiple observations, often with multiple pointings, were collected. The left panels in Figure 1 present the low-resolution adaptively smoothed images of these mosaicked *Chandra*-ACIS exposures. The broadening of the X-ray point sources at the halos of the SFiNCs fields is due to the considerable degradation of the *Chandra* telescope point-spread function (PSF) far off-axis. A typical net exposure time for a single SFiNCs pointing ranges between 50 and 100 ks. All observations but one (ObsID 6401) were taken in the

---

[6] Current release version, v1.1, of the *Chandra* Source Catalog is available at http://cxc.cfa.harvard.edu/csc1/. The production of the release v2.0 is in progress, http://cxc.cfa.harvard.edu/csc2/.

[7] http://cxc.cfa.harvard.edu/cda/

Table 1
SFiNCs Star-forming Regions

Name (1)	R.A.(J2000) h:m:s (2)	Decl.(J2000) °:′:″ (3)	l deg (4)	b deg (5)	D pc (6)	Dist. Ref. (7)	OB (8)	*Spitzer* Ref. (9)	*Chandra* Ref. (10)
NGC 7822 (Be59)	00:02:15.27	+67:25:59.7	118.2262	5.0120	900	Ma08;Pa08	O5V	…	…
IRAS 00013+6817 (SFO 2)	00:04:03.85	+68:33:33.7	118.6050	6.0865	900	Ma08;Pa08	…	Gu09	…
NGC 1333	03:29:04.76	+31:20:10.7	158.3063	−20.4982	235	Hi08	B5V	Gu09	Wi10
IC 348	03:44:30.30	+32:07:44.8	160.5025	−17.8368	300	He08	B5V	Lu16	St12
LkHα 101	04:30:09.86	+35:16:09.2	165.3491	−9.0203	510	Wo10	B4	Gu09	Wo10
NGC 2068-2071	05:46:43.54	+00:07:34.2	205.2813	−14.2981	414	Me07	B2/3	Me12	Gr04;Sk09
ONC Flank S	05:35:05.79	−05:39:07.9	209.2379	−19.5421	414	Me07	B9V	Me12	Ra04
ONC Flank N	05:35:14.38	−04:49:49.5	208.4786	−19.1380	414	Me07	B1V	Me12	Ra04
OMC 2-3	05:35:23.44	−05:07:03.1	208.7676	−19.2349	414	Me07	B0.5V	Me12	Ts02
Mon R2	06:07:46.15	−06:22:53.6	213.7009	−12.6029	830	Ra68	B0	Gu09	Na03
GGD 12-15	06:10:49.51	−06:11:45.7	213.8772	−11.8404	830	Ra68	B8/A0	Gu09	…
RCW 120	17:12:23.25	−38:28:45.4	348.2381	0.4639	1350	Za07	O9:	…	…
Serpens Main	18:29:56.30	+01:13:11.5	31.5647	5.3394	415	Dz10	…	Gu09	Gi07;Wi07
Serpens South	18:30:02.56	−02:03:42.2	28.6501	3.8133	415	Dz10	…	Po13	…
IRAS 20050+2720	20:07:06.56	+27:30:02.3	65.7962	−2.6014	700	Wi89	B3	Gu09	Gu12
Sh 2-106	20:27:24.36	+37:22:54.9	76.3802	−0.6137	1400	No05;Sc07	B0V	Gu09	Gi04
IC 5146	21:53:29.82	+47:15:22.4	94.3896	−5.5133	800	Ga14	B2V	Gu09	…
NGC 7160	21:53:49.98	+62:35:10.2	104.0159	6.4318	870	Co02	B0.5V	Si06	…
LDN 1251B	22:38:48.05	+75:11:50.4	114.6324	14.5068	300	Ku08	…	Ev03	Si09
Cep OB3b	22:55:39.32	+62:38:11.2	110.0643	2.6936	700	Mo09;Dz11	O7V	Al12	Ge06;Al12
Cep A	22:56:14.13	+62:02:17.8	109.8676	2.1246	700	Mo09;Dz11	O9V	Gu09	Pr09
Cep C	23:05:49.42	+62:30:27.2	111.0778	2.0919	700	Mo09;Dz11	B9:	Gu09	…

Note. Column 1: SFR name. Columns 2–5: Coordinates: R.A., decl., Galactic longitude, and Galactic latitude. Column 6: distance from the Sun in parsecs. Column 7: literature reference to the distance value. Column 8: the earliest OB star within the *Chandra* field from the catalogs of Skiff (2009) and SIMBAD. Columns 9–10: literature references to the previous *Spitzer* and *Chandra* studies of the region. Reference code in Columns 7, 9, and 10: Al12 (Allen et al. 2012), Co02 (Contreras et al. 2002), Dz10 (Dzib et al. 2010), Dz11 (Dzib et al. 2011), Ev03 (Evans et al. 2003), Ga14 (García-Rojas et al. 2014), Ge06 (Getman et al. 2006), Gi04 (Giardino et al. 2004), Gi07 (Giardino et al. 2007), Gr04 (Grosso et al. 2004), Gu09 (Gutermuth et al. 2009), Gu12 (Günther et al. 2012), He08 (Herbst 2008), Hi08 (Hirota et al. 2008), Ku08 (Kun et al. 2008), Lu16 (Luhman et al. 2016), Ma08 (Majaess et al. 2008), Me07 (Menten et al. 2007), Me12 (Megeath et al. 2012), Mo09 (Moscadelli et al. 2009), Na03 (Nakajima et al. 2003), No05 (Noel et al. 2005), Pa08 (Pandey et al. 2008), Po13 (Povich et al. 2013), Pr09 (Pravdo et al. 2009), Ra68 (Racine 1968), Ra04 (Ramírez et al. 2004), Sc07 (Schneider et al. 2007), Si06 (Sicilia-Aguilar et al. 2006),Si09 (Simon 2009), Sk09 (Skinner et al. 2009), St12 (Stelzer et al. 2012), Ts02 (Tsujimoto et al. 2002), Wi89 (Wilking et al. 1989), Wi07 (Winston et al. 2007), Wi10 (Winston et al. 2010), Wo10 (Wolk et al. 2010), and Za07 (Zavagno et al. 2007).

imaging mode with the imaging array ACIS-I, an array of four abutted 1024 × 1024 pixel front-side illuminated charge-coupled devices (CCDs) covering about 17′ × 17′ on the sky; the aimpoints for these observations are located on the I3 chip. In some of these observations, the S2 and/or S3 chips from the spectroscopic ACIS-S array were also operational. One observation (ObsID 6401 for IC 5146) was taken in the imaging mode with the aimpoint located on the S3 chip; in this case the S2 and all ACIS-I chips were turned on as well.

Our X-ray data reduction follows the procedures described in detail by the MYStIX studies of Kuhn et al. (2013a), Townsley et al. (2014), and earlier studies of Broos et al. (2010, 2011). The Level 1 processed event lists provided by the pipeline processing at the *Chandra* X-ray Center were calibrated and cleaned using mostly standard methods and tools. Briefly, using the tool *acis_process_events* from the CIAO version 4.6, the latest calibration information (CALDB 4.6.2) on time-dependent gain and our custom bad pixel mask (Section 3 in Broos et al. 2010) are applied; background event candidates are identified. Using the *acis_detect_afterglow* tool, additional afterglow events not detected with the standard *Chandra* X-ray Center (CXC) pipeline are flagged. The event list is cleaned by "grade" (only ASCA grades 0, 2, 3, 4, and 6 are accepted), "status," "good-time interval," and energy filters. The slight PSF broadening from the CXC software position randomizations is removed. Instrumental background events were identified and removed using an aggressive algorithm when searching for sources and using an algorithm with few false positives when extracting sources (Section 3 in Broos et al. 2010). Event positions were adjusted to better align with the 2MASS catalog (Skrutskie et al. 2006).

Detection of candidate point sources is performed using two methods, the wavelet transform method (Freeman et al. 2002) and the maximum likelihood image deconvolution with local PSFs (see Section 4.2 in Broos et al. 2010); the latter is better suited for resolving closely spaced sources. Source photon extraction and characterization from multi-ObsID ACIS data based on local PSFs, and updated position estimates were obtained for candidate sources using the *ACIS Extract* (*AE*; Broos et al. 2010, 2012) software package.[8] Through numerous iterations over spatially crowded source candidates, *AE* produces optimal source and background extraction regions; and based on Poisson statistics, *AE* calculates the probability that a source candidate is a background fluctuation (P_B). As in MYStIX, here the SFiNCs *Chandra* catalog retains all X-ray point sources for which $P_B < 1\%$; this criterion sometimes results in on-axis X-ray sources with as few as three net counts.

---

[8] The *ACIS Extract* software package and User's Guide are available at http://www2.astro.psu.edu/xray/docs/TARA/ae_users_guide.html.

Table 2
Log of SFiNCs *Chandra*-ACIS Observations

Region (1)	ObsID (2)	Sequence (3)	Start Time (UT) (4)	Exposure (s) (5)	R.A. α_{J2000} (6)	Decl. δ_{J2000} (7)	Roll (°) (8)	ACIS Mode (9)	PI (10)
NGC 7822 (Be59)	14536	200837	2014-01-14T17:52	45488	00:02:16.99	+67:25:09.0	301	VFaint	K. Getman
IRAS 00013+6817 (SFO 2)	16344	200966	2015-03-17T03:46	1841	00:04:04.69	+68:33:12.9	355	VFaint	G. Garmire
IRAS 00013+6817 (SFO 2)	17643	200966	2015-04-07T06:26	21486	00:04:04.69	+68:33:12.9	16	VFaint	G. Garmire
NGC 1333	642	200067	2000-07-12T23:15	37611	03:29:05.59	+31:19:18.9	95	Faint	E. Feigelson
NGC 1333	6436	200410	2006-07-05T15:03	36484	03:29:01.99	+31:20:53.9	94	VFaint	S. Wolk
NGC 1333	6437	200411	2006-07-11T10:25	39616	03:29:01.99	+31:20:53.9	94	VFaint	S. Wolk
IC 348	13425	200747	2011-10-17T06:12	9912	03:44:31.50	+32:08:33.6	118	VFaint	K. Flaherty
IC 348	13426	200748	2011-10-19T22:06	9912	03:44:31.50	+32:08:33.6	119	VFaint	K. Flaherty
IC 348	13427	200749	2011-10-22T13:32	9912	03:44:31.50	+32:08:33.6	121	VFaint	K. Flaherty
IC 348	13428	200750	2011-11-17T05:35	9224	03:44:31.50	+32:08:33.6	163	VFaint	K. Flaherty
IC 348	13429	200751	2011-10-28T09:53	10408	03:44:31.50	+32:08:33.6	125	VFaint	K. Flaherty
IC 348	13430	200752	2011-10-31T06:55	9912	03:44:31.50	+32:08:33.6	128	VFaint	K. Flaherty
IC 348	13431	200753	2011-11-03T09:46	9915	03:44:31.50	+32:08:33.6	132	VFaint	K. Flaherty
IC 348	13432	200754	2011-11-06T18:23	9912	03:44:31.50	+32:08:33.6	136	VFaint	K. Flaherty
IC 348	13433	200755	2011-11-10T01:36	10790	03:44:31.50	+32:08:33.6	143	VFaint	K. Flaherty
IC 348	13434	200756	2011-11-13T06:49	9911	03:44:31.50	+32:08:33.6	150	VFaint	K. Flaherty
IC 348	606	200031	2000-09-21T19:58	52285	03:44:30.00	+32:07:59.9	109	VFaint	T. Preibisch
IC 348	8584	200471	2008-03-15T09:02	49509	03:44:13.19	+32:06:00.0	288	Faint	N. Calvet
IC 348	8933	200514	2008-03-18T17:35	39632	03:43:59.89	+31:58:21.6	289	VFaint	S. Wolk
IC 348	8944	200525	2008-03-13T17:53	39142	03:43:59.89	+31:58:21.6	288	VFaint	S. Wolk
LkHα 101	5428	200361	2005-03-08T17:25	39645	04:30:14.40	+35:16:22.1	280	VFaint	S. Wolk
LkHα 101	5429	200362	2005-03-06T16:50	39651	04:30:14.40	+35:16:22.1	280	VFaint	S. Wolk
NGC 2068-2071	10763	200472	2008-11-27T22:50	19696	05:46:02.40	−00:09:00.0	43	Faint	N. Calvet
NGC 2068-2071	1872	200100	2000-10-18T05:14	93969	05:46:43.50	+00:03:29.9	79	Faint	N. Grosso
NGC 2068-2071	5382	200317	2005-04-11T01:29	18208	05:46:13.09	−00:06:05.0	261	Faint	J. Kastner
NGC 2068-2071	5383	200318	2005-08-27T14:31	19879	05:46:13.09	−00:06:05.0	100	Faint	J. Kastner
NGC 2068-2071	5384	200319	2005-12-09T14:48	19702	05:46:13.09	−00:06:05.0	22	Faint	J. Kastner
NGC 2068-2071	6413	200388	2005-12-14T15:45	18100	05:46:13.09	−00:06:05.0	10	Faint	J. Kastner
NGC 2068-2071	6414	200389	2006-05-01T03:45	21648	05:46:13.09	−00:06:05.0	250	Faint	J. Kastner
NGC 2068-2071	6415	200390	2006-08-07T18:23	20454	05:46:13.09	−00:06:05.0	110	Faint	J. Kastner
NGC 2068-2071	7417	200430	2007-11-06T19:40	67178	05:47:04.79	+00:21:42.8	68	Faint	S. Skinner
NGC 2068-2071	8585	200472	2008-11-28T12:15	28470	05:46:02.40	−00:09:00.0	43	Faint	N. Calvet
NGC 2068-2071	9915	200531	2008-09-18T04:03	19895	05:46:13.09	−00:06:04.7	91	Faint	D. Weintraub
NGC 2068-2071	9916	200532	2009-01-23T03:58	18405	05:46:13.09	−00:06:04.7	299	Faint	D. Weintraub
NGC 2068-2071	9917	200533	2009-04-21T16:18	29784	05:46:13.09	−00:06:04.7	255	Faint	D. Weintraub
ONC Flank S	2548	200156	2002-09-06T12:57	46759	05:35:05.59	−05:41:04.7	101	Faint	J. Stauffer
ONC Flank N	2549	200157	2002-08-26T13:49	48804	05:35:19.09	−04:48:31.3	102	Faint	J. Stauffer
OMC 2-3	634	200059	2000-01-01T13:05	79647	05:35:19.97	−05:05:29.8	329	Faint	K. Koyama
Mon R2	1882	200110	2000-12-02T23:14	96364	06:07:49.49	−06:22:54.6	37	Faint	K. Koyama
GGD 12-15	12392	200726	2010-12-15T14:05	67317	06:10:49.99	−06:12:00.0	18	VFaint	J. Forbrich
RCW 120	13276	200746	2013-02-11T07:39	29688	17:12:20.80	−38:29:30.5	93	VFaint	G. Garmire
RCW 120	13621	200775	2012-06-30T12:28	49117	17:12:20.80	−38:29:30.5	303	VFaint	K. Getman
Serpens Main	4479	200248	2004-06-19T21:42	88449	18:29:49.99	+01:15:29.9	161	Faint	F. Favata
Serpens South	11013	200642	2010-06-07T23:39	97485	18:30:02.99	−02:01:58.1	136	Faint	E. Winston
IRAS 20050+2720	6438	200412	2006-12-10T02:35	22669	20:07:13.60	+27:28:48.7	314	VFaint	S. Wolk
IRAS 20050+2720	7254	200412	2006-01-07T19:48	20852	20:07:13.60	+27:28:48.7	344	VFaint	S. Wolk
IRAS 20050+2720	8492	200412	2007-01-29T03:53	50481	20:07:13.60	+27:28:48.7	12	VFaint	S. Wolk
Sh 2-106	1893	200121	2001-11-03T00:08	44384	20:27:25.49	+37:22:48.6	283	Faint	Y. Maeda
IC 5146	15723	200936	2015-02-24T18:06	37468	21:53:30.30	+47:16:03.6	10	VFaint	M. Kuhn
IC 5146	6401	200378	2006-02-22T08:12	26571	21:52:34.09	+47:13:43.6	8	Faint	B. Stelzer
NGC 7160	10818	200519	2008-11-21T13:00	20685	21:53:47.99	+62:36:00.0	278	Faint	J. Miller
NGC 7160	10819	200519	2008-11-22T12:26	14761	21:53:47.99	+62:36:00.0	278	Faint	J. Miller
NGC 7160	10820	200519	2008-11-23T03:59	15746	21:53:47.99	+62:36:00.0	278	Faint	J. Miller
NGC 7160	8938	200519	2008-11-18T22:42	18021	21:53:47.99	+62:36:00.0	278	Faint	J. Miller
LDN 1251B	7415	200428	2007-08-11T13:05	29664	22:38:46.99	+75:11:30.0	161	VFaint	T. Simon
LDN 1251B	8588	200428	2007-08-10T10:46	27982	22:38:46.99	+75:11:30.0	161	VFaint	T. Simon
Cep OB3b	10809	200536	2009-04-04T12:49	21323	22:55:47.50	+62:38:10.2	34	VFaint	T. Allen
Cep OB3b	10810	200536	2009-05-07T20:34	22852	22:55:47.50	+62:38:10.2	71	VFaint	T. Allen
Cep OB3b	10811	200535	2009-04-28T07:05	24405	22:53:31.69	+62:35:33.3	63	VFaint	T. Allen
Cep OB3b	10812	200535	2009-05-03T01:48	24814	22:53:31.69	+62:35:33.3	63	VFaint	T. Allen
Cep OB3b	3502	200197	2003-03-11T12:21	30090	22:56:46.99	+62:40:00.0	7	Faint	G. Garmire
Cep OB3b	9919	200535	2009-05-08T03:29	22465	22:53:31.69	+62:35:33.3	68	VFaint	T. Allen

Table 2
(Continued)

Region (1)	ObsID (2)	Sequence (3)	Start Time (UT) (4)	Exposure (s) (5)	R.A. α_{J2000} (6)	Decl. δ_{J2000} (7)	Roll (°) (8)	ACIS Mode (9)	PI (10)
Cep OB3b	9920	200536	2009-04-16T10:45	27682	22:55:47.50	+62:38:10.2	47	VFaint	T. Allen
Cep A	8898	200479	2008-04-08T12:13	77953	22:56:19.84	+62:01:46.9	39	Faint	S. Pravdo
Cep C	10934	200570	2010-09-21T10:42	43989	23:05:50.99	+62:30:55.0	193	Faint	K. Covey

Note. Column 1: SFR name, sorted by R.A. Columns 2–3: *Chandra* observation id and sequence number. Column 4: start time of a *Chandra* observation. Column 5: exposure time is the net usable time after various filtering steps are applied in the data reduction process. Columns 6–7: the aimpoint of a *Chandra* observation is obtained from the satellite aspect solution before astrometric correction is applied. Units of R.A. are hours, minutes, and seconds; units of decl. are degrees, arcminutes, and arcseconds. Column 8: roll angle of a *Chandra* observation. Column 9: *Chandra*-ACIS observing mode. The ACIS modes are described in Section 6.12 of *Chandra* Proposers' Observatory Guide, http://asc.harvard.edu/proposer/POG/. Column 10: the principal investigator of a *Chandra* observation.

3.2. X-Ray Source Catalog

Our final *Chandra*-ACIS catalog for the 22 SFiNCs SFRs comprises 15364 X-ray sources (Table 3). The *AE* package provides a variety of source characteristics, including celestial position, off-axis angle, net and background counts, fraction of the PSF enclosed within the extraction region, source significance and probability for a source being a background fluctuation assuming Poisson statistics, a variability indicator extracted from the one-sided Kolmogorov–Smirnov test, median energy after background subtraction, and occasional anomalies related to chip gap, filed edge positions, photon pile-up, location on a readout streak, and a possible contamination by afterglow events.

It has to be stressed here that our deliberately aggressive strategy of pushing the X-ray source detection down to three net counts on-axis, similar to that of the MYStIX (Kuhn et al. 2013a; Townsley et al. 2014) and earlier CCCP (Broos et al. 2011; Townsley et al. 2011, *Chandra* Carina Complex Project) projects, produces most sensitive X-ray source catalogs. For instance, the comparison between the SFiNCs and previously published X-ray catalogs, which are available for 13 SFiNCs SFRs (Appendix A and Table 10), indicates that the number of X-ray sources in SFiNCs is typically by a factor of >3 higher than that in the earlier studies. The X-ray color–magnitude diagrams presented further in Section 4.6 suggest that the vast majority of the newly discovered faint X-ray sources have hard X-ray spectra (median energy above 2–3 keV), characteristic of active galactic nuclei (AGNs) or highly absorbed YSOs. Older background stars in the high-Galactic latitude SFiNCs SFRs would generally contribute only a small fraction to these weak, extremely hard X-ray sources (Figure 2 in Broos et al. 2013). But the MYStIX, CCCP, and SFiNCs catalogs are undoubtedly subject to contamination by faint spurious X-ray sources. This choice is obvious—by producing the most sensitive X-ray catalogs we aim at identifying larger numbers of faint X-ray sources with IR counterparts, many of which would be new low-mass and/or highly absorbed YSO members of star-forming regions. Our choice of a threshold of $P_B < 1\%$ for detection has been justified in previous studies of the Carina Nebula star-forming complex, in which the number of X-ray sources, both with and without IR counterparts, increased smoothly (without jumps) as the threshold was increased (see Figure 9 in Broos et al. 2011). Similar trends are seen in MYStIX (Kuhn et al. 2013a). Due to the complexity of our X-ray methods (a fusion of two source detection methods, iterative background optimization, and extraction from multi-ObsID ACIS data) a simulation aimed at estimating the fraction of spurious X-ray sources is deemed to be infeasible (Section 6.2 in Broos et al. 2011). Nevertheless, the comparison of the numbers of the simulated Galactic field and extragalactic X-ray contaminants with the numbers of the observed X-ray non-members for the MYStIX fields suggest that the fraction of the spurious X-ray sources in our X-ray catalogs is likely below a few-tens of percent (see Table 8 in Broos et al. 2013).

Another caveat pertain to our methods of detecting and identifying X-ray sources and to the resulting SFiNCs as well as MYStIX and CCCP X-ray catalogs. The very weak X-ray sources often tend to concentrate toward the central parts of *Chandra*-ACIS fields producing a ring-shaped spatial distribution. This, so called "egg-crate" effect, is due to the variation in detection completeness with off-axis angle (Broos et al. 2011). Our simulations of the MYStIX extragalactic X-ray contaminants successfully reproduced such a distribution (see Figure 6 (f) in Broos et al. 2013).

The X-ray fluxes and absorbing column densities of the SFiNCs X-ray sources are generated using the non-parametric method *XPHOT* (Getman et al. 2010). The concept of the method is similar to the long-standing use of color–magnitude diagrams in optical and infrared astronomy, with X-ray median energy replacing color index and X-ray source counts replacing magnitude. Empirical X-ray spectral templates derived from bright sources from the *Chandra* Orion Ultradeep Project (COUP; Getman et al. 2005) are further used to translate apparent photometric properties of weak PMS stars into their intrinsic properties. The advantage of the *XPHOT* method over a traditional parametric spectral modeling is that it is more accurate for very faint sources and provides both statistical and systematic (due to uncertainty in X-ray model) errors on derived intrinsic fluxes and absorptions. *XPHOT* allows a recovery of the soft ($\lesssim$1 keV) X-ray plasma component, which is often missed in the X-ray data of weak and/or highly absorbed sources when using traditional methods of parametric model fitting. The comparison of the *XPHOT* fluxes and column densities with the previously published X-ray fluxes and densities (Appendix A) supports these notions: the number of faint X-ray sources with available flux estimates in SFiNCs is higher than that in the previous catalogs; and the SFiNCs *XPHOT* fluxes are systematically higher than the earlier published X-ray fluxes.

The incident photon fluxes produced by *AE* and the apparent/intrinsic X-ray fluxes and absorbing column densities produced by *XPHOT* are given in Table 4. Since *XPHOT* assumes the X-ray spectral shapes of young, low-mass stars,

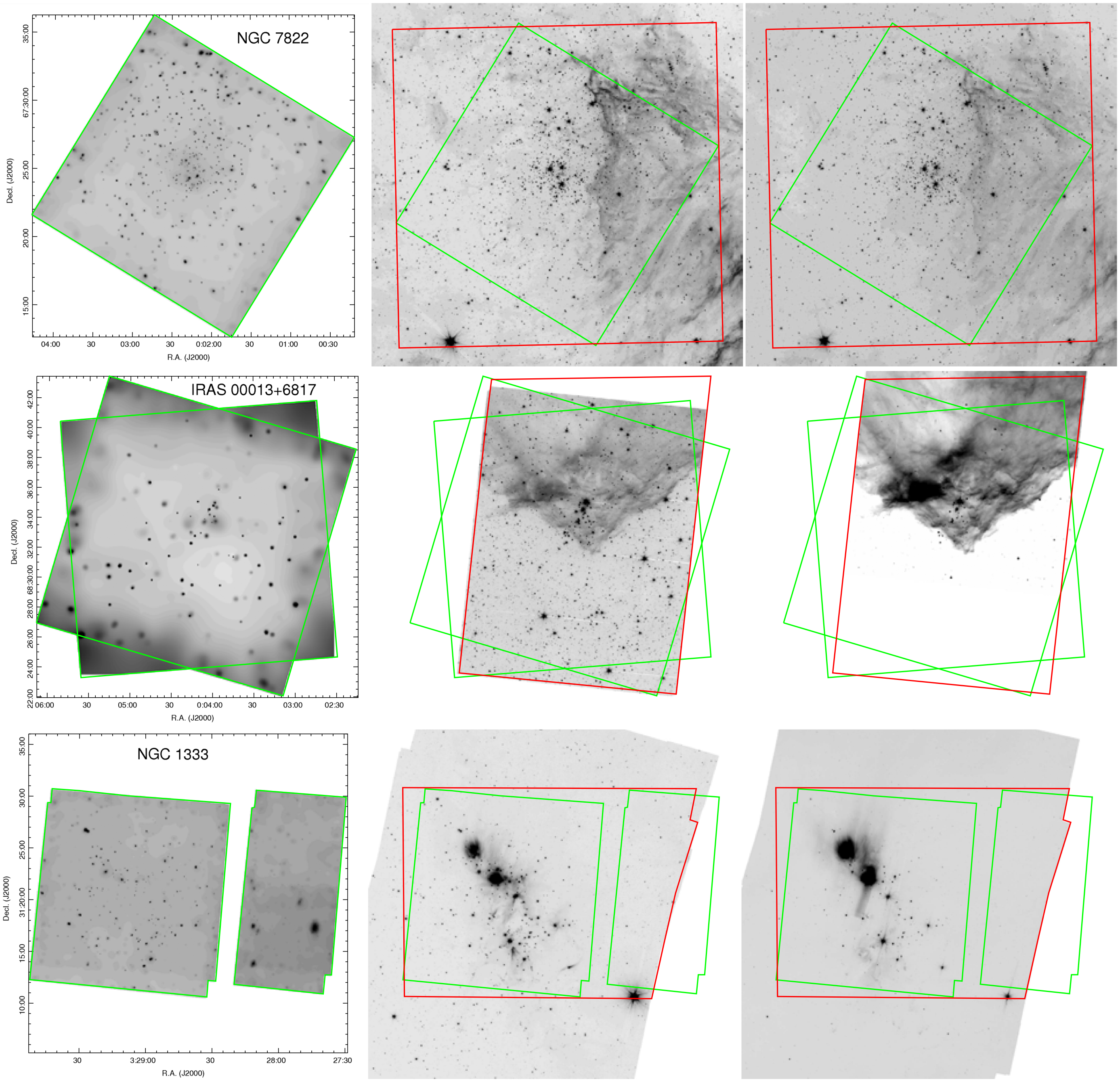

Figure 1. Low-resolution images of the SFiNCs SFRs: adaptively smoothed *Chandra*-ACIS image in the total (0.5–8) keV band (left), *Spitzer*-IRAC in the 3.6 μm band (middle), and *Spitzer*-IRAC 8.0 μm band (right). For NGC 7822, no observations were taken in the IRAC 8.0 μm band; instead, the *Spitzer*-IRAC image in the 4.5 μm band is shown. *Chandra*-ACIS field of view is outlined in green; for the reference on the angular size of the field, recall that the size of a single square *Chandra*-ACIS-I field is $\sim 17' \times 17'$. The field of view for the "cut-out" IRAC catalog (Section 3.4) is outlined in red.

(The complete figure set (8 images) is available.)

the estimates of the column densities and intrinsic X-ray fluxes (Columns 10–18 in Table 4) could be inaccurate for high-mass stellar members of the SFiNCs SFRs as well as for non-members, such as Galactic field stars and extragalactic objects, whereas the incident and apparent X-ray fluxes (Columns 4–9 in Table 4) are valid for any class of X-ray sources.

X-ray luminosity in the total X-ray band ($L_{\rm tc}$) can be derived from the $F_{\rm tc}$ quantity (Column 16 in Table 4) by multiplying it by $4\pi d^2$ where d is the object's distance, in centimeters, assuming that the object is a YSO member of a SFiNCs region. For the sets of the SFiNCs cluster members (defined further in Section 4.1) with available $L_{\rm tc}$ measurements, their X-ray luminosity functions are presented in Figure 2; the XLFs are sorted by the SFR distances. The X-ray sensitivity to a PMS population is a function of the X-ray exposure time, the SFR distance, and the X-ray absorption of the PMS population. Figure 2 shows that for the nearest SFiNCs regions NGC 1333 and IC 348 their XLFs peak at $\log(L_{\rm tc}) \sim 29$–29.5 erg s^{-1}, whereas for the most distant regions RCW 120 and Sh 2-106 the peaks are at $\log(L_{\rm tc}) \sim 30.3$–$30.8$ erg s^{-1}.

Table 3
SFiNCs X-Ray Sources and Basic Properties

Source			Position				Extraction					Characteristics				
SFR	Seq. No.	CXOU J	α (J2000) (°)	δ (J2000) (°)	Error (″)	θ (′)	$C_{t,\mathrm{net}}$ (cts)	$\sigma_{t,\mathrm{net}}$ (cts)	B_t (cts)	$C_{h,\mathrm{net}}$ (cts)	PSF Frac.	SNR	log P_B	Anom.	Var.	E_{median} (keV)
(1)	(2)	(3)	(4)	(5)	(6)	(7)	(8)	(9)	(10)	(11)	(12)	(13)	(14)	(15)	(16)	(17)
NGC 7822	1	000033.87+672446.2	0.141150	67.412846	0.6	10.3	30.5	6.1	3.5	21.9	0.54	5.2	<-5	…	a	2.6
NGC 7822	2	000033.92+672452.8	0.141362	67.414691	0.8	10.3	7.5	3.5	4.5	3.7	0.39	2.0	−2.9	…	a	1.6
NGC 7822	3	000034.62+672537.7	0.144257	67.427159	0.9	10.2	30.4	6.5	10.6	18.2	0.91	4.5	<-5	…	a	2.6
NGC 7822	4	000036.43+672658.5	0.151798	67.449596	0.6	10.2	71.9	9.0	8.1	32.9	0.91	7.9	<-5	…	a	1.9
NGC 7822	5	000041.15+672526.6	0.171487	67.424076	1.5	9.6	8.5	4.1	7.5	8.7	0.91	1.9	−2.4	…	a	5.0
NGC 7822	6	000044.02+672844.3	0.183441	67.478987	1.4	10.1	11.9	4.6	8.1	10.7	0.91	2.4	−3.3	…	a	4.0
NGC 7822	7	000044.33+672306.9	0.184745	67.385269	1.6	9.4	5.1	3.3	5.9	5.5	0.89	1.4	−2.2	…	b	4.1
NGC 7822	8	000045.20+672805.8	0.188345	67.468297	1.1	9.7	19.2	5.2	6.8	2.0	0.91	3.5	<-5	…	a	1.7
NGC 7822	9	000046.19+672358.2	0.192477	67.399503	0.8	9.1	30.2	6.1	5.8	8.0	0.91	4.7	<-5	…	a	1.6
NGC 7822	10	000048.35+672648.8	0.201499	67.446893	0.7	9.1	40.3	6.8	5.7	28.1	0.90	5.7	<-5	…	a	3.0

Note. This table is available in its entirety (15364 SFiNCs X-ray sources) in the machine-readable form in the online journal. A portion is shown here for guidance regarding its form and content. The format of this table is similar to that of Table 1 in Broos et al. (2010). Column 1: star-forming region. Column 2: X-ray catalog sequence number, sorted by R.A. Column 3: IAU designation. Columns 4–5: R.A. and decl. (in decimal degrees) for epoch J2000.0. Column 6: estimated standard deviation of the random component of the position error, $\sqrt{\sigma_x^2 + \sigma_y^2}$. The single-axis position errors, σ_x and σ_y, are estimated from the single-axis standard deviations of the PSF inside the extraction region and the number of counts extracted. Column 7: off-axis angle. Columns 8 and 9: net counts extracted in the total energy band (0.5–8 keV); average of the upper and lower 1σ errors on Column 9. Column 10: background counts expected in the source extraction region (total band). Column 11: net counts extracted in the hard energy band (2–8 keV). Column 12: fraction of the PSF (at 1.497 keV) enclosed within the extraction region. A reduced PSF fraction (significantly below 90%) may indicate that the source is in a crowded region. Column 13: photometric significance computed as net counts divided by the upper error on net counts. Column 14: logarithmic probability that extracted counts (total band) are solely from background. Some sources have P_B values above the 1% threshold that defines the catalog because local background estimates can rise during the final extraction iteration after sources are removed from the catalog. Column 15: source anomalies: (g) fractional time that source was on a detector (FRACEXPO from *mkarf*) is <0.9; (e) source on field edge; (p) X-ray properties may be biased due to photon pile-up; (s) source on readout streak; (a) photometry and spectrum may contain $>10\%$ afterglow events. Column 16: variability characterization based on K-S statistic (total band) from the single ObsId showing the most variability: (a) no evidence for variability ($0.05 < P_{KS}$); (b) possibly variable ($0.005 < P_{KS} < 0.05$); (c) definitely variable ($P_{KS} < 0.005$). No value is reported for sources with fewer than four counts or for sources in chip gaps or on field edges. Column 17: background-corrected median photon energy (total band).

(This table is available in its entirety in machine-readable form.)

Table 4
SFiNCs X-Ray Fluxes

Source			*AE* Fluxes		Spectral Properties from XPHOT												
SFR	Seq. No.	CXOU J	log PF_h (photon cm^{-2} s^{-1})	log PF_t (photon cm^{-2} s^{-1})	log F_h (erg cm^{-2} s^{-1})	σ (erg cm^{-2} s^{-1})	log F_t (erg cm^{-2} s^{-1})	σ (erg cm^{-2} s^{-1})	log N_H (cm^{-2})	$\sigma_{\rm stat}$ (cm^{-2})	$\sigma_{\rm sys}$ (cm^{-2})	log F_{hc} (erg cm^{-2} s^{-1})	$\sigma_{\rm stat}$ (erg cm^{-2} s^{-1})	$\sigma_{\rm sys}$ (erg cm^{-2} s^{-1})	log $F_{\rm tc}$ (erg cm^{-2} s^{-1})	$\sigma_{\rm stat}$ (erg cm^{-2} s^{-1})	$\sigma_{\rm sys}$ (erg cm^{-2} s^{-1})
(1)	(2)	(3)	(4)	(5)	(6)	(7)	(8)	(9)	(10)	(11)	(12)	(13)	(14)	(15)	(16)	(17)	(18)
NGC 7822	1	000033.87+672446.2	−5.293	−5.161	−13.661	0.122	−13.527	0.105	22.38	0.11	0.08	−13.536	0.125	0.043	−13.048	0.114	0.172
NGC 7822	2	000033.92+672452.8	−5.924	−5.632	−14.361	0.391	−14.233	0.262	21.95	0.65	0.12	−14.304	0.394	0.034	−13.844	0.328	0.251
NGC 7822	3	000034.62+672537.7	−5.640	−5.432	−13.900	0.142	−13.808	0.109	22.40	0.10	0.11	−13.764	0.145	0.065	−13.283	0.118	0.298
NGC 7822	4	000036.43+672658.5	−5.383	−5.061	−13.626	0.095	−13.560	0.066	22.08	0.12	0.08	−13.560	0.096	0.020	−13.196	0.078	0.126
NGC 7822	5	000041.15+672526.6	−5.969	−6.001	−13.999	0.220	−13.972	0.239	23.48	0.25	…	−13.266	0.326	0.087	−12.838	0.339	0.227
NGC 7822	6	000044.02+672844.3	−5.872	−5.834	−14.008	0.198	−13.967	0.193	23.00	0.27	0.08	−13.625	0.263	0.114	−13.184	0.263	0.263
NGC 7822	7	000044.33+672306.9	−6.154	−6.192	−14.324	0.302	−14.310	0.339	23.11	0.36	0.07	−13.848	0.417	0.153	−13.395	0.447	0.428
NGC 7822	8	000045.20+672805.8	−6.598	−5.643	…	…	…	…	…	…	…	…	…	…	…	…	…
NGC 7822	9	000046.19+672358.2	−6.008	−5.448	−14.370	0.226	−14.073	0.101	21.84	0.15	0.16	−14.326	0.226	0.031	−13.732	0.119	0.248
NGC 7822	10	000048.35+672648.8	−5.463	−5.331	−13.729	0.105	−13.633	0.089	22.53	0.11	0.07	−13.559	0.112	0.051	−13.090	0.102	0.183

Note. This table is available in its entirety (15364 SFiNCs X-ray sources) in the machine-readable form in the online journal. A portion is shown here for guidance regarding its form and content. Fluxes given in columns 4–5 are produced by *AE* (Broos et al. 2010). Fluxes and column densities given in columns 6–18 are produced by *XPHOT* (Getman et al. 2010). *XPHOT* assumes X-ray spectral shapes of young, low-mass stars. Intrinsic *XPHOT* quantities (columns 10–18) will be unreliable for high-mass stellar members of the SFiNCs SFRs as well as for non-members, such as Galactic field stars and extragalactic objects. The fluxes and the column densities are given in a log scale. Column 1: star-forming Region. Column 2: X-ray catalog sequence number, sorted by R.A. Column 3: IAU designation. Columns 4–5: incident X-ray photon fluxes in the hard (2–8) keV and total (0.5–8) keV bands, respectively. Columns 6–9: apparent X-ray fluxes in the hard and total bands, and their 1σ statistical uncertainties. Columns 10–12: X-ray column density and its 1σ statistical and systematic uncertainties. Columns 13–18: corrected for absorption, X-ray fluxes in the hard and total bands, and their 1σ statistical and systematic uncertainties.

(This table is available in its entirety in machine-readable form.)

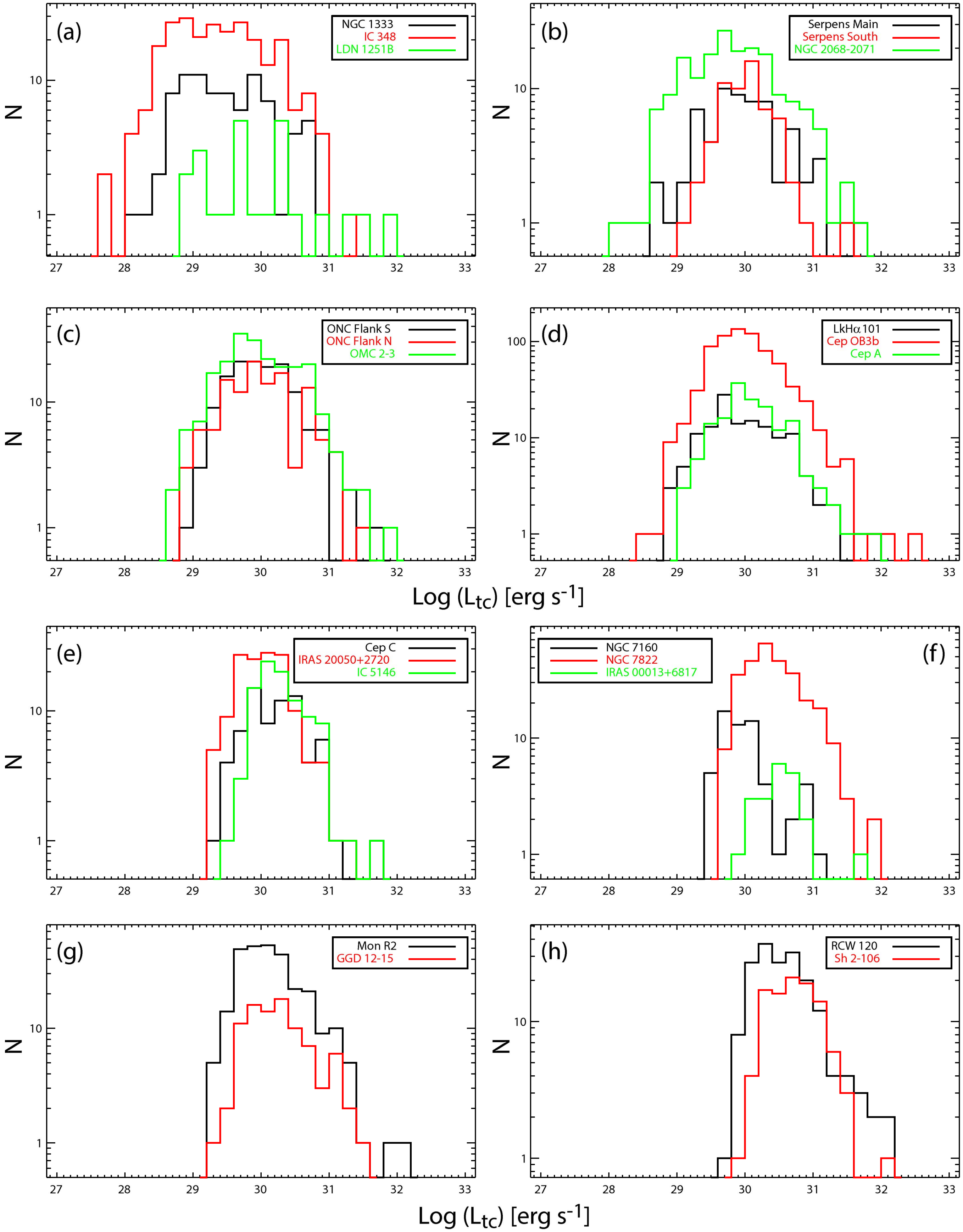

Figure 2. X-ray luminosity functions (XLFs) for the SFiNCs cluster members with available L_{tc} estimates. The XLFs are arranged in figure panels based on the SFiNCs SFRs' distances: from the nearest SFRs (panel (a)) to the most distant SFRs (panel (h)).

Table 5
Log of SFiNCs *Spitzer*-IRAC Observations

Region (1)	AOR (2)	PID (3)	Start Time (UT) (4)	Stop Time (UT) (5)	Center α_{J2000} (6)	Center δ_{J2000} (7)	IRAC Mode (8)	PI (9)
NGC 7822	48001280	90179	2013-04-12 10:27:38	2013-04-12 16:34:37	0.570833	67.419194	IRAC Map PC	Getman, Konstantin V
IRAS 00013+6817	3658240	6	2003-12-23 13:33:58	2003-12-23 14:06:02	0.994833	68.594583	IRAC Map	Fazio, Giovanni
NGC 1333	16034304	178	2005-09-16 09:56:12	2005-09-16 10:59:36	52.437500	30.913889	IRAC Map	Evans, Neal
NGC 1333	3652864	6	2004-02-10 08:29:23	2004-02-10 09:23:31	52.252458	31.311917	IRAC Map	Fazio, Giovanni
NGC 1333	5793280	178	2004-09-08 17:03:35	2004-09-08 17:37:59	52.252458	31.311917	IRAC Map	Evans, Neal
NGC 1333	18323968	30516	2007-02-15 21:50:58	2007-02-15 22:34:19	52.293333	31.225000	IRAC Map	Looney, Leslie W
NGC 1333	18325760	30516	2007-02-15 21:07:00	2007-02-15 21:50:22	52.185417	31.094167	IRAC Map	Looney, Leslie W
IC 348	16034048	178	2005-09-16 09:10:33	2005-09-16 09:54:45	56.150000	31.927222	IRAC Map	Evans, Neal
IC 348	34977024	60160	2009-10-02 21:25:30	2009-10-02 21:57:37	56.083667	32.050278	IRAC Map PC	Muzerolle, James
IC 348	34977280	60160	2009-10-04 02:44:04	2009-10-04 03:26:21	56.083667	32.050278	IRAC Map PC	Muzerolle, James

Note. This table is available in its entirety (423 *Spitzer*-IRAC AORs for the 22 SFiNCs SFRs) in the machine-readable form in the online journal. A portion is shown here for guidance regarding its form and content. Column 1: star-forming Region. Column 2: astronomical Object Request number. Column 3: *Spitzer* program identification number. Columns 4–5: start and stop times of the observation, in UT. Columns 6–7: approximate center of the observation; R.A. and decl. for epoch (J2000.0). Column 8: IRAC mode. The PC (Post-Cryo) mode has been introduced during the warm mission of the *Spitzer* observatory with only two shortest-wavelength IRAC modules in operation. Column 9: the principal investigator of the observation.

(This table is available in its entirety in machine-readable form.)

For the PMS members of young (age $\lesssim$ 5–10 Myr) stellar clusters, their X-ray luminosities can be translated to stellar masses (Getman et al. 2014a) using the empirical X-ray luminosity/mass relation calibrated to well-studied Taurus PMS stars (Telleschi et al. 2007). We thus expect that our SFiNCs X-ray source catalog includes PMS subsamples that are roughly complete down to $\sim 0.3\,M_\odot$ and $\sim 2\,M_\odot$ for the nearest and the most distant SFiNCs SFRs, respectively.

3.3. Spitzer-IRAC Data

Spitzer-IRAC infrared photometry (often together with *JHK* measurements) is used to establish the presence of protoplanetary disks around cluster members. All but two SFiNCs regions have published catalogs of *Spitzer*-selected disk-bearing stellar populations (Table 1); typical regions have 100–200 published infrared-excess young objects. For MYStIX, we found published catalogs were often inadequate due to crowding and strong PAH-band nebulosity so that a new analysis was needed. For SFiNCs, both crowding and nebulosity are greatly reduced and we believe that published catalogs of disky YSOs have sufficient high quality to provide the basis for constructing our catalogs. The catalogs for 12 of the 22 SFiNCs regions have been reduced in a consistent way by Gutermuth et al. (2009), and most of the other regions have catalogs derived using similar consistent procedures by Megeath et al. (2012) and Allen et al. (2012). Nevertheless, most of these published *Spitzer* catalogs are limited to disky YSOs.

To obtain MIR photometry for X-ray objects and to identify and measure MIR photometry for additional non-*Chandra* disky stars that were missed in previous studies of the SFiNCs regions (typically faint YSOs), we have reduced the archived *Spitzer*-IRAC data by homogeneously applying the MYStIX-based *Spitzer*-IRAC data reduction methods of Kuhn et al. (2013b) to the 423 Astronomical Object Request (AORs) data sets for the 22 SFiNCs SFRs (Table 5).

These observations were taken with the IRAC (Infrared Array Camera) detector (Fazio et al. 2004), which operates simultaneously on four wavelengths in two pairs of channels (3.6 and 5.8; 4.5 and 8.0 μm), providing $5\farcm2 \times 5\farcm2$ images with spatial resolution of FWHM = $1\farcs6$ to $1\farcs9$ from 3.6 to 8 μm. Most of these observations were taken in the high-dynamic-range mode, to provide unsaturated photometry for both brighter and fainter sources. Over 70% of these were taken in the Post-Cryo mode during the warm mission of the *Spitzer* observatory with only two shortest wavelengths in operation. NGC 7822 is the only SFiNCs region lacking data in the two longest IRAC wavelengths, 5.8 and 8.0 μm.

Typical total integration times per pixel for long frames in the channel 3.6, for all combined observations per SFiNCs SFR, are $\gtrsim$50 s pix^{-1}. For nine SFiNCs SFRs (NGC 7822, IC 348, ONC Flank S, Serpens Main, IRAS 20050+2720, Sh 2-106, NGC 7160, Cep OB3b, and Cep A) the integration times are close to or over 100 s pix^{-1}. Only one SFR, RCW 120, is limited to a short GLIMPSE exposure of 2 × 1.2 s pix^{-1}. For all but seven SFiNCs regions, their *Chandra*-ACIS-I fields have full IRAC coverage; for the seven regions (IRAS 00013+6817, LkHα 101, ONC Flank S, ONC Flank N, IRAS 20050+2720, LDN 1251B, and Cep C) the IRAC observations cover over 80%–90% of the *Chandra*-ACIS-I fields (Figure 1).

Our *Spitzer*-IRAC data reduction follows the procedures described in detail by the MYStIX study of Kuhn et al. (2013b). Briefly, Basic Calibrated Data (BCD) products from the *Spitzer* Science Center's IRAC pipeline were automatically treated with the WCSmosaic IDL package developed by R. Gutermuth from the IRAC instrumental team. Starting with BCD data products, the package mosaics individual exposures while treating bright source artifacts, cosmic-ray rejection, distortion correction, subpixel offsetting, and background matching (Gutermuth et al. 2008). We selected a plate scale of 0$''$.86 for the reduced IRAC mosaics, which is the native scale divided by $\sqrt{2}$. Source detection was performed on mosaicked images using the IRAF task STARFIND.

Aperture photometry of IRAC sources was obtained using the IRAF task PHOT. The photometry was calculated in circular apertures with radius of 2, 3, 4, and 14 pixels (1$''$.7, 2$''$.6, 3$''$.5, 12$''$.1). For all the SFiNCs IRAC sources 1 pixel wide background was adopted. There is no improvement in photometry if a 4-pixel-wide background is used instead (Getman et al. 2012). Using the IRAC PSF for the [3.6] band re-sampled to a plate scale of 0$''$.86, pairs of sources are simulated with wide ranges of source separations, orientations, and flux ratios to derive the flux contribution from a nearby source within 2, 3, and 4 pixel apertures as a function of separation angle and flux ratio (Kuhn et al. 2013b). For the real sources, their photometry is derived using 2-, 3-, and 4-pixel-source apertures, and we report photometry from the largest aperture for which the expected contamination from a nearby source is less than 5%; larger apertures were favored for uncrowded sources and smaller apertures favored for crowded sources. Extractions from the 14-pixel ($\sim$10 native pixel) apertures for the relatively isolated, bright, and unsaturated SFiNCs sources were employed to estimate the aperture correction values. We adopt the same zero-point IRAC magnitudes for the different cases of apertures as those used in MYStIX (Section 3.3 in Kuhn et al. 2013b).

3.4. *IRAC Source Catalog*

As in MYStIX, here the SFiNCs IRAC source catalog retains all point sources with the photometric signal-to-noise ratio >5 in both [3.6] and [4.5] channels. This catalog covers the 22 SFiNCs SFRs and their vicinities on the sky and comprises 1638654 IRAC sources with available photometric measurements for 100%, 100%, 29%, and 23% of these sources in the 3.6, 4.5, 5.8, and 8.0 μm bands, respectively. Over 90% of these sources are from the extraction of the wide mosaics in/around the following six SFiNCs SFRs: Mon R2, RCW 120, Serpens South, Sh 2-106, Cep OB3b, and Cep A. Table 6 lists IRAC sources' positions, IRAC-band magnitudes and their uncertainties, and aperture size flag. The magnitude uncertainties include the statistical uncertainty, uncertainty in the calibration of the IRAC detector, and uncertainty in the aperture correction. The cases for which the contamination from a nearby source exceeds 10% in the smallest 2-pixel aperture are flagged as "-1" (last column in Table 6). Similarly to MYStIX, the fractions of the SFiNCs IRAC sources with different aperture sizes are: 13% with 4-pixel apertures, 10% with 3-pixel apertures, and 77% with 2-pixel apertures (44% of the sources have flags indicating crowding).

From the entire SFiNCs IRAC catalog we consider a subsample of the IRAC sources ($\sim$22%) that covers only the *Chandra*-ACIS fields and their *immediate* vicinities (marked as red polygons in Figure 1) and thus harbors a significant fraction of SFiNCs YSO members; we call this the "cut-out" sample. Figure 3 shows the histograms of the [3.6]-band magnitude for the "cut-out" sample. The sensitivity of the sample depends on a number of factors: IRAC exposure time, presence/absence of a diffuse nebular background, source extinction and distance to an object of interest. For most SFiNCs SFRs, the histograms peak near $m_{3.6} \sim 17$ mag, which would translate to a mass of a lightly obscured, diskless SFiNCs YSO, located in a region with low nebulosity, of $<0.1\ M_{\odot}$. Thus, the *Spitzer*-based sample of disk-bearing PMS stars goes down to lower masses than the *Chandra*-based sample of PMS stars ($M \gtrsim 0.3\ M_{\odot}$, Section 3.2).

The comparison between the SFiNCs IRAC catalog and the previously published *Spitzer* catalogs is presented in Appendix A. Since most of the published catalogs are limited to disk-bearing YSO objects, the number of IRAC sources in SFiNCs is typically by a factor of >60 higher than that in the earlier studies (Table 11). As in MYStIX (Kuhn et al. 2013b), the SFiNCs MIR photometry is in a good agreement with that of the previous MIR studies (Figure 21).

3.5. *X-Ray/Infrared Matching*

Due to the deterioration of the *Chandra* telescope PSF with the off-axis angle, the SFiNCs X-ray sources lying on the ACIS-S chips for all but one SFiNCs regions (IC 5146) were further omitted from our identification and membership analyses. For IC 5146, the X-ray data from the ObsID 6401, with the aimpoint on S3 chip, were retained for further analyses.

Source position cross correlations between the SFiNCs *Chandra* X-ray source catalog (Section 3.2) and an IR catalog, either the "cut-out" IRAC (Section 3.4) or 2MASS (Skrutskie et al. 2006), were made using the following steps.

First, the trivial matching of close source pairs within the constant 2$''$ radius was used to identify candidate matches. The 2$''$ tolerance size was chosen based on the X-ray-IR source positional offsets obtained in the COUP project (Figure 9 in Getman et al. 2005).

Second, the more sophisticated matching with the IDL tool *match_xy* (Section 8 in Broos et al. 2010) was applied to all the candidate matches from the previous step. The *match_xy* package takes into consideration the positional statistical uncertainties of individual sources, which is particularly relevant for *Chandra* X-ray source catalogs since the *Chandra* PSF significantly degrades off-axis.[9] The *match_xy* tool was applied only to closest pairs, discarding multiple matches, and was run to accept matches, for which the source separations are less than 2.3 times the combined uncertainty on positions.

Third, we performed a careful visual inspection of all source pairs with the X-ray-IR separations of <2$''$ (candidate matches from the first step) that were rejected by the *match_xy* procedure during the second step. The results of this inspection suggest that for many of the rejected matches (typically 10% out of all possible X-ray-IR matches per a SFiNCs region) their unusually large separations arise from systematic effects, such as inaccurate measurements of X-ray/IR source positions due to the presence of multiple resolved or un-resolved sources. The *match_xy* tool does not account for such effects. As an example, expended views for a few of such X-ray-IR pairs are shown in Figure 4. Typical cases include: a cataloged double X-ray source and a single registered IR source visually recognized as a single (first panel from above); a cataloged double X-ray source and a double IR source with a single registered companion (second panel); a single registered and

---

[9] The X-ray source position uncertainty is a function of both the number of extracted counts and the off-axis angle. The SFiNCs X-ray random position uncertainties vary from 0$''$.1 in the core to $>1''$ in the halo parts of the SFiNCs fields; whereas the 2MASS and IRAC SFiNCs source position uncertainties remain fixed across the fields at the $\lesssim 0''.1$ and $\lesssim 0''.1$–$0''.3$ levels for the relatively bright ($J < 16$ mag) 2MASS and IRAC sources, respectively.

Table 6
SFiNCs IRAC Sources and Photometry

Region (1)	Source (2)	R.A. (deg) (3)	Decl. (deg) (4)	[3.6] (mag) (5)	σ_[3.6] (mag) (6)	[4.5] (mag) (7)	σ_[4.5] (mag) (8)	[5.8] (mag) (9)	σ_[5.8] (mag) (10)	[8.0] (mag) (11)	σ_[8.0] (mag) (12)	ApertureFl (13)
NGC 7822	G118.0586+05.2740	0.0017167	67.6576472	15.190	0.022	15.134	0.027	…	…	…	…	4
NGC 7822	G117.9462+04.7218	0.0018208	67.0942639	14.366	0.027	14.438	0.019	…	…	…	…	4
NGC 7822	G117.9954+04.9637	0.0018333	67.3410528	14.171	0.075	14.056	0.053	…	…	…	…	4
NGC 7822	G117.9429+04.7056	0.0018708	67.0777194	14.289	0.017	14.247	0.014	…	…	…	…	4
NGC 7822	G118.0391+05.1771	0.0023458	67.5588750	13.123	0.022	13.023	0.019	…	…	…	…	2
NGC 7822	G117.9819+04.8961	0.0023958	67.2720972	15.710	0.108	15.415	0.106	…	…	…	…	2
NGC 7822	G118.0296+05.1298	0.0025708	67.5106333	15.856	0.092	15.759	0.091	…	…	…	…	2
NGC 7822	G117.9481+04.7292	0.0027542	67.1018444	14.157	0.033	14.158	0.037	…	…	…	…	4
NGC 7822	G118.0293+05.1283	0.0027625	67.5090611	13.802	0.033	13.602	0.032	…	…	…	…	4
NGC 7822	G118.0301+05.1319	0.0027750	67.5127861	15.815	0.053	15.960	0.078	…	…	…	…	3

Note. This table is available in its entirety (1638654 *Spitzer*-IRAC sources in/around the 22 SFiNCs SFRs) in the machine-readable form in the online journal. A portion is shown here for guidance regarding its form and content. The format of the table is similar to that of MYStIX Table 3 in Kuhn et al. (2013b). Column 1: SFiNCs SFR name. Column 2: source name in the GLLL.llll+BB.bbbb format. Columns 3–4: R.A. and decl. in decimal degrees (J2000.0). Columns 5–12: IRAC magnitudes and their 1σ errors for the 3.6, 4.5, 5.8, and 8.0 μm bands. Column 13: aperture size flag: 2, 3, and 4–2, 3, and 4-pixel aperture with contaminating flux $<10\%$ of source flux; -1–2-pixel aperture with contaminating flux $>10\%$ of source flux.

(This table is available in its entirety in machine-readable form.)

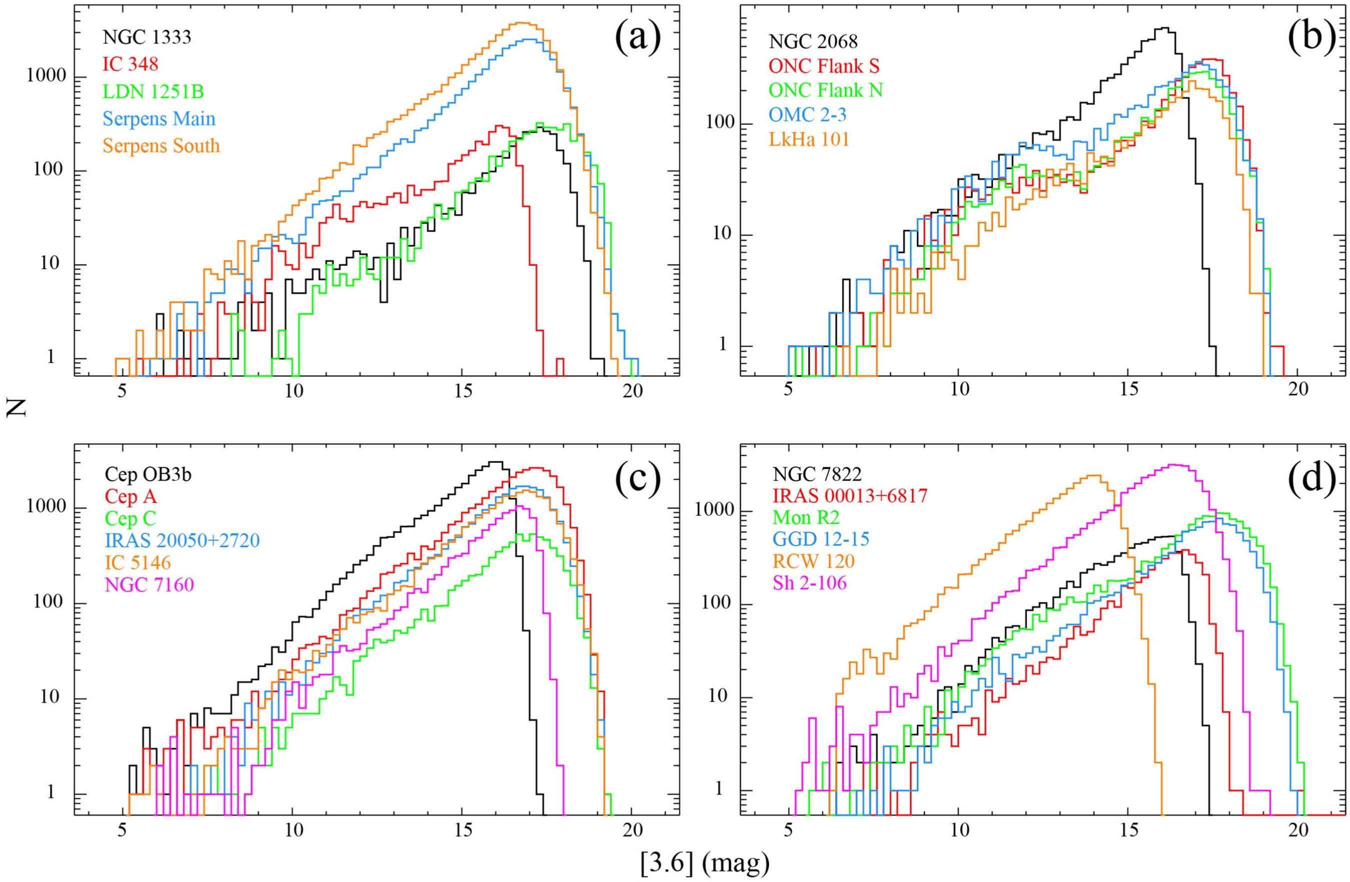

Figure 3. Histograms of the [3.6]-band magnitude for the SFiNCs IRAC "cut-out" source sample. The histograms are arranged in figure panels based on the SFiNCs SFRs' distances: from the nearest SFRs (panel (a)) to the most distant SFRs (panel (d)).

visually recognized X-ray source and a double IR source with a single registered companion (third panel); both X-ray and IR sources viewed and registered as single sources (forth panel); a single X-ray source near a registered IR double (fifth panel). More complex cases involving triple and multiple visual systems exist. In all of these cases, the X-ray and IR source extraction regions still highly overlap and their X-ray-IR properties are often consistent with the X-ray-IR trends seen for the source pairs accepted by *match_xy*, such as the trends of the X-ray flux versus the *J*-band magnitude and the X-ray median energy versus the $J - H$ color. For the SFiNCs membership study, we consider to retain such pairs as legitimate X-ray-IR matches. In cases where there are double/multiple cataloged X-ray sources near a single cataloged IR source, notes on multiplicity are added for all such X-ray sources that are probable YSO members of the SFiNCs SFRs (see the YSO membership tables below), but only the X-ray source closest to the IR source is assigned as a formal counterpart to the IR source.

3.6. Sources of Contamination in SFiNCs

X-ray surveys of star-forming regions are subject to contamination by extragalactic AGNs and Galactic foreground and background stars (Getman et al. 2011; Broos et al. 2013). Unlike the MYStIX SFRs, the SFiNCs regions lie away from the Galactic plane where the field star contamination is greatly reduced. While detailed and sophisticated simulations of the X-ray contaminants for the SFiNCs fields are not feasible due to the lack of computing and manpower resources, we can evaluate the levels of the SFiNCs X-ray contaminants based on the results of the recent MYStIX simulations by Broos et al. (2013) for the two nearby MYStIX SFRs, Flame Nebula and RCW 36. Both have typical SFiNCs distances and *Chandra* observation exposure times (Feigelson et al. 2013): Flame Nebula ($d = 414$ pc) and RCW 36 ($d = 700$ pc) were captured in single *Chandra*-ACIS-I images, each with 70–80 ks exposure time. As most of the SFiNCs SFRs, Flame Nebula is a high-Galactic latitude region ($b = -16\overset{\circ}{.}4$), whereas RCW 36 lies close to the Galactic plane ($b = +1\overset{\circ}{.}4$). As the majority of the SFiNCs SFRs, both Flame and RCW 36 are relatively young regions featuring prominent molecular cloud structures.

Considering the results of the contamination simulations for this two SFRs (Table 8 in Broos et al. 2013), one may reasonably guess the typical numbers of the X-ray contaminants within the SFiNCs *Chandra* fields (per $17' \times 17'$ field): a dozen X-ray foreground stars, from a few to a dozen background stars, and roughly a hundred AGNs. The foreground stars are expected to have soft X-ray spectra ($E_{\rm median} < 1$ keV); the background stars would have X-ray median energies similar to the bulk of PMS stars ($1 < E_{\rm median} < 2.5$ keV); while the AGNs would have high median energies above 2–3 keV comparable mainly to deeply embedded YSOs and protostellar objects (Figure 2 in Broos et al. 2013). A quarter of these foreground stars, more than half of the background stars, and all of the AGNs are expected to be undetected by 2MASS (Figure 3 in Broos et al. 2013).

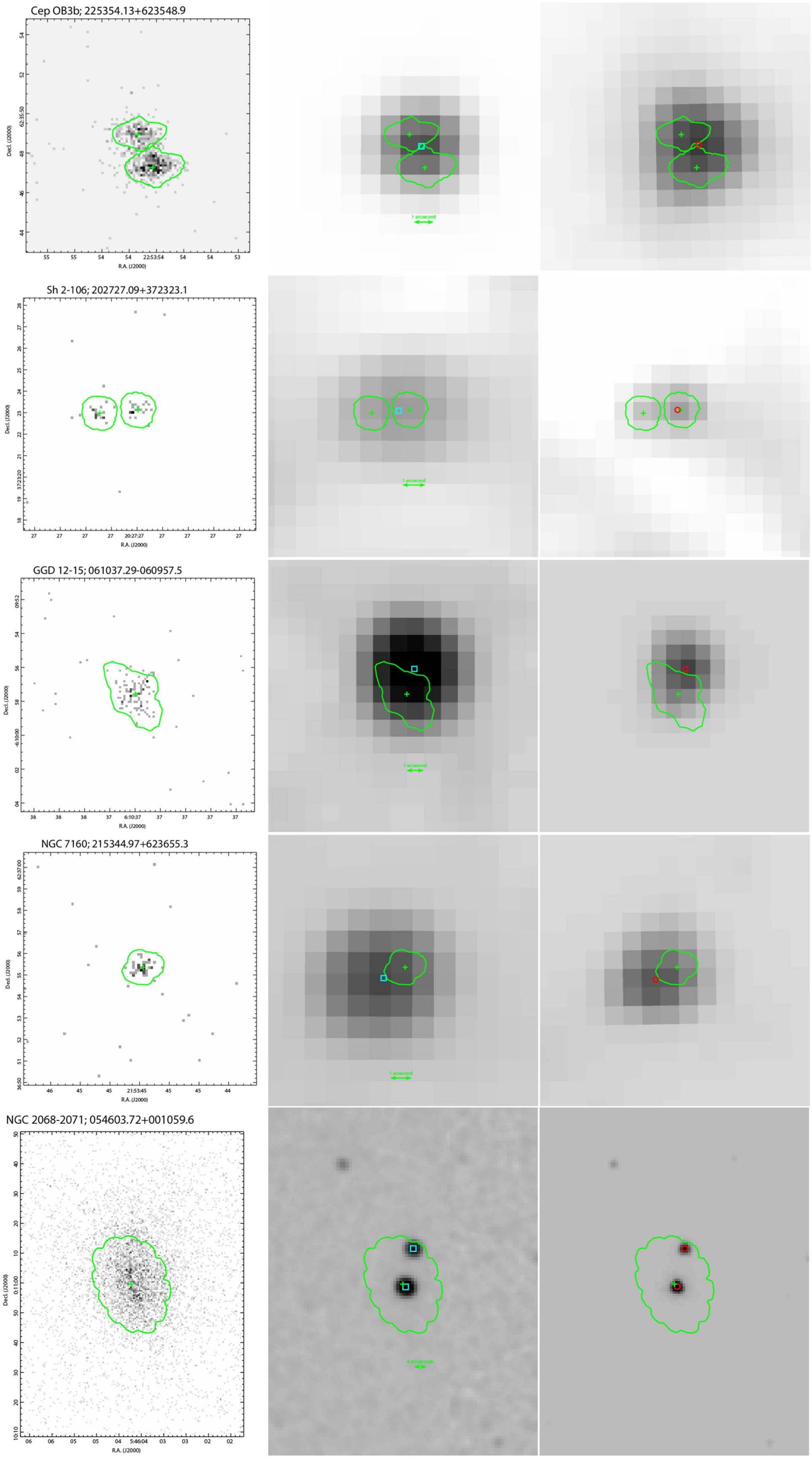

Figure 4. Examples of SFiNCs X-ray–IR pairs likely affected by the presence of double sources. *Chandra*-ACIS images (left), 2MASS *K*-band images (middle), and *Spitzer*-IRAC 3.6 μm images (right). Cataloged source positions of X-ray, 2MASS, and *Spitzer*-IRAC sources are given in green, cyan, and red, respectively. X-ray source extraction regions are outlined by the green polygons.

Although the overwhelming contamination from unrelated Galactic field stars prohibits IR surveys from providing complete censuses of YSO populations, these surveys are known to be very effective in isolating YSOs with IR excesses. The selection of disky YSOs is subject to further contamination by star-forming galaxies and obscured AGNs, and nebular knot emission (Gutermuth et al. 2009). For SFRs close to the Galactic midplane, additional major sources of contamination include dusty asymptotic giant branch (AGB) stars and YSOs from unrelated SFRs (Povich et al. 2013). For most of the SFiNCs SFRs located away from the Galactic midplane, the contamination of *Spitzer*-selected disky YSO samples by AGB stars is expected to be small, no more than a few percent (e.g., Dunham et al. 2015, and references therein); and the contamination by unrelated YSOs to be negligible or absent.

4. YSO Membership of the SFiNCs SFRs

4.1. YSO Selection Procedure

Since the Galactic field star contamination is greatly reduced in SFiNCs, the MYStIX's complex probabilistic X-ray and IR source classifications (Broos et al. 2013; Povich et al. 2013) are not needed here. Instead, the SFiNCs YSO classification can be achieved using simpler IR and X-ray classification approaches given in Gutermuth et al. (2009) and Getman et al. (2012). The major ten steps of our membership analysis are presented below.

First, we start by applying the YSO classification scheme of Gutermuth et al. (2009) to the SFiNCs IRAC "cut-out" catalog. The Phase 1 of the scheme identifies and removes star-forming galaxies and broad-line AGNs, as well as knots of shocked emission; the disky YSO candidates with available photometric measurements in all four IRAC bands are selected. The Phase 2 analysis is further applied to identify additional disky YSO candidates with IR photometry available only in the JHK_s[3.6][4.5] bands.

Second, following Getman et al. (2012), we construct the observed infrared spectral energy distributions (SEDs) in 2MASS+IRAC IR bands for all the SFiNCs IRAC disky YSO candidates as well as for all the SFiNCs X-ray sources with available IR photometric measurements, and compare them to the (de)reddened median SED templates of the IC 348 PMS stellar photospheres given by Lada et al. (2006). Figure 5 shows examples of such SEDs for several SFiNCs X-ray YSOs in the OMC 2-3 SFR. According to this SED-based analysis, the four sources shown in the upper panels are diskless YSOs, the next two sources (third row) are disky Class II YSOs, and the last two (bottom row) are disky Class I protostars. The two X-ray Class II YSOs (third row) are not listed in the previous disky YSO catalog of Megeath et al. (2012). While generally in agreement with the color–color approach of Gutermuth et al. (2009) for the IRAC-selected YSOs, the SED-based method is found to be extremely useful in selecting disky (flagged in the SFiNCs membership catalog as "DSK") and diskless ("NOD") X-ray YSO candidates.

Third, the X-ray sample is culled of X-ray selected YSO disky candidates with very faint MIR counterparts ($[3.6] \gtrsim 15.5$ mag and $[4.5] \gtrsim 14.5$ mag) whose spatial distribution is inconsistent with that of other YSO IR-X-ray candidates (if clustered) and/or molecular cloud cores seen in Herschel-*SPIRE* images. Most of those sources are considered to be X-ray AGN candidates (Getman et al. 2012). Their positions on the X-ray color–magnitude diagrams are consistent with those of extragalactic background sources (black points on the X-ray color–magnitude diagrams in Section 4.6).

The following steps locate additional SFiNCs YSO candidates that we flag as possible members ("PMB"). Fourth, the X-ray sources without IRAC (and often without 2MASS) counterparts that lie in the centers of YSO clusters/groups and are subject to significant MIR diffuse nebular background, especially for LkHα 101, Mon R2, RCW 120, Sh 2-106, and Cep A (Figure 1), are flagged as "PMB." In LkHα 101, the high diffuse background is due to the contamination from the point-spread function wings and trails of the bright EM* LkHα 101 star; in the remaining four regions the high background nebular emission is likely due to heated dust in the cluster cores. Figure 6 shows that most of these "PMB" sources are relatively bright X-ray sources (outlined in cyan) that are clearly visible by eye on the X-ray images but are often missed from the MIR images since the MIR point source sensitivity is dramatically reduced by the high nebular background. Their positions on the X-ray color–magnitude diagrams (presented below in Section 4.6) are consistent with those of highly absorbed YSOs, AGNs, or background field stars. However, since these are located at the very centers of dense stellar clusters and molecular cores (presented below as Figure 7), which subtend <1% of the $17' \times 17'$ ACIS-I field, the probability of being an AGN or a background star is tiny (Section 3.6). X-ray YSO clusters/groups without IR counterparts have been previously seen in other SFRs. For instance, in MYStIX SFRs, such as NGC 3576, M 17, NGC 6357, and RCW 38 (Section 2.3 and Figure 1 in Broos et al. 2013) and in the Carina Complex (Section 5.2.2 in Townsley et al. 2011). Fifth, the X-ray sources with 2MASS counterparts that are located outside the field of view of the SFiNCs IRAC "cut-out" catalog for the seven SFiNCs SFRs (IRAS 00013+6817, LkHα 101, ONC Flank S, ONC Flank N, IRAS 20050+2720, LDN 1251B, and Cep C in Figure 1) are flagged as "PMB." The positions of these sources on the X-ray and NIR color–color and color–magnitude diagrams are consistent with those of other SFiNCs YSO members (the diagrams are presented below in Sections 4.4, 4.6, and Appendix B). Sixth, based on the cross-correlation between the source positions of the SFiNCs X-ray/IR catalogs and the catalogs of massive OB-type stars from SIMBAD and Skiff (2009), all known OB-type stars in the SFiNCs fields are identified; the non-disky IR and/or undetected in X-rays OB stars are added to the SFiNCs membership catalog and flagged as "PMB." Seventh, the X-ray sources that are part of close visual double/multiple X-ray systems with their companions previously identified as YSO candidates, are also flagged as "PMB."

Eight, based on the criteria, $E_{\rm median} < 1$ keV and $J - H < 0.5$ mag, representing negligible interstellar absorption (Getman et al. 2012), we select foreground X-ray candidates, typically a few to several per SFiNCs field. However, these criteria are not sufficient for choosing definite foreground stars. The soft X-ray spectra and low NIR colors often pertain to intermediate and high-mass young stars. Many of these foreground candidates are found to be associated with the B-type probable members of the SFiNCs regions. For instance, three out of four foreground candidates in ONC Flank N are known B-type stars, including one of the ionizing stars of the region, B1V star c Ori. While many of the SFiNCs foreground candidates are diskless stars, three out of four of those in ONC

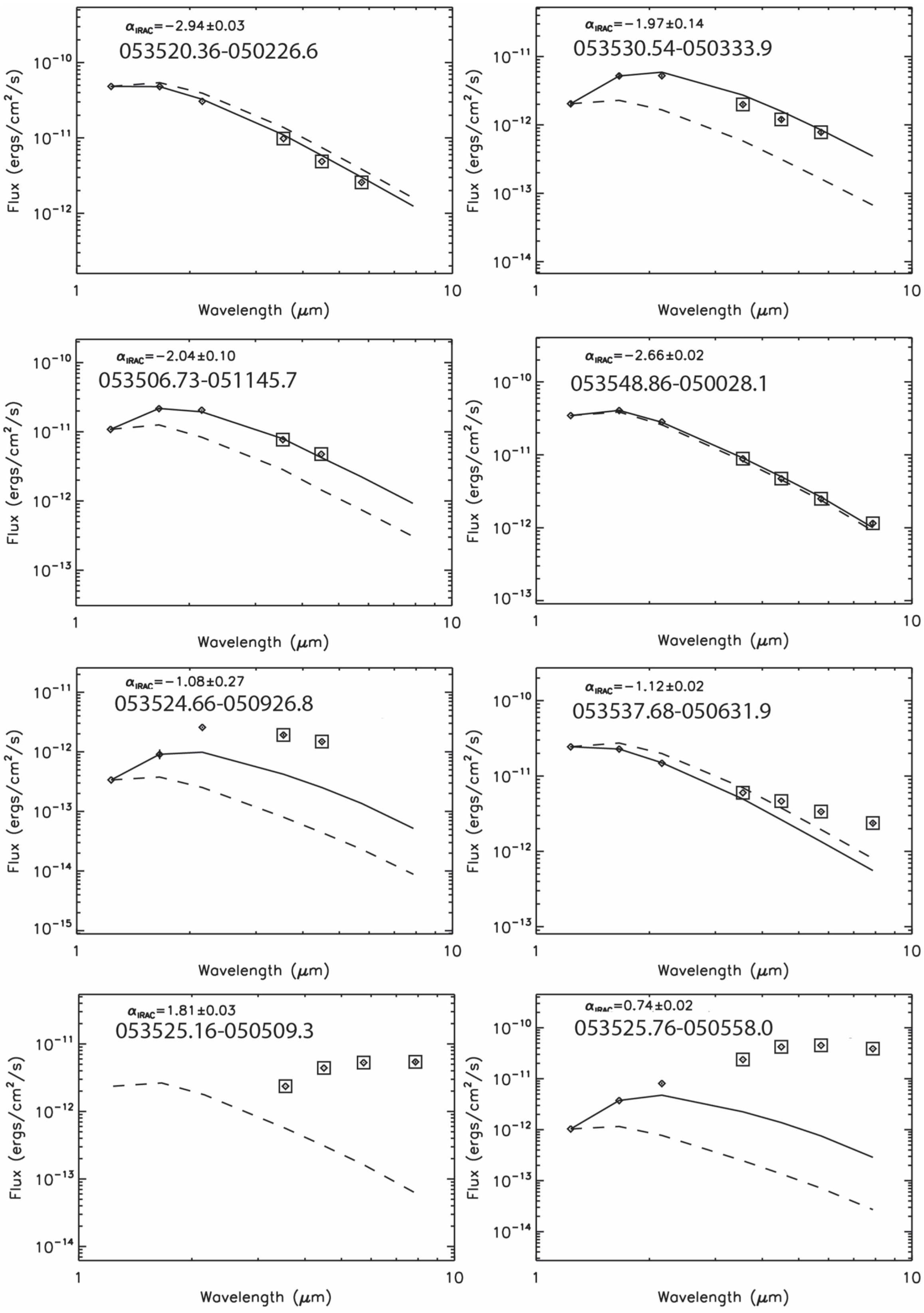

Figure 5. Examples of the IR SEDs for the diskless (upper four panels) and disky (bottom four panels) X-ray young objects in OMC 2-3. JHK_s (diamonds without squares) and IRAC-band (diamonds outlined by squares) flux points with usually small errors. The dashed and solid lines give the original and (de)reddened median SEDs for the IC 348 YSOs (Lada et al. 2006) fitted to the SFiNCs data. The panel legends give information on the SFiNCs sources' IAU name and apparent IRAC SED slope.

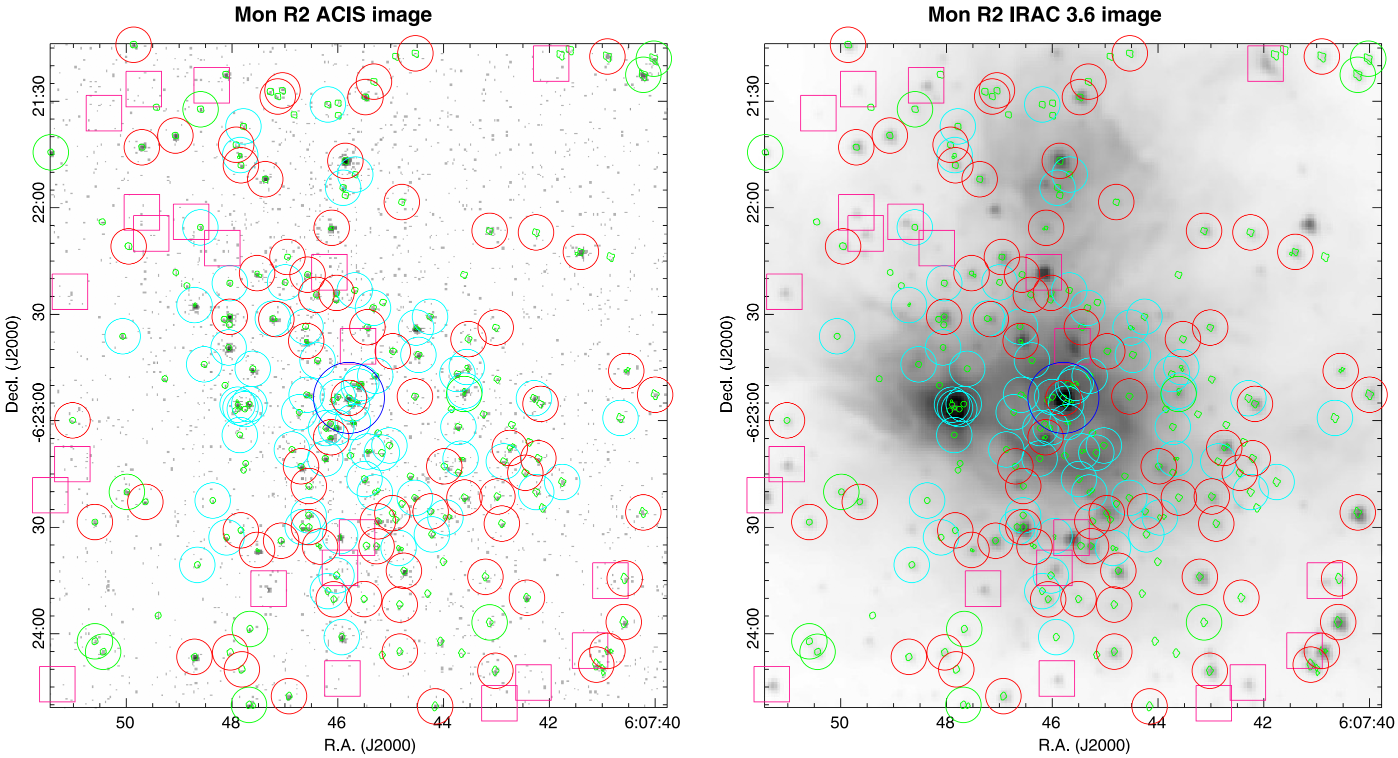

Figure 6. Close-up view of the centers of the YSO clusters/groups in LkHα 101, Mon R2, RCW 120, Sh 2-106, and Cep A that are subject to high MIR diffuse nebular background. An example is given for Mon R2. The figure set presenting all five SFRs is available in the online journal. *Chandra*-ACIS at (0.5–8) keV band and *Spitzer*-IRAC 3.6 μm images are shown on the left and right panels, respectively. The SFiNCs YSO members, as a final outcome of the YSO selection procedures in Section 4.1, are color-coded as: X-ray diskless YSOs (green circles), X-ray disky YSOs (red circles), non-X-ray disky YSOs (pink squares), "PMB" YSO members (cyan circles), and OB-type stars (blue circles). ACIS source extraction regions are outlined by green polygons.

(The complete figure set (5 images) is available.)

Flank S possess IR excesses. At this stage, we keep these objects in the SFiNCs membership database, with the suffix "FRG" appended to the name of their YSO class. During our final stage of the membership analysis (see below), the SFiNCs member sample is culled of a substantial number of these and additional foreground objects.

Ninth, our results on the YSO membership in SFiNCs are compared to those from the previous *Spitzer* studies of the SFiNCs SFRs (Column 9 in Table 1). Three major different types of inconsistencies can be noted. (1) With the exception of the Serpens South SFR, roughly several percent of sources in the compared catalogs are relatively faint MIR sources with their measurement uncertainties in either of the two catalogs (SFiNCs versus literature) being slightly larger than those imposed in the Phase 1/2 classification scheme of Gutermuth et al. (2009). Those that are too bright to be classified as background galaxies and pass our SED-based classification, were added to the SFiNCs membership catalog as additional disky YSOs. In the case of Serpens South, roughly 50% of additional disky YSOs from Povich et al. (2013) that passed our SED-based analysis were added to the SFiNCs membership catalog. (2) A few percent of sources in the compared catalogs have inconsistent classifications—transition disks in the published studies but diskless (based on our SED-based analysis) in the SFiNCs membership catalog. This is likely due to the use of additional longer wavelength MIPS data in the previous studies. For compatibility with the MYStIX data, we prefer to retain the diskless class for these sources; those that have X-ray counterparts further appear in our SFiNCs membership catalog as "NOD" members. (3) A few percent of sources that are identified as protostars in the previous studies but are not present in our SFiNCs IRAC catalog due to the imposed constraint on the photometric signal-to-noise ratio of >5 in both [3.6] and [4.5] channels for our catalog (Section 3.4). Such protostars are not included in our SFiNCs membership catalog.

Tenth, at this final stage, for every SFiNCs YSO member candidate a source atlas is created, similar to the one provided in the Appendix B. For each source, the atlas conveniently collects various source's properties into a two-page digest, including the source's spatial position, X-ray/IR photometric quantities, source's IR spectral energy distribution, source's locations on X-ray/IR color–magnitude and color–color diagrams, information on the presence/absence of a counterpart from previously published YSO catalogs, etc. For each source, we perform a visual inspection of the source atlas combined with the information on source's X-ray light-curve (not shown in the atlas), on source's spectral type from the SIMBAD database (when available), and on source's parallax measurements (when available) from the *Gaia*-Tycho catalog (Gaia Collaboration et al. 2016). This source examination allowed us to identify and remove over 500 ambiguous member candidates. These include a hundred foreground candidates (judging mainly from their parallax measurements and positions on the color–color and color–magnitude diagrams), a hundred weak IR non-X-ray sources (mainly

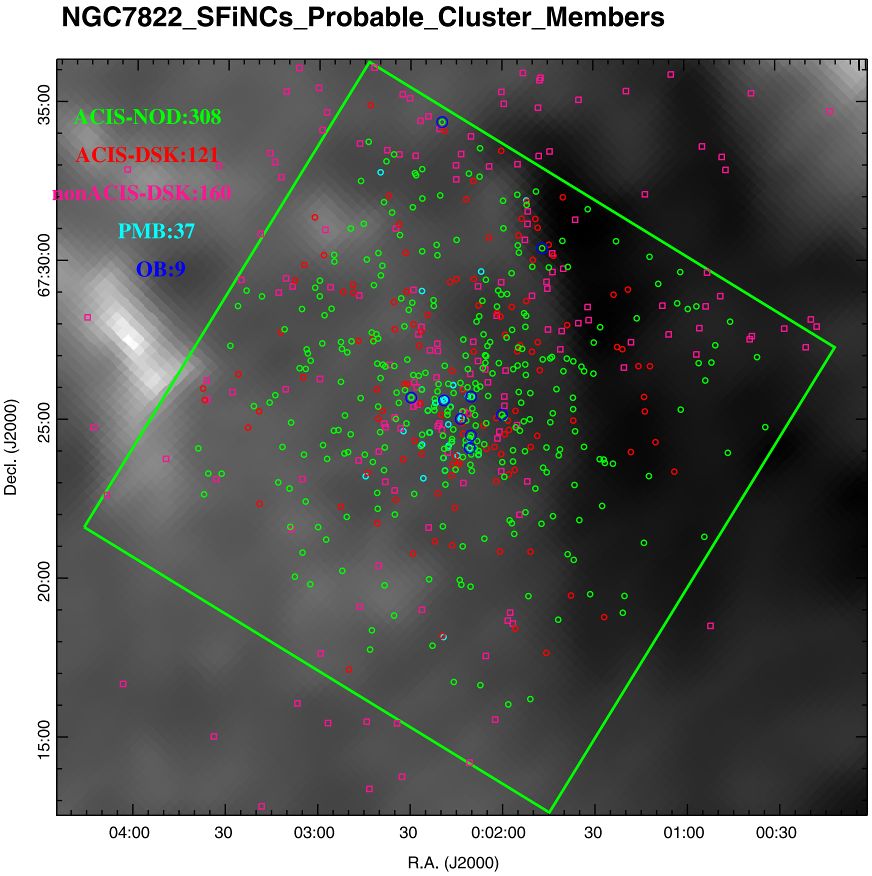

Figure 7. SFiNCs probable cluster members superimposed on the images taken by *AKARI*-FIS at 160 μm (for NGC 7822, IRAS 00013+6817, IRAS 20050+2720, NGC 7160, Cep OB3b) and *Herschel*-SPIRE at 500 μm (for the rest of the SFiNCs SFRs). An example is given for the Be59 SFR. The figure set presenting all SFiNCs SFRs is available in the online journal. The far-IR images trace the locations of the SFiNCs molecular clouds. The images are shown in inverted colors with logarithmic scales (denser clouds look darker, except for NGC 7160 where there is no cloud left). X-ray diskless YSOs, X-ray disky YSOs, non-X-ray disky YSOs, additional possible YSO members, and OB-type stars are marked as green circles, red circles, pink squares, cyan circles, and blue circles, respectively. *Chandra*-ACIS-I field of view is outlined by the green polygons. The figure legends provide information on the numbers of the SFiNCs YSOs. Since many "PMB" YSOs (cyan) are parts of visual double/multiple X-ray systems, their symbols are often covered up by the nearby ACIS-DSK/NOD symbols. For NGC 2068-2071, Mon R2, GGD 12-15, Cep OB3b, and Cep C, a handful of non-X-ray disky SPCMs located outside the boundaries of the current FIR images are not shown in these figures. The SPCM spatial distributions with expanded FOVs can be seen in Figure 17.

(The complete figure set (22 images) is available.)

based on their ambiguous SED shapes), a hundred "PMB" sources with very weak X-ray counterparts, and two hundred weak X-ray sources, for which their X-ray median energy is inconsistent with their NIR colors. The final SFiNCs YSO member list comprises 8492 sources.

4.2. Catalog of SFiNCs Probable Cluster Members

Tables 7 and 8 provide the list of 8492 SFINCs probable cluster members (SPCMs) and their main IR and X-ray properties. In this list, 66%, 30%, and 4% were classified as disky ("DSK" in column 11 of Table 8), diskless ("NOD"), and "PMB" members, respectively. Their reported properties include source names and positions, 2MASS NIR and *Spitzer*-IRAC MIR photometry, *Chandra*-ACIS-I X-ray net counts, median energies, incident fluxes, column densities, and intrinsic luminosities, apparent IRAC SED slopes, visual source extinctions, and stellar ages. The IRAC IR and X-ray properties of the SFiNCs SPCMs were excerpted from Tables 6, 3, and 4. Also provided are: the positional flag indicating whether the SPCM source lies within the *Chandra*-ACIS field of view (FOV); the flag indicating an association with an OB-type star and the related notes on the basic OB properties; as well as the flag and the related notes indicating complicated X-ray-IR stellar identifications often involving double or multiple sources.

The source extinctions (Table 8, column 12) were estimated for over half of the SFiNCs SPCMs with certain IR properties, including reliable NIR photometric measurements, using the NIR color–color method described in Getman et al. (2014a). The stellar ages (Table 8, column 13) were estimated for 22% of the SPCMs, whose NIR and X-ray properties satisfy certain criteria discussed in Getman et al. (2014a). This age estimator, called *AgeJX*, is based on an empirical X-ray luminosity–mass relation calibrated to well-studied Taurus PMS stars (Telleschi et al. 2007) and to theoretical evolutionary tracks calculated by Siess et al. (2000). While individual *AgeJX* values are very noisy, median ages for stellar clusters, such as the MYStIX clusters, are reasonably precise (Getman et al. 2014a).

4.3. Spatial Distribution of SPCMs

Figure 7 shows the spatial distributions of different classes of SPCMs superimposed on the far-infrared (FIR) images of the SFiNCs fields taken by *AKARI*-FIS at 160 μm (for NGC 7822,

Table 7
SFiNCs Probable Cluster Members: IR Photometry

Region (1)	Source (2)	R.A. (deg) (3)	Decl. (deg) (4)	2MASS (5)	JHK_s (mag) (6)	NIR_Fl (7)	IRAC (8)	IRAC mags (mag) (9)
NGC 7822	000033.87+672446.2	0.141150	67.412846	00003378+6724462	15.19 ± 0.05 13.58 ± 0.04 12.89 ± 0.03	AAA000	G118.0624+05.0235	12.38 ± 0.01 12.26 ± 0.01 … …
NGC 7822	000036.43+672658.5	0.151798	67.449596	00003633+6726582	13.68 ± 0.03 12.64 ± 0.03 12.17 ± 0.03	AAA000	G118.0737+05.0586	11.78 ± 0.00 11.73 ± 0.00 … …
NGC 7822	000045.20+672805.8	0.188345	67.468297	00004532+6728055	13.90 ± 0.03 12.85 ± 0.03 12.45 ± 0.03	AAA000	G118.0915+05.0742	12.06 ± 0.01 11.98 ± 0.01 … …
NGC 7822	000046.19+672358.2	0.192477	67.399503	00004605+6723575	14.08 ± … 13.01 ± 0.04 12.60 ± 0.03	UAA0cc	G118.0791+05.0063	12.19 ± 0.01 12.16 ± 0.03 … …
NGC 7822	000050.10+672721.4	0.208781	67.455954	00005018+6727204	15.09 ± 0.05 13.89 ± 0.04 13.42 ± 0.04	AAA000	G118.0967+05.0603	13.01 ± 0.01 12.92 ± 0.01 … …
NGC 7822	000051.39+672648.8	0.214161	67.446914	00005151+6726487	14.66 ± 0.04 13.33 ± 0.04 12.89 ± 0.03	AAA000	G118.0970+05.0513	12.55 ± 0.01 12.40 ± 0.01 … …
NGC 7822	000053.45+672615.0	0.222725	67.437501	00005355+6726148	15.43 ± 0.06 13.99 ± 0.05 13.34 ± 0.04	AAA000	G118.0984+05.0415	12.79 ± 0.02 12.72 ± 0.01 … …
NGC 7822	000054.01+672119.8	0.225079	67.355504	00005405+6721190	15.41 ± 0.05 14.03 ± 0.04 13.56 ± 0.05	AAA000	G118.0830+04.9607	13.00 ± 0.01 12.87 ± 0.01 … …
NGC 7822	000055.58+672647.8	0.231621	67.446638	00005552+6726466	15.30 ± 0.05 13.96 ± 0.04 13.56 ± 0.05	AAA000	G118.1032+05.0494	13.05 ± 0.02 12.96 ± 0.01 … …
NGC 7822	000056.24+672835.1	0.234343	67.476426	00005640+6728347	16.19 ± 0.09 15.00 ± 0.08 14.30 ± 0.06	AAAccc	G118.1104+05.0786	13.71 ± 0.02 13.65 ± 0.02 … …

Note. This table is available in its entirety (8492 SFiNCs probable cluster members across the 22 SFiNCs SFRs) in the machine-readable form in the online journal. A portion is shown here for guidance regarding its form and content. Column 1: SFiNCs SFR name. Column 2: source's IAU designation. Columns 3–4: R.A. and decl. in decimal degrees (J2000.0). Column 5: 2MASS source label. Column 6: 2MASS photometry in the *J*-, *H*-, and K_s-bands, respectively. Column 7: 2MASS photometry quality and confusion/contamination flag. Columns 8–9: IRAC source label and IRAC photometry in the [3.6], [4.5], [5.8], and [8.0] bands, respectively. These quantities were excerpted from Table 6.

(This table is available in its entirety in machine-readable form.)

Table 8

SFiNCs Probable Cluster Members: Main X-Ray and Other Properties

Region (1)	Source (2)	ACIS Label (3)	XFOV flag (4)	$C_{t,\mathrm{net}}$ (cts) (5)	E_{median} (keV) (6)	$\log(PF_t)$ (ph cm^{-2} s^{-1}) (7)	$\log(N_H)$ (cm^{-2}) (8)	$\log(L_{\mathrm{tc}})$ (erg s^{-1}) (9)	α_{IRAC} (10)	Class (11)	A_V (mag) (12)	*AgeJX* (Myr) (13)	OB[a] flag (14)	*Id*[b] flag (15)
NGC 7822	000033.87+672446.2	c2	1	30.5	2.62	−5.16	22.4	30.94	−2.05 ± 0.04	NOD	8.7	…	…	…
NGC 7822	000036.43+672658.5	c11	1	71.9	1.88	−5.06	22.1	30.79	−2.30 ± 0.02	NOD	3.8	…	…	…
NGC 7822	000045.20+672805.8	c24	1	19.2	1.66	−5.64	…	…	−2.21 ± 0.04	NOD	3.6	…	…	…
NGC 7822	000046.19+672358.2	c26	1	30.2	1.58	−5.45	21.8	30.25	−2.38 ± 0.11	NOD	…	…	…	…
NGC 7822	000050.10+672721.4	c31	1	9.1	1.77	−5.98	22.1	29.90	−2.19 ± 0.05	NOD	4.9	2.5	…	…
NGC 7822	000051.39+672648.8	c32	1	38.3	2.12	−5.36	22.2	30.63	−1.92 ± 0.04	NOD	5.7	…	…	…
NGC 7822	000053.45+672615.0	c36	1	56.5	2.37	−5.20	22.3	30.82	−2.23 ± 0.10	NOD	7.4	…	…	…
NGC 7822	000054.01+672119.8	c39	1	45.5	2.37	−5.21	22.3	30.81	−2.01 ± 0.04	NOD	6.2	…	…	…
NGC 7822	000055.58+672647.8	c41	1	12.9	2.08	−5.84	22.3	30.21	−2.15 ± 0.09	NOD	5.6	4.3	…	…
NGC 7822	000056.24+672835.1	c42	1	40.6	3.00	−4.93	22.5	31.25	−2.29 ± 0.13	NOD	…	…	…	Y

Notes. This table is available in its entirety (8492 SFiNCs probable cluster members across the 22 SFiNCs SFRs) in the machine-readable form in the online journal. A portion is shown here for guidance regarding its form and content. Column 1: SFiNCs SFR name. Column 2: source's IAU designation. Column 3: ACIS sources' label. Column 4: a flag indicating whether the source is located inside (XFOV = 1) or outside (XFOV = 0) the *Chandra*-ACIS-I field of view. Columns 5–9: the main X-ray properties of the SFiNCs YSO excerpted from Tables 3 and 4. These include net counts, median energy, incident X-ray photon flux, column density, and intrinsic luminosity. All quantities were computed in the total (0.5–8) keV band. Column 10. apparent SED slope measured in the IRAC wavelength range from 3.6 to 8.0 μm. Column 11. YSO class: diskless ("NOD"), disky ("DSK"), possible member without a disk class ("PMB"). The suffix "FRG" indicates that the source could be a foreground star or a YSO member of the region. Columns 12–13: source extinction in the *V*-band and stellar age estimated using the methods of Getman et al. (2014a). Column 14: OB flag indicating whether the source is associated with a known OB-type star from the catalogs of Skiff (2009) and/or SIMBAD. If the flag = "Y," the related information on the OB star' name, spectral type, and primary catalog of origin is placed in the note section of this table. Column 15: flag "Y" indicates that the X-ray-IR source match was rejected by the tool match_*xy* but was reinstated as a legitimate match upon the visual inspection. Such cases are often associated with sources' binarity and multiplicity. The related comments are given in the note section of this table.

[a] Notes on individual OB-type stars, including OB name, spectral type, and primary catalog of origin. NGC 7822 000146.83+673025.8: BD+66 1673; O5V((f))n from SKIFF. NGC 7822 000200.07+672511.5: 2MASS J00020012+6725109; B3V from SKIFF. NGC 7822 000210.16+672545.5: BD+66 1674; B0IIIn from SKIFF. NGC 7822 000210.24+672432.3: BD+66 1675; O7V from SKIFF. NGC 7822 000219.06+672538.5: NGC 7822 x; O9 from SKIFF. NGC 7822 000219.68+673424.3: LS I+67 10; B1: from SKIFF. NGC 7822 000229.79+672543.7: NGC 7822 y; B3? from SKIFF. NGC 7822 000210.62+672408.6: 2MASS J00021063+6724087; B8III from SKIFF. NGC 7822 000213.58+672503.6: LS I+67 9; B0.5Vn from SKIFF. NGC 1333 032857.19+311419.1: BD+30 547; BV from SIMBAD. NGC 1333 032910.39+312159.2: [SVS76] NGC 1333 3; B5:V + F2: from SKIFF. NGC 1333 032919.81+312457.4: BD+30 549; B8/9V from SKIFF. NGC 1333 032909.63+312256.4: [SVS76] NGC 1333 7; B:III from SKIFF.

[b] Notes on specific X-ray-IR source matches, based on the visual inspection of the 2MASS, IRAC, and ACIS images. The "SERs highly overlap" comment means that the IR and X-ray sources look like single sources and their source extraction regions (SERs) highly overlap. The last two digits given at the end of the individual notes indicate whether the source's X-ray-IR properties are consistent with the trends of the X-ray incident photon flux vs. the *J*-band magnitude and the X-ray median energy vs. the $J - H$ color seen for the majority of the X-ray-IR pairs: "0"—inconsistent; "1"—consistent. NGC 7822 000056.24+672835.1: SERs highly overlap; 00. NGC 7822 000115.84+672813.1: X-ray is a v. double with c79; 2MASS is a single; SERs highly overlap; 11. NGC 7822 000127.37+672218.9: SERs highly overlap; 10. NGC 7822 000134.82+672152.3: SERs highly overlap; 10. NGC 7822 000136.77+672521.9: SERs highly overlap; 11. NGC 7822 000138.66+672800.6: SERs highly overlap; 01. NGC 7822 000141.10+672405.8: SERs highly overlap; 10. NGC 7822 000146.83+673025.8: SERs highly overlap; 01. NGC 7822 000151.85+673153.5: X-ray is a v. triple; 2MASS is a single; SERs highly overlap; 01. NGC 7822 000152.06+673156.1: X-ray is a v. triple with c279 and c274.

(This table is available in its entirety in machine-readable form.)

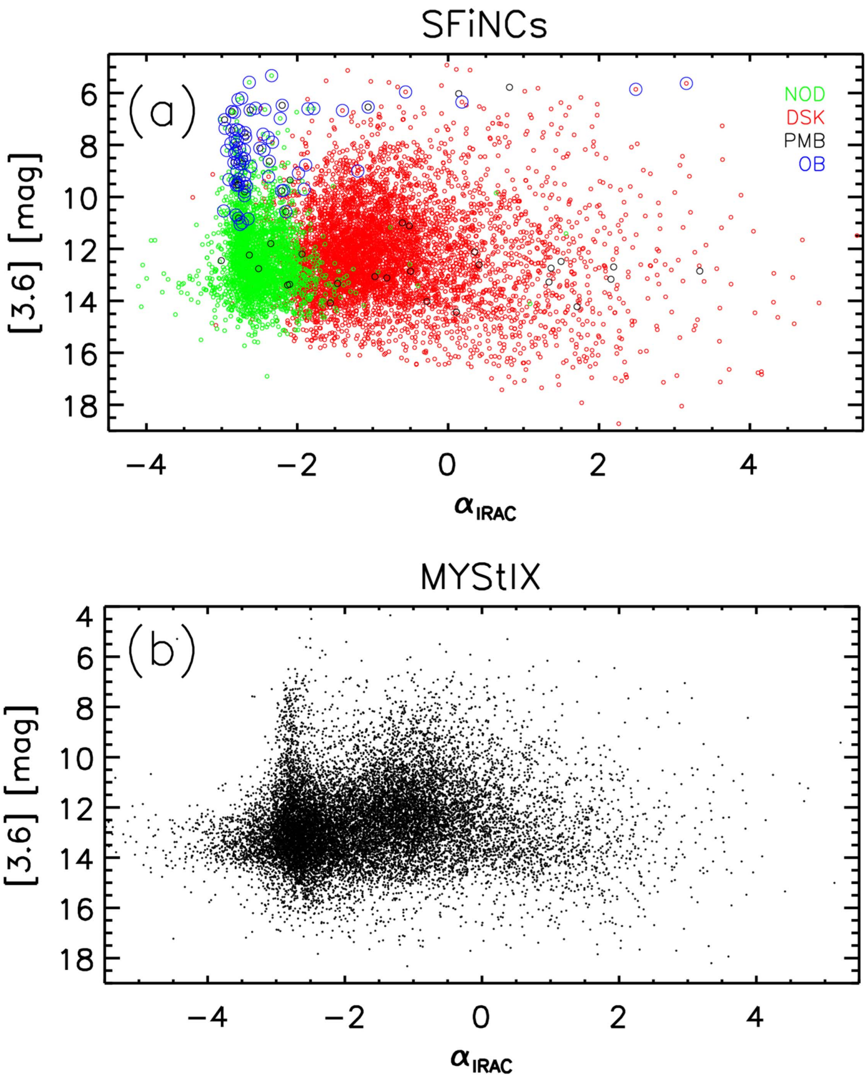

Figure 8. Examples of some of the global apparent and intrinsic MIR, NIR, and X-ray properties of the SFiNCs (upper panels) and MYStIX (lower panels) probable cluster members. These MYStIX quantities are tabulated in Broos et al. (2013) and Getman et al. (2014a). The SFiNCs SPCMs are color-coded according to their classes: diskless YSOs in green, disky YSOs in red, YSOs without disk classification in black, and OB-type stars in blue. ((a), (b)) MIR [3.6] magnitude vs. apparent IRAC SED slope. ((c), (d)) NIR $J-H$ color vs. X-ray median energy. ((e), (f)) NIR K-band magnitude vs. X-ray net counts. ((g), (h)) NIR absolute J-band magnitude corrected for source extinction vs. X-ray intrinsic source luminosity. ((i), (j)) Stellar age vs. visual source extinction.

(The complete figure set (5 images) is available.)

IRAS 00013+6817, IRAS 20050+2720, NGC 7160, and Cep OB3b) and *Herschel*-SPIRE at 500 μm (for the rest of the SFiNCs SFRs). The images trace the locations of the SFiNCs molecular clouds. Upon the inspection of this figure a few noteworthy items emerge.

First, it is important to stress here that the frequent apparent prevalence of disky populations in SFiNCs is due to the combination of two effects: an astrophysical from the youth of many SFiNCs regions; and an observational as a sample selection bias from the higher sensitivity of the *Spitzer*-IRAC observations (primary disky selector) to low-mass and/or extremely absorbed YSOs compared to the *Chandra*-ACIS observations (primary diskless selector). In the future SFiNCs studies, care must be taken to account for the unseen YSO populations using the XLF/IMF analyses, as it was done in MYStIX (Kuhn et al. 2015b).

Second, for many relatively young SFRs (e.g., IRAS 00013+6817, LkHα 101, ONC Flank fields, OMC 2-3, Mon R2, GGD 12-15, Serpens Main, IRAS 20050+2720, LDN 1251B, Cep A, and Cep C), the disky SPCMs often lie projected close to the molecular structures whereas the diskless SPCMs are often more widely distributed around the clouds suggesting processes of continuous star formation or possibly several episodes of a rapid star formation followed by kinematic drifting over several million years (Feigelson 1996). Some of the distributed YSOs are likely young stars that have been dynamically ejected from star-forming clouds (Bate et al. 2003).

Third, the efficacy of the X-ray selection can be immediately noticed in cases of relatively older SFRs: for instance, the apparent number of diskless YSOs becomes comparable or higher than that of the disky YSOs in the revealed rich

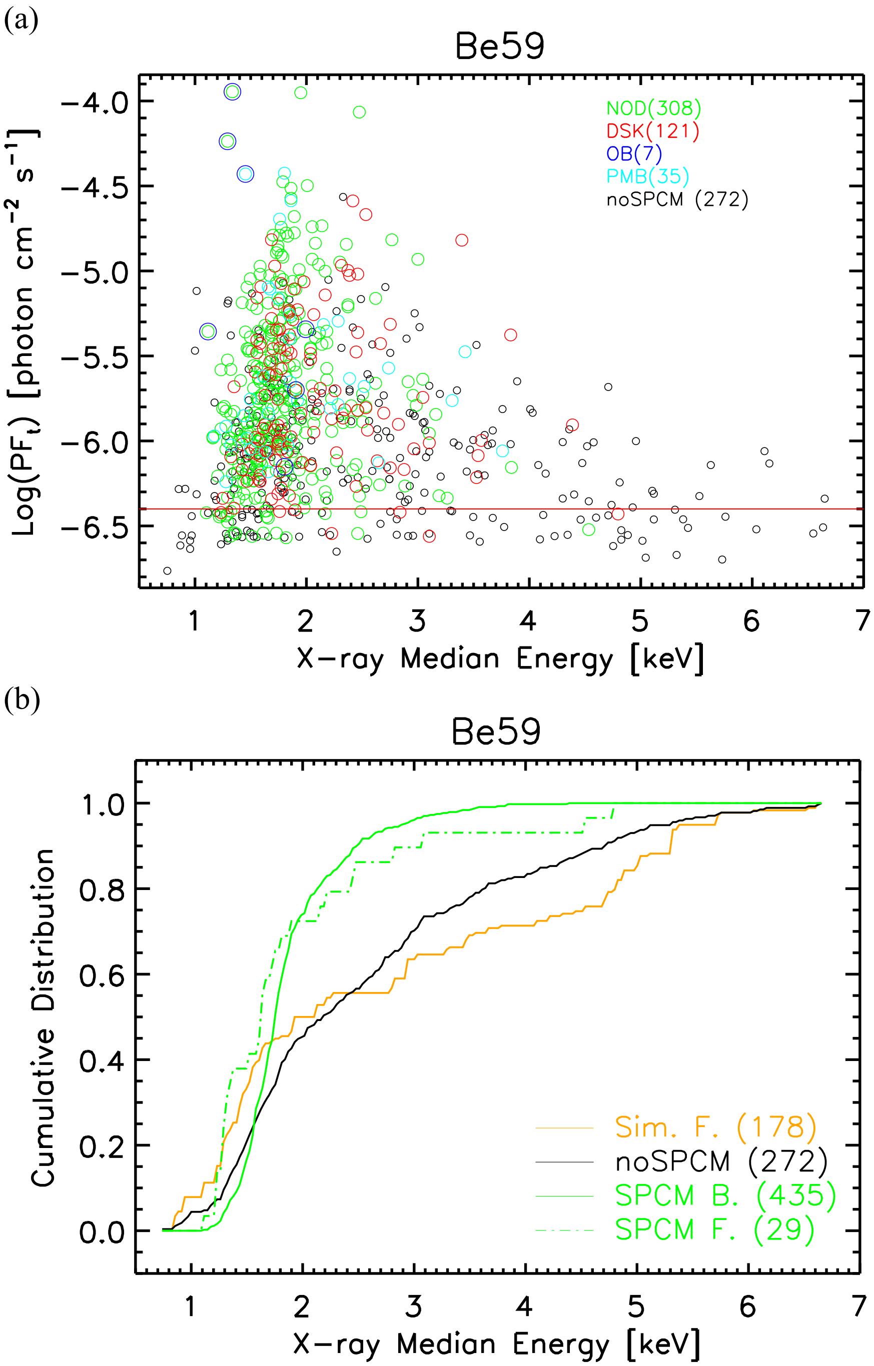

Figure 9. Comparison between the bright and faint X-ray SPCMs. An example is given for the Be59 SFR. The figure set presenting all SFiNCs SFRs is available in the online journal. (a) Apparent X-ray photometric flux vs. X-ray median energy. All ACIS-I X-ray SPCM and non-SPCM sources are plotted. Diskless, disky, OB-type, and PMB SPCMs are marked as green, red, blue, and cyan circles, respectively. Non-SPCMs are in black. Bright and faint X-ray SPCMs are separated by the red line. (b) Cumulative distributions of X-ray median energy are compared among the bright X-ray SPCMs (solid green), faint X-ray SPCMs (dashed green), non-SPCMs (black), and simulated faint X-ray sources with spurious 2MASS matches produced by the random position shifting via 100 draws (orange). The figure legends provide numbers of plotted source samples.

(The complete figure set (22 images) is available.)

subclusters of the IC 348, ONC Flank N, and Cep OB3b SFRs, and undoubtedly predominant in the oldest SFiNCs SFR NGC 7160. The X-ray selection also plays the major role in discovering stellar clusters in areas with strong IR nebular background: for instance, the central parts of the rich stellar subclusters in Mon R2 and Sh 2-106 remain undetected in purely IR studies (compare Figure 7 of this paper with Figure 1 of Gutermuth et al. 2009).

4.4. IR and Optical Color–Magnitude and Color–Color Diagrams

The positions of the SPCM sources in the NIR color–magnitude and color–color diagrams (Figures 10 and 11) are consistent with the expected loci of PMS stars, i.e., to the right (on the color–magnitude) and generally above and to the right (on the color–color diagrams) from the unabsorbed 3 and

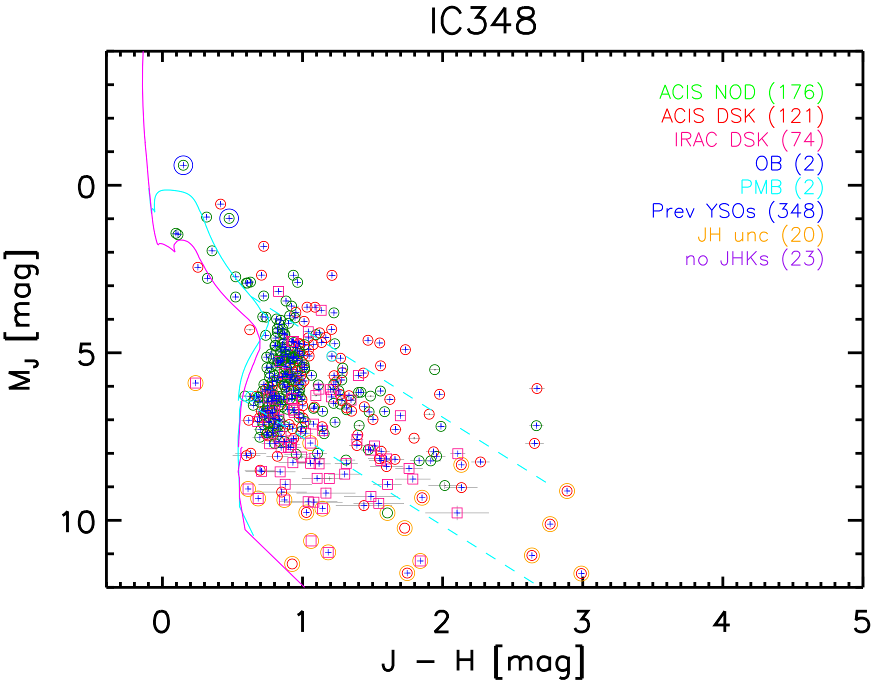

Figure 10. 2MASS color–magnitude diagrams in J- and H-bands for SPCMs stratified by YSO class. An example is given for IC 348 SFR. The figure set presenting other SFiNCs SFRs is available in the online journal. SPCM sources are color-coded according to their YSO class: IRAC disky (pink squares), ACIS disky (red circles), ACIS diskless (green circles), PMBs (cyan circles), and OB-type stars (blue circles). Sources that have uncertain NIR magnitudes are additionally marked by large orange circles (one or more NIR magnitudes are often upper limits). SPCMs that have been listed in previous YSO catalogs are further marked by small blue crosses. The unabsorbed 3 Myr (cyan) and 10 Myr (magenta) PMS isochrones are from Bressan et al. (2012) and Baraffe et al. (2015) for $M > 0.1\ M_\odot$ and $M < 0.1\ M_\odot$, respectively. In the case of 3 Myr isochrones, their $A_V = 20$ mag reddening vectors (using the extinction law from Cardelli et al. 1989) for 0.1 and 1 $M_\odot$ are shown as dashed cyan lines. Uncertainties on the J and H magnitudes are shown as gray error bars. The legends indicate the numbers of plotted sources; the number of SPCMs without 2MASS counterparts is also indicated in purple. The values on y-axis are absolute magnitudes (corrected for distance).

(The complete figure set (22 images) is available.)

10 Myr (cyan and magenta) PMS isochrones. Many SPCM populations are subject to a wide range of source extinction; for instance, A_V changes from 0 to >20 mag in the NGC 1333 and NGC 2068-2071 SFRs. Some SFRs are subject to a uniform foreground absorption of $A_V \gtrsim 2$ mag, such as Be59, LkHα 101, and Mon R2. For some SFRs, such as NGC 7160 and the ONC Flank sub-regions, their SPCM populations are mainly unobscured. For the oldest SFiNCs SFR, NGC 7160, the color–magnitude positions of a relatively large fraction of diskless SPCMs are clustered around the 10 Myr PMS isochrone; this is consistent with the average age of 10–13 Myr previously estimated for the sample of bright optical stars (Sicilia-Aguilar et al. 2004; Bell et al. 2013). For the most distant SFRs (RCW 120 and Sh 2-106) the SPCM data sets are sensitive down to only ~0.8–1 $M_\odot$, whereas for the nearest SFRs (NGC 1333 and IC 348) the SPCM data sets comprise many low-mass YSOs with masses $\lesssim 0.1\ M_\odot$.

Our YSO selection method (Section 4.1), although benefiting from the synergy of multiple data components (such as X-ray and/or NIR and/or MIR photometry and spatial distribution), is flexible enough to allow reasonably reliable YSO classification for some cases of missing data, such as non-X-ray disky YSOs, non-IR PMB YSOs, and X-ray+MIR YSOs with uncertain NIR data. With regards to the latter, it is important to note here that the positions of the SPCMs with uncertain NIR magnitudes (orange circles) on the NIR diagrams should be considered with caution because many of them remain undetected in the 2MASS J- and/or H-bands (typically due to high absorption and/or nebulosity) and their J-, H-band magnitudes are often reported by 2MASS as upper limits. For instance, several disky SPCMs in OMC 2-3 (## 105, 141, 420, 423, 430, 439, and 460) have abnormal positions on the NIR color–magnitude diagram (Figures 10), to the left of the 10 Myr PMS isochrones. Such positions cannot be trusted due to the uncertain NIR photometry. Nevertheless, the detailed inspection of SPCM Atlas (Appendix B) and other auxiliary data provide strong evidences for YSO nature of these sources, such as the spatial location against the OMC molecular filaments and cores, the X-ray variability and high X-ray absorption, the IR SED shapes (in the K_s and IRAC bands) reminiscent of Class II/I YSOs, and the previous YSO identification by Megeath et al. (2012).

A few relatively bright ($M_J \sim 0$ mag) and red ($J - H > 2$ mag) outliers can be noticed on the NIR color–magnitude diagram (Figures 10); these are the SPCM sources #136 in LkHα 101, #105 in Sh 2-106, and #103 in Serpens Main. While the first two are clearly associated with the main ionizing sources of the LkHα 101 and Sh 2-106 SFRs (see SPCM Atlas in Appendix B), the latter is a non-X-ray source previously identified by Winston et al. (2009, their source #71) as a Class II YSO of spectral type M9. Its unusually high IR brightness for an M9 PMS star, red colors, disky SED, and spatial location at the outskirts of the main cluster (see SPCM Atlas in Appendix B) suggest that the source could be considered as a candidate AGB star unrelated to the region. A small contamination of the SPCM sample by AGBs is expected (Section 3.6).

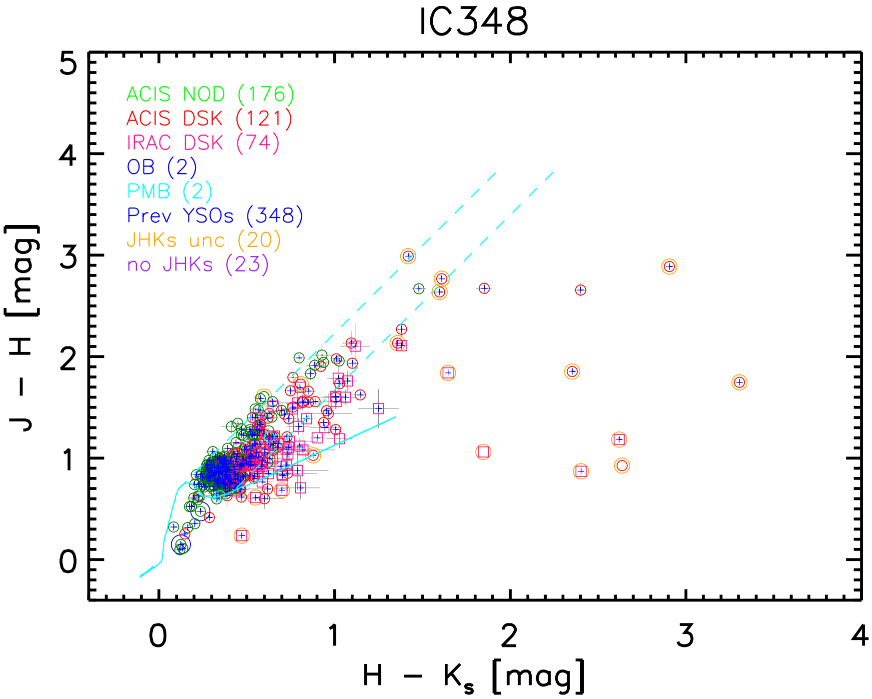

Figure 11. 2MASS color–color diagrams in JHK_s bands for SPCMs stratified by YSO class. An example is given for IC 348 SFR. The figure set presenting other SFiNCs SFRs is available in the online journal. SPCM sources are color-coded according to their YSO class: IRAC disky (pink squares), ACIS disky (red circles), and ACIS diskless (green circles), PMBs (cyan circles), and OB-type stars (blue circles). Sources that have uncertain NIR magnitudes are additionally marked by large orange circles (one or more NIR magnitudes are often upper limits). SPCMs that have been listed in previous YSO catalogs are further marked by small blue crosses. The solid cyan curve shows the locus of unabsorbed 3 Myr stars from Bressan et al. (2012) joined with the baseline for de-reddening disky YSOs Getman et al. (2014a). The $A_V = 30$ mag reddening vectors (using the extinction law from Cardelli et al. 1989) for 0.1 and 0.8 $M_\odot$ are shown as dashed cyan lines. Uncertainties on the individual photometric colors are shown as gray error bars. The legends indicate the numbers of plotted sources; the number of SPCMs without 2MASS counterparts is also indicated, in purple color.

(The complete figure set (22 images) is available.)

The positions of SPCMs in the MIR color–magnitude and color–color diagrams (Figures 12, 13, 14, 15) generally agree with our independent IR SED classification of objects as disk-bearing (red and pink) and diskless (green) based on comparison with IC 348 stars (second stage of our membership analysis in Section 4.1). On the MIR color–magnitude diagram (Figures 12), the diskless SPCMs generally follow well the locus of the diskless IC 348 stars (cyan). On the MIR color–color diagrams, the majority of SPCMs with their disk classification are consistent with the simple color criteria that diskless stars have $K_s - [3.6] \lesssim 0.6$ mag, $[3.6]–[4.5] \lesssim 0.2$ mag, $[4.5]–[5.8] \lesssim 0.2$ mag, and $[5.8]–[8.0] \lesssim 0.2$ mag. Disky sources with discrepant locations on such diagrams may represent cases of transition disks; for instance, the SPCM sources ## 109, 231, and 258 in the well-studied IC 348 SFR (see SPCM Atlas in Appendix B).

Serpens South, likely the youngest SFiNCs SFR, harbors an exceptionally rich population of disky SPCMs that lies projected against an IR dark molecular cloud. A dozen disky SPCMs in Serpens South have anomalously blue colors, such as $[4.5]–[5.8] < 0$ mag (Figure 14). These can be divided into two groups. The first group is composed of likely outflow candidate YSOs with elevated [4.5] emission from molecular shocks (Povich et al. 2013). These Serpens South SPCMs (## 158, 169, 255, 256, 379, 389, and 409) generally lie projected against the dense parts of the molecular filaments (see SPCM Atlas in Appendix B). The second group constitutes transition disk YSOs with an [8.0]-excess (## 199, 281, 430, and 603) that are typically located away from the dense filaments in the areas with low background nebular emission in the [8.0]-band. Another set of Serpens South disky SPCMs (such as ## 115, 119, 196, 251, 258, 295, 318, 343, and 413) has abnormally blue [5.8]–[8.0] colors (see SPCMs with $[5.8]–[8.0] \lesssim 0$ mag in Figure 15). These lie projected against the dense parts of the cloud and have SED shapes characterized by a flux rise in shorter following by a flux decline in longer IRAC bands (see SPCM Atlas). These are likely protostellar objects with the flux in the [8.0]-band strongly affected by an absorption from protostellar envelope, in the silicate band centered near 9.7 μm (Figure 7(a) in Povich et al. 2013).

Optical photometric data are generally not as useful for identifying YSOs as IR/X-ray data. They often suffer the problems of source crowding and background nebulosity and are biased toward unobscured YSOs. Nevertheless, Figure 16 shows the optical color–magnitude diagrams in the i- and z-bands for several SFiNCs SFRs with available SDSS coverage (Alam et al. 2015). For all these SFRs, the SDSS coverage is only partial due to the presence of diffuse nebula background from heated gas. On these diagrams, the positions of SPCMs are generally consistent with the expected PMS loci, i.e., to the right from the 10 and 100 Myr (magenta and blue) PMS isochrones. For some disky SPCMs, their location to the left from the 10–100 Myr PMS isochrones is inconsistent with their status of disky YSOs. This may point to discrepant optical magnitudes; for instance, some may possess disks at high inclination where the optical light is enhanced by scattering above the disk (Guarcello et al. 2010). It is interesting to note that for the NGC 2068-2071 SFR, both

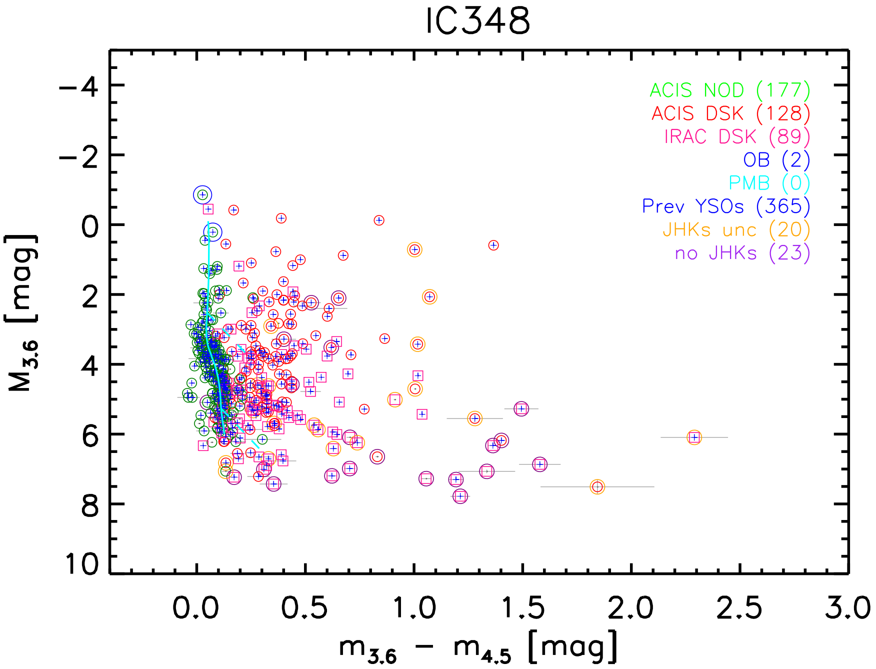

Figure 12. IRAC MIR color–magnitude diagrams in [3.6] and [4.5] for SPCMs stratified by YSO class. An example is given for IC 348 SFR. The figure set presenting other SFiNCs SFRs is available in the online journal. SPCM sources are color-coded according to their YSO class: IRAC disky (pink squares), ACIS disky (red circles), ACIS diskless (green circles), PMBs (cyan circles), and OB-type stars (blue circles). Sources that have uncertain NIR magnitudes are additionally marked by large orange circles (one or more NIR magnitudes are often upper limits) and sources without 2MASS counterparts are marked by large purple circles. For every SFiNCs SFR, the solid cyan curve represents the smoothed version of the locus of the IC 348 diskless SPCMs. The reddening vectors of $A_K = 2$ mag (using the extinction law from Flaherty et al. 2007), originating from the IC 348 locus at ~1 and 0.1 $M_\odot$ (according to the 3 Myr PMS models of Baraffe et al. 2015), are shown as dashed cyan lines. Uncertainties on the [3.6] and [4.5] magnitudes are shown as gray error bars. SPCMs that have been listed in previous YSO catalogs are further marked by small blue crosses. The legends indicate the numbers of plotted sources. The values on *y*-axis are absolute magnitudes (corrected for distance).

(The complete figure set (22 images) is available.)

the NIR and optical color–magnitude diagrams point to the presence of an older, perhaps foreground, PMS population.

In all diagrams above, the loci of the previously identified YSOs (blue +s), when available, are in agreement with the loci of SPCMs. The more detailed comparison with the previous YSO catalogs is given in Section 5.

4.5. Global Properties of SPCMs

For the entire SFiNCs SPCM sample, Figure 8 (upper panels) shows a few important independently measured basic MIR, NIR, and X-ray source characteristics (*JHKs* and [3.6] band magnitudes, X-ray net counts, and X-ray median energy), as well as a few derived using those and other quantities, X-ray luminosity, visual source extinction, absolute *J*-band magnitude, and stellar age. The relationships seen among these properties are in agreement with those of the MYStIX (bottom panels in Figure 8) and YSO samples obtained in previous studies of SFRs and thus lend confidence in our data and membership methods and the resulted SFiNCs SPCM catalog.

Specifically, panels (a) and (b) show bimodal distributions of the SFiNCs and MYStIX apparent IRAC SED slopes with peaks at around $\alpha_{\rm IRAC} \sim -1.3$ and $\alpha_{\rm IRAC} \sim -2.7$ corresponding to disky and diskless star populations, respectively. Such bimodality was reported in the PMS populations of other SFRs, for instance, Cha I cloud (Luhman et al. 2008) and σ Ori (Hernández et al. 2007). This is consistent with the disk classification scheme of Lada (1987).

But some outliers are present on these graphs. For instance, a few SPCMs classified as diskless have an unusually high slope, $\alpha_{\rm IRAC} > -1$. These include sources ## 109, 118 in Mon R2, ## 108, 144 in RCW 120, # 918 in Cep OB3b, and # 155 in OMC 2-3. All of these sources are located in regions that are subject to a moderate MIR nebular background emission. All lack photometry measurements in the [8.0] band; the two sources in Mon R2 lack photometry in both the [5.8] and [8.0] bands. The shapes of their IR SEDs in all but a single, longest IRAC band are consistent with stellar photospheres (see SPCM Atlas in Appendix B). This marginal IR excess can be attributed either to their physical evolutionary state as transition disk objects or to the problems in photometry measurements (inaccurate photometry in the longest band due to the prevalence of nebular background). We chose the latter case and classified these objects as diskless. At the other extreme, over 200 disky SPCMs have a relatively lower slope, $\alpha_{\rm IRAC} < -2$. A characteristic feature of their SEDs is a slight but consistent deviation of the SED shapes from stellar photospheres in two or more IR bands. The vast majority of these sources have been identified as disky YSOs in previous studies of the SFiNCs SFRs. For instance, a large number of such SPCMs is present in the NGC 2068-2071 SFR with the majority identified as disky by Megeath et al. (2012): ## 50, 65, 75, 87, 112, 160, 255, 258, 270, 282, 299, and 302 (see SPCM Atlas in Appendix B).

In panel (a), at the faint end of [3.6] ([3.6] $\gtrsim$ 15.5 mag), the points correspond to disky YSOs that are seen lying projected against the SFiNCs molecular structures; 76% of these faint, disky YSOs are associated with the very young Serpens South

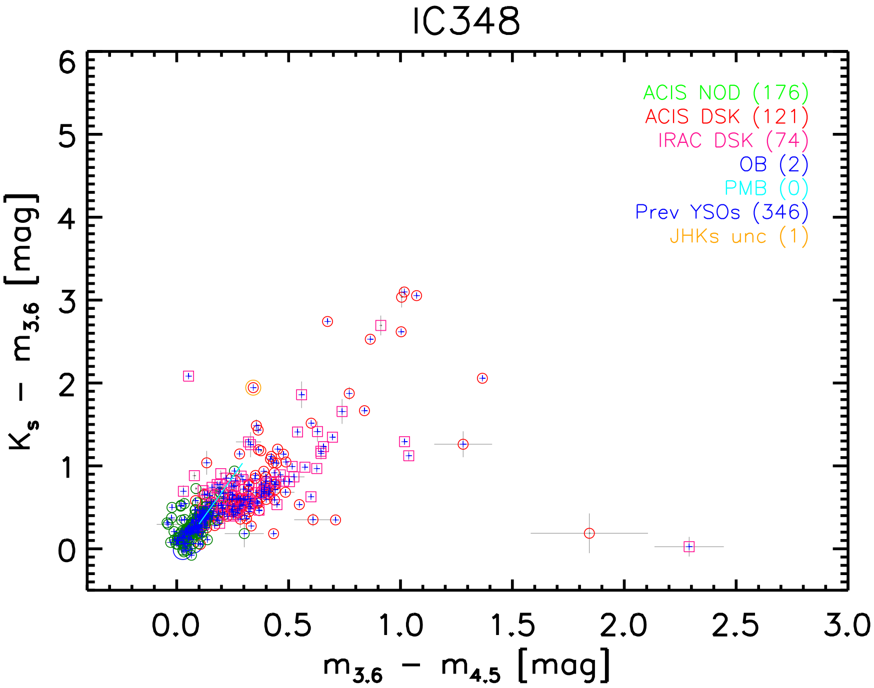

Figure 13. IRAC MIR color–color diagrams in K_s, [3.6], and [4.5] bands for SPCMs stratified by YSO class. An example is given for IC 348 SFR. The figure set presenting other SFiNCs SFRs is available in the online journal. SPCM sources are color-coded according to their YSO class: IRAC disky (pink squares), ACIS disky (red circles), ACIS diskless (green circles), PMBs (cyan circles), and OB-type stars (blue circles). Sources that have uncertain NIR magnitudes are additionally marked by large orange circles (one or more NIR magnitudes are often upper limits). The reddening vector of $A_K = 2$ mag (using the extinction law from Flaherty et al. 2007) is shown by the cyan line. Uncertainties on the individual photometric colors are shown as gray error bars. SPCMs that have been listed in previous YSO catalogs are further marked by small blue crosses. The legends indicate the numbers of plotted sources.

(The complete figure set (22 images) is available.)

SFR (Figure 7). At the bright end of [3.6] ([3.6] > 7 mag), many SFiNCs YSOs are identified as known OB-type stars; but a dozen more disky YSOs lie within this OB locus. The nearby OMC 2-3 SFR harbors the largest number of such objects (seven); these are SPCM sources ## 107, 115, 165, 170, 201, 438, and 441. Our visual inspection of the source's properties given in SPCM Atlas (Appendix B) suggests that all of these objects lie projected against the OMC molecular filament. Half of them have IR SEDs that show a precipitous flux rise with increasing IRAC wavelength (characteristic of Class I objects); the other half is characterized by shallower IRAC slopes (characteristic of Class II objects). For most of them SIMBAD lists a class of "Variable Star of Orion Type"; and for the Class II objects, SIMBAD provides a spectral type of early K-type stars. The most distant SFINCs SFR, Sh 2-106, harbors three of such objects (## 67, 231, 234); all listed as disky YSOs in previously published studies of the region. SPCM Atlas shows that these lie projected close to the center of the primary stellar cluster in Sh 2-106. While spectral types are not available for these objects, their bright IR magnitudes, spatial location close the giant molecular clumps, and steep IRAC slopes point toward the extreme youth and possibly high masses of these objects, especially for the X-ray emitting Class I protostar # 67. However, in the case of Sh 2-106 (an SFR close to the Galactic plane), where YSOs are observed against field population of AGB stars, a misclassification of an AGB as a bright IR YSO is also possible (Section 3.6). Specifically, the SPCM source # 234 whose SED shape is characterized by a sharp rise of flux through the NIR bands followed by a flux flattening through IRAC bands might be also considered as an AGB stellar candidate with dust-rich winds.

The NIR $J - H$ color and X-ray median energy of PMS stars are excellent surrogates for line-of-sight obscuration by dust and gas, respectively (e.g., Vuong et al. 2003; Getman et al. 2011). Panels (c) and (d) show that the dust-to-gas absorption relationships for the SFiNCs and MYStIX SFRs look very similar. The SFiNCs SPCMs without disk classifications ("PMB"), many of which are found at the centers of the SFiNCs stellar clusters affected by MIR nebular emission, have gas-to-dust ratios similar to those of other SPCMs. Since the $J - H$ color is also a surrogate for spectral type, its values for many known lightly/moderately absorbed OB-type members are shifted downwards with respect to the PMS locus. In their MYStIX science study of new protostellar objects in the MYStIX regions, Romine et al. (2016) used X-ray median energy >4.5 keV as a strict criterion to discriminate Class I protostars from Class II-III systems.

It is well known that PMS X-ray luminosities strongly correlate with stellar mass and bolometric luminosity. For instance, clear relationships are seen for YSOs in the Orion Nebula and Taurus SFRs (Preibisch & Feigelson 2005; Telleschi et al. 2007). The astrophysical cause of this relationship is poorly understood but could be related to the scaling of X-ray luminosity with surface area and/or stellar convective volume. The spread and the slope of this relationship are also subject to the variability, accretion, X-ray saturation, and age effects (Getman et al. 2014a). NIR magnitudes, such as J- or K-band, and X-ray net counts of PMS stars are good surrogates for bolometric luminosity (and mass) and X-ray luminosity, respectively. Panels (e) and (f) show the correlation of these

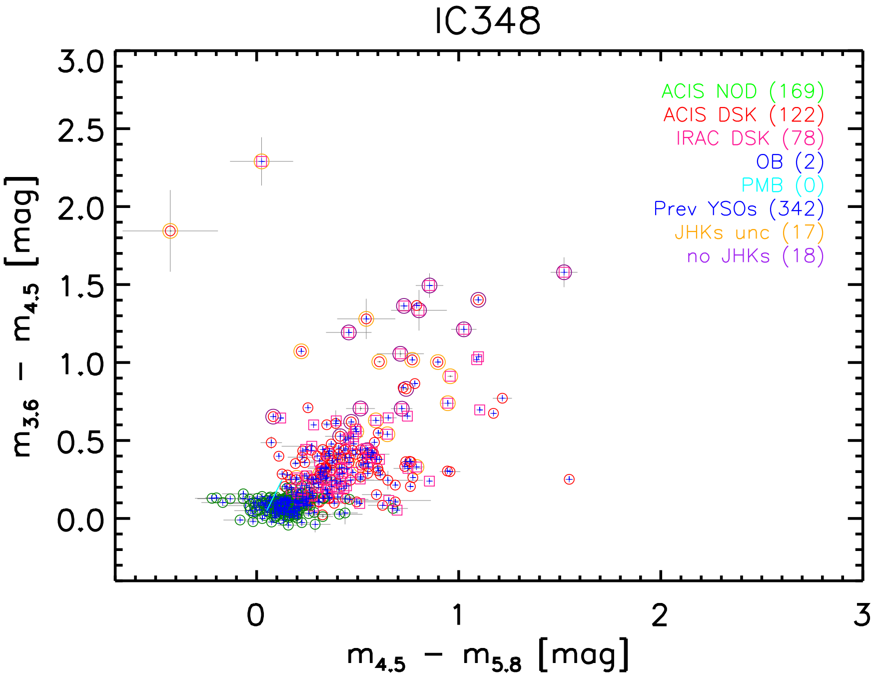

Figure 14. IRAC MIR color–color diagrams in [3.6], [4.5], and [5.8] bands for SPCMs stratified by YSO class. An example is given for IC 348 SFR. The figure set presenting other SFiNCs SFRs is available in the online journal. SPCM sources are color-coded according to their YSO class: IRAC disky (pink squares), ACIS disky (red circles), ACIS diskless (green circles), PMBs (cyan circles), and OB-type stars (blue circles). Sources that have uncertain NIR magnitudes are additionally marked by large orange circles (one or more NIR magnitudes are often upper limits) and sources without 2MASS counterparts are marked by large purple circles. The reddening vector of $A_K = 2$ mag (using the extinction law from Flaherty et al. 2007) is shown by the cyan line. Uncertainties on the individual photometric colors are shown as gray error bars. SPCMs that have been listed in previous YSO catalogs are further marked by small blue crosses. The legends indicate the numbers of plotted sources.

(The complete figure set (21 images) is available.)

apparent quantities, K-band magnitude versus X-ray net counts, whereas panels (g) and (h) present the correlation between the intrinsic J-band and X-ray luminosities. The statistical significance of these correlations were evaluated by testing the null hypothesis that the Kendall's τ coefficient is equal to zero. This test was made using the *corr.test* program from the R statistical software system.[10] The test shows statistically significant correlations for the data presented in all four panels, with the Kendall's τ p-values of <0.0001 for any of the panels. The observed τ values are −0.42, −0.36, −0.46, and −0.38 for panels (e), (f), (g), and (h), respectively. Both the K_s-$\log(NC)$ and M_J-$\log(L_{\rm tc})$ correlations are expressions of the same $\log(L_{\rm bol})-\log(L_X)$ relationship. From these plots, it is clearly seen that the OB-type stars do not follow this PMS relationship, in part due to the difference in X-ray production mechanisms. On the other hand, the location of the "PMB" YSOs on these plots are consistent with that of the diskless and disky PMS stars. On panels (g) and (h), the SFiNCs X-ray luminosities are systematically below the MYStIX luminosities due to closer distances with similar *Chandra* exposures.

Due to the depletion of molecular clouds and stellar kinematic drift, older YSOs are expected to exhibit lower interstellar absorptions than younger YSOs. Getman et al. (2014a) found that the stellar ages of the MYStIX YSOs are anticorrelated with the source extinction A_V (panel (j) here and Figure 4 in Getman et al.). A similar relationship was found for the YSOs in the Rosette SFR (Ybarra et al. 2013). And again, a similar $AgeJX - A_V$ relationship is seen for the YSOs in the SFiNCs SFRs (panel (i)). The SFiNCs disky YSOs are found to be on average younger than the SFiNCs diskless YSOs.

4.6. Comparison between Bright and Faint X-Ray SPCMs

As is mentioned in Section 3.2, our data reduction procedures produce very sensitive X-ray source catalogs that are undoubtedly subject to contamination by faint spurious X-ray sources. In this section, we demonstrate that the great majority of faint SPCMs are not spurious but are real YSOs.

Since the YSO selection for the vast majority of faint X-ray SPCMs relies on the presence of an IR counterpart (Section 4.1), it is important to verify that the faint X-ray SPCMs are not background fluctuations with spurious IR matches. The major steps of our test analysis here are as follows.

First, the X-ray SPCM source sample is divided into the bright and faint X-ray subsamples, as it is shown on the X-ray flux versus median energy diagram (analogous to an IR color–magnitude diagram; Figure 9(a)). For the SFiNCs SFRs with rich X-ray SPCM populations, the X-ray flux threshold for separating bright and faint X-ray SPCMs is set at the photometric flux level of $\log(PF_{\rm lim}) = -6.4$ photons cm^{-2} s^{-1}; but for the sparser populations, this threshold is raised to accumulate at least ∼20 SPCMs (if possible) within the faint subsample. The entire sample of faint X-ray SPCMs across 22 SFiNCs SFRs comprises 889 sources. Disregarding the faint "PMB" SPCMs located in the cluster centers of Mon R2, RCW 120, Sh 2-106, LkHα, and Cep A (about 50 sources in Figure 9(a)) that were shown to be likely cluster members using

---

[10] The *corr.test* tool is part of the *psych* package. The description of the package is available online at http://personality-project.org/r/psych/psych-manual.pdf.

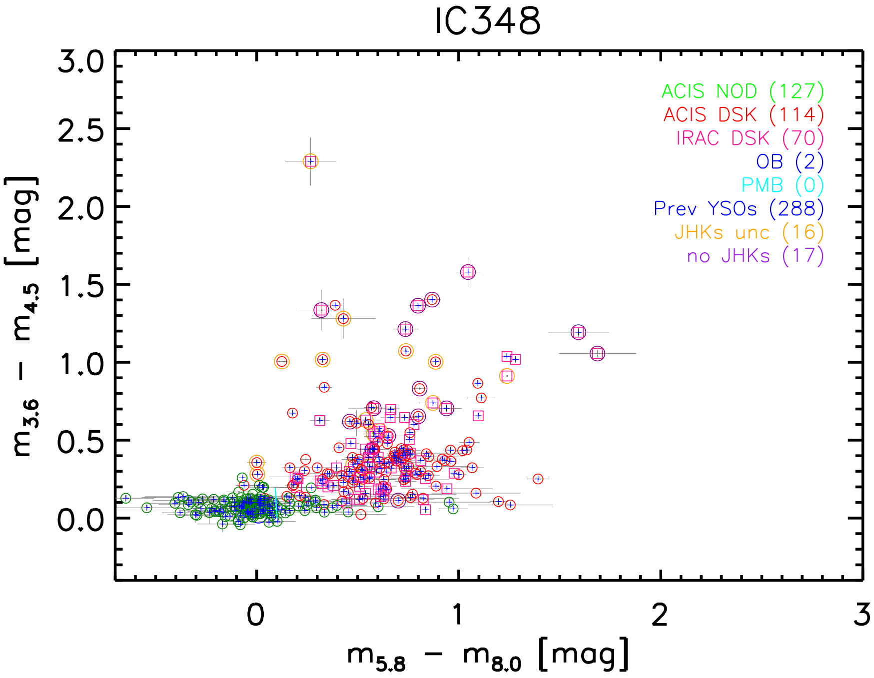

Figure 15. IRAC MIR color–color diagrams in [3.6], [4.5], [5.8], and [8.0] bands for SPCMs stratified by YSO class. An example is given for IC 348 SFR. The figure set presenting other SFiNCs SFRs is available in the online journal. SPCM sources are color-coded according to their YSO class: IRAC disky (pink squares), ACIS disky (red circles), and ACIS diskless (green circles). Sources that have uncertain NIR magnitudes are additionally marked by large orange circles (one or more NIR magnitudes are often upper limits) and sources without 2MASS counterparts are marked by large purple circles. The reddening vector of $A_K = 2$ mag (using the extinction law from Flaherty et al. 2007) is shown by the cyan line. Uncertainties on the individual photometric colors are shown as gray error bars. SPCMs that have been listed in previous YSO catalogs are further marked by small blue crosses. The legends indicate the numbers of plotted sources.

(The complete figure set (21 images) is available.)

the independent analysis in Section 4.1, among the remaining faint X-ray SPCMs, 94% and 99% have 2MASS and IRAC counterparts, respectively. It is important to note here that the non-SPCM sample (shown in black) is expected to be composed of different classes of X-ray sources, including AGNs, stellar background/foreground contaminants, as well as spurious X-ray sources.

Second, simulated sets of spurious ACIS-2MASS matches are constructed via 100 Monte-Carlo draws by randomly shifting the positions of all real X-ray ACIS-I sources (including both SPCM and non-SPCM X-ray sources) within $r = [20\text{–}50]''$ distance of the true source's positions and by applying the trivial matching of source pairs within the constant $2''$ radius (first step in Section 3.5). Across the 100 simulated sets, the faint X-ray sources (with their X-ray fluxes below $PF_{\rm lim}$) that appear to have "spurious" 2MASS matches in such simulations are combined into the "simulated faint" source subsample. The cumulative distributions of the X-ray median energy (an excellent surrogate for the line-of-sight obscuration) are further compared among different source subsamples.

In Figure 9(b), the cumulative distributions of the X-ray median energy (*ME*) are compared among the real X-ray SPCMs (bright and faint given in green color), non-SPCMs (black), and simulated faint X-ray sources with spurious 2MASS matches (orange). There are two independent supporting lines of evidence suggesting that the vast majority of the faint SPCMs are not spurious but true YSO sources.

First, judging from the source numbers (provided in the figure legends), the number of the expected (simulated) faint sources with spurious matches typically comprise only several percent of the real faint SPCM sources. For instance, in the case of Be59, we expect 178/100 spurious sources among 29 faint SPCMs, which is only 6%. Across the entire set of 22 SFiNCs SFRs, the median fraction of spurious sources among the faint SPCMs is only 7% with an interquartile range of 5%–10%.

Second, it is clearly seen that the *ME* distributions of the simulated faint sources with spurious X-ray-IR matches are similar to those of the real X-ray non-SPCM sources; whereas the *ME* distributions of the faint SPCMs are found to be significantly lower and often (but not always) consistent with those of the bright SPCMs. For the cases when the *ME* distributions of the faint SPCMs are inconsistent with (systematically higher than) those of bright SPCMs, such as, OMC 2-3, Mon R2, Serpens South, IRAS 20050+2720, IC 5146, and Cep A, an additional analysis comparing the distributions of R.A. and decl. for the same source samples was performed (graphs are not shown). The results of this analysis indicate that the spatial distributions of both the faint and bright SPCMs are inconsistent with the relatively uniform distributions of non-SPCMs, but are either consistent with each other or the fainter SPCMs are found to be more clustered in/around the SFiNCs molecular clouds, suggesting that the fainter SPCMs are more absorbed YSOs.

Considering that all faint SPCMs have passed through our rigorous YSO selection (Section 4.1), we believe that the vast majority ($\gtrsim$90%) of the faint X-ray SPCMs are real YSOs.

5. Comparison with Previously Published YSO Catalogs

The SFiNCs SPCM catalog can be compared to the YSO catalogs independently derived in earlier published studies. The previously published YSO catalogs are abbreviated here as Pub. Here we are not principally interested in evaluating

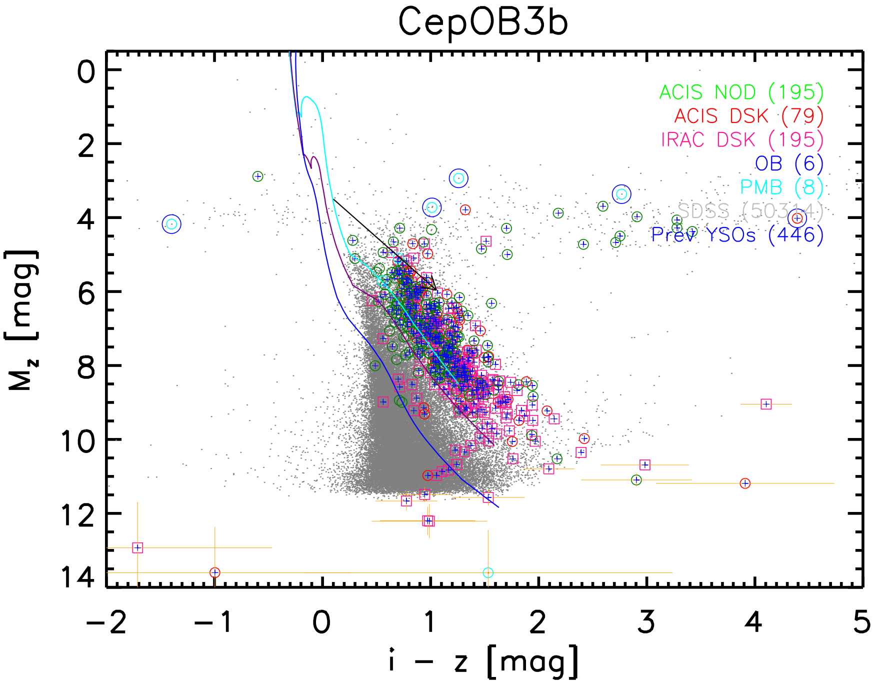

Figure 16. SDSS optical color–magnitude diagrams in the *I* and *Z* bands for SPCMs stratified by YSO class. The SDSS DR 12 data (Alam et al. 2015) are available for the Orion and Cepheus as well as IC 5146 and Serpens Main SFiNCs regions. For any of those SFRs, the SDSS coverage is only partial due to the presence of diffuse nebular background. An example is given here for the Cep OB3b SFR. The figure set presenting other SFiNCs SFRs with available SDSS data can be found in the online journal. All SPCMs with available SDSS photometry are plotted as colored circles. All SDSS sources in the field that have photometric errors below 0.2 mag are plotted as gray dots. The SPCM sources are color-coded according to their YSO class: IRAC disky (pink squares), ACIS disky (red circles), ACIS diskless (green circles), PMBs (cyan circles), and OB-type stars (blue circles). Error bars (orange) are shown for SPCMs with photometric errors above 0.2 mag. The unabsorbed 3 Myr (cyan), 10 Myr (magenta), and 100 Myr (blue) PMS isochrones are from Bressan et al. (2012). Reddening vector $A_V = 5$ mag (using the extinction law from Cardelli et al. 1989) is shown as the black arrow. SPCMs that have been listed in previous YSO catalogs are further marked by small blue crosses. The legends indicate the numbers of plotted sources. The values on *y*-axis are absolute magnitudes (corrected for distance).

(The complete figure set (9 images) is available.)

properties of individual YSOs that are uncommon between the SPCM and Pub catalogs (properties of individual unique SPCMs can be found in the SPCM source atlas, Appendix B). Our principal interest is the differences between the total numbers, spatial distributions, and IR magnitudes of the entire SPCM and Pub YSO populations.

For this analysis, we choose previous YSO studies from the literature that clearly define membership lists and include YSO selection using MIR-*Spitzer* data, often with the addition of X-ray *Chandra* and optical data. A summary of such studies is given in Table 9.

Table 9 shows that previous *Spitzer* and *Chandra* YSO catalogs are available for 20 and 12 SFiNCs SFRs, respectively (see Column 5 in the table). For ten SFiNCs SFRs (Be 59, SFO 2, NGC 2068-2071, GGD 12-15, RCW 120, Serpens South, IC 5146, NGC 7160, LDN 1251B, Cep C) X-ray YSO catalogs are published here for the first time. For RCW 120 and Be59, both MIR-*Spitzer* and ACIS-*Chandra* YSO catalogs are published here for the first time.

Column 8 in Table 9 gives the contribution of SPCM to the increase in the census of YSOs in the SFiNCs SFRs. This number ranges widely: several percent in IC 348, Cep OB3b, and ONC Flank S; from ~30% to 80% for the majority of the regions; to more than 100% in LDN 1251B, Cep A, Be59, and RCW 120. The total census increase in 20 SFiNCs SFRs (disregarding Be 59 and RCW 12), relative to the previously published *Spitzer* and *Chandra* YSO catalogs, is 26%. The total census increase for all 22 SFiNCs SFRs (including Be 59 and RCW 120) is 40%.

Figure 17 shows the spatial distributions of all SPCM and Pub YSOs. For most of the SFiNCs SFRs, the SPCM and Pub surveys have comparable spatial coverage sizes (Column 7 in Table 9). The SPCM field of view is significantly larger for Mon R2 and Cep A, and is noticeably smaller for NGC 1333, NGC 7160, and Cep OB3b. The spatial distributions of SPCMs are generally consistent with those of Pubs. Significant differences in YSO distributions are readily noticed for the SFiNCs SFRs that lack Pub X-ray YSOs, such as SFO 2, NGC 2068-2071, GGD 12-15, IC 5146, NGC 7160, LDN 1251B, and Cep C. In these SFRs, many diskless SPCMs, which often lie projected outside the SFiNCs clouds, represent newly discovered YSO populations.

While Figures 10 through 15 present IR magnitudes and colors for all SPCMs, with and without Pub counterparts, Figure 18 shows MIR color–magnitude diagrams for the YSOs that are uncommon between the SPCM and Pub catalogs. These color–color and color–magnitude diagrams suggest that the vast majority of the unique SPCM and Pub YSOs are relatively faint MIR sources, possibly either lower mass and/or higher absorbed members of the regions. In several exceptional cases (NGC 1333, IC 348, sub-regions in Orion, Serpens Main, NGC 7160, and Cep OB3b), some of the unique Pub YSOs are relatively bright MIR sources; these are located mainly outside the boundaries of the SPCM-ACIS fields.

Table 9
Comparison between SPCM and Previously Published Catalogs

Region (1)	SPCM # sources (2)	Pub Ref. (3)	Pub # sources (4)	IR_Xray Flag (5)	SPCM-Pub # sources (6)	FOV Flag (7)	Census Increase % (8)
NGC 7822 (Be59)	626	…	…	…	…	…	…
IRAS 00013+6817 (SFO 2)	71	Gu09	48	10	44	C	56
NGC 1333	181	Lu16	203	11	155	S	13
IC 348	396	Lu16	478	11	367	C	6
LkHα 101	250	Wo10	211	11	200	C	24
NGC 2068-2071	387	Me12	273	10	254	C	49
ONC Flank S	386	Me12, Ra04	281, 190, (384)	11	256, 186, (354)	C	8
ONC Flank N	327	Me12, Ra04	217, 166, (311)	11	203, 160, (295)	C	10
OMC 2-3	530	Me12, Ts02	394, 108, (443)	11	355, 101, (389)	C	32
Mon R2	652	Gu09, Na03	235, 290, (426)	11	229, 281, (411)	L	57
GGD 12-15	222	Gu09	119	10	119	C	86
RCW 120	420	…	…	…	…	…	…
Serpens Main	159	Wi07	137	11	110	C	36
Serpens South	645	Po13	666	10	542	C	15
IRAS 20050+2720	380	Gu12	330	11	286	C	28
Sh 2-106	264	Gu09, Gi04	79, 93, (158)	11	76, 85, (146)	C	75
IC 5146	256	Gu09	149	10	148	C	72
NGC 7160	143	Si06	132	10	21	S	92
LDN 1251B	49	Ev03	21	10	19	C	143
Cep OB3b	1636	Al12	2575	11	1487	S	6
Cep A	335	Gu09, Pr09	96, 29, (113)	11	92, 28, (101)	L	207
Cep C	177	Gu09	114	10	109	C	60

Note. Column 1: SFR. Column 2: total number of the SPCM sources. Column 3: literature references to the previous YSO catalogs. Column 4: total number of YSOs from the previous catalog(s). In the case of two separate previous catalogs, the numbers age given for both catalogs, as well as for the merged catalog removing duplicate sources. For the merged catalog, the number is in parenthesis. Column 5: flag indicating the type of the previous YSO catalog(s): "10"—IR without X-ray, "11"—IR and X-ray. Column 6: number of source matches between SPCM and the previous catalog(s). As for Column 4, the numbers for the merged catalogs are given in parenthesis. Column 7: flag comparing the fields of view: "C"—both SPCM and the previous catalog(s) have fields of view of a comparable size, "S"—the SPCM field of view is smaller, "L"—the SPCM field of view is larger. Column 8: the increase in the census of YSOs by SFiNCs relative to the previous studies (in %): (Col.2 − Col.6)/Col.4. Reference code in Column 3:, Al12 (Allen et al. 2012), Ev03 (Evans et al. 2003), Gi04 (Giardino et al. 2004), Gu09 (Gutermuth et al. 2009), Gu12 (Günther et al. 2012), Lu16 (Luhman et al. 2016), Me12 (Megeath et al. 2012), Na03 (Nakajima et al. 2003), Po13 (Povich et al. 2013), Pr09 (Pravdo et al. 2009), Ra04 (Ramírez et al. 2004), Si06 (Sicilia-Aguilar et al. 2006), Ts02 (Tsujimoto et al. 2002), Wi07 (Winston et al. 2007), and Wo10 (Wolk et al. 2010).

6. Limitations and Advantages of the SFiNCs SPCM Sample

The SFiNCs SPCM sample is prone to the following known limitations.

1. As in MYStIX, here we omitted the usage of the MIPS data (Section 4.1). This leads to the inability to identify some fraction of protostellar objects, especially those that lack [3.6] and [4.5] measurements. This also results in the loss of some fraction of transition disk objects, especially those that were not detected in X-rays.
2. While extragalactic background objects and the bulk of foreground stars were successfully removed from the SPCM sample, the X-ray part of the sample is still subject to contamination from Galactic field stars, mainly background stars. It is hard to identify background stars since their IR and X-ray properties considerably overlap with those of YSOs (Broos et al. 2013). Nevertheless, based on the results of the contamination simulations given in Section 3.6, one can reasonably guess that the typical number of expected Galactic field X-ray stars with 2MASS counterparts should not exceed several tens of stars per $17' \times 17'$ field. The median number of SPCMs per $17' \times 17'$ SFiNCs field is 250 YSOs with interquartile range [165–400] YSOs (Table 7 or Figure 7). A few to several foreground stellar contaminants per $17' \times 17'$ SFiNCs field have already been identified and removed (Section 4.1). This suggests that less than a few percent of the SFiNCs SPCMs could be Galactic field contaminants.
3. The IRAC-selected subsample of the SFiNCs SPCMs is generally deeper toward lower mass YSOs than the ACIS selected subsample (Section 3.4). In future SFiNCs studies, care must be taken to account for the unseen YSO populations using the XLF/IMF analyses similar to those of Kuhn et al. (2015b).

Compared to the previously published YSO samples for the SFiNCs SFRs, our SFiNCs SPCM sample has the following two main advantages.

1. SFiNCs offers a consistent treatment of IR and X-ray data sets across 22 SFRs (Sections 3, 4). It provides a uniform and comprehensive database of SFiNCs cluster members and their properties, which is suitable for further comparison across all SFiNCs SFRs and with MYStIX.
2. As in MYStIX, the SFiNCs samples are advantageous by inclusion of YSOs both with and without disks. For 10 SFiNCs SFRs, the lists of X-ray YSOs are published here for the first time (Section 5). These include 1,000 new diskless PMS stars. For two of these regions (RCW 120 and Be 59), both MIR-*Spitzer* and

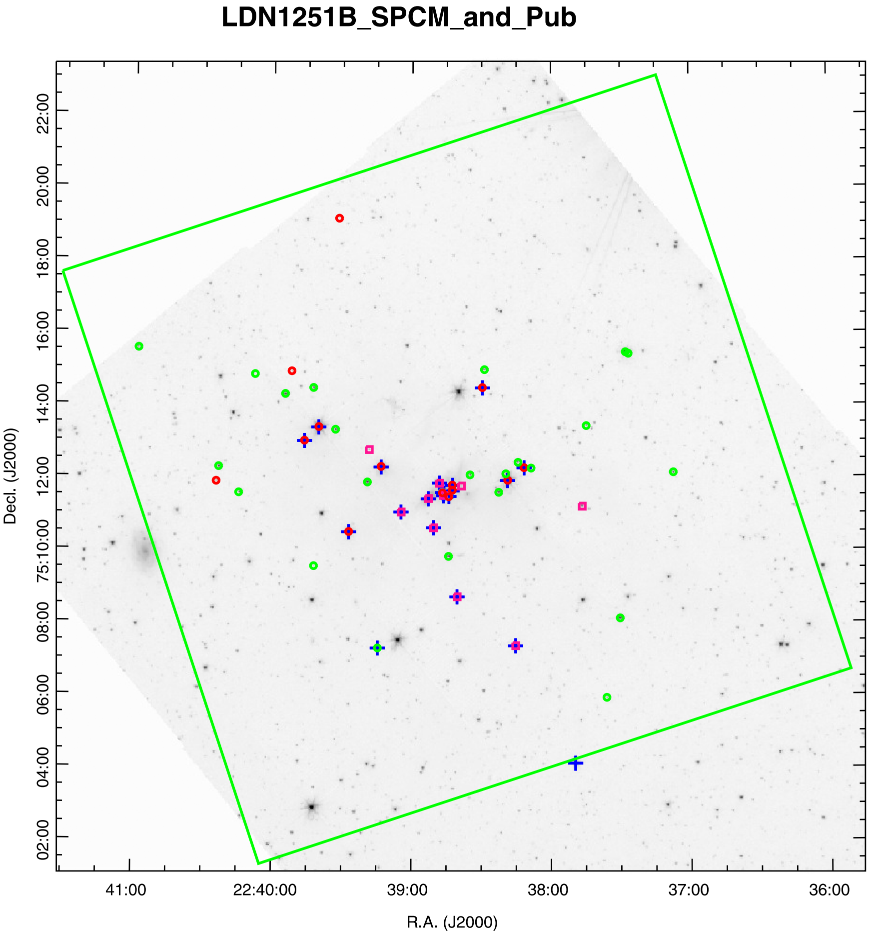

Figure 17. SPCMs (green, red, pink, cyan, and blue circles) and YSOs from previously published catalogs (blue +) superimposed on the low-resolution IRAC-[3.6] images. SPCM's colors and numbers are similar to Figure 7. An example is given for the LDN 1251B SFR. The figure set presenting other SFiNCs SFRs is available in the online journal; this omits Be 59 and RCW 120 due to the absence of previous IR/X-ray YSO catalogs. The images are shown in inverted colors with logarithmic scales. *Chandra*-ACIS-I field of view is outlined by the green polygons.

(The complete figure set (20 images) is available.)

ACIS-*Chandra* YSO catalogs are published here for the first time.

7. Summary

This paper presents the homogeneous data and YSO membership analyses as well as tabulated results for a large number of *Chandra*-ACIS and *Spitzer*-IRAC sources across the 22 nearby SFiNCs SFRs for further comparison with our earlier MYStIX survey of richer and more distant regions.

The MYStIX-based data reduction and catalog production methods were applied to the 65 *Chandra*-ACIS and 423 *Spitzer*-IRAC observations of the SFiNCs SFRs, resulting in the tables of the source properties for over 15,300 X-ray and 1,630,000 IR point sources (Section 3 and Tables 3, 4, and 6).

Unlike the MYStIX SFRs, most of the SFiNCs SFRs are high-Galactic latitude regions, where the Galactic field star contamination is greatly reduced. This allowed us to use simpler (than MYStIX) IR and X-ray YSO classification schemes based on the approaches of Gutermuth et al. (2009) and Getman et al. (2012). These classifications yield 8492 SFiNCs probable cluster members (SPCMs). The properties of the SPCMs are reported here in the form of the tables (Section 4, Tables 7 and 8), maps of sources distributions (Figure 7), and the visual atlas with various source's characteristics (Appendix B). Due to both the closer distances and reduced field star crowding, the 2MASS survey provides sufficient depth and resolution for SFiNCs PMS stars, whereas the deeper and higher resolution UKIDSS survey was often needed for MYStIX. Comparison with the previously published *Spitzer* and *Chandra* YSO catalogs shows that the SPCM list increases the census of the IR/X-ray member populations by 6%–200% for individual SFRs and by 40% for the merged sample of all 22 SFiNCs SFRs (Section 5).

The uniform and comprehensive database of SFiNCs probable cluster members serves as a foundation for various future SFiNCs/MYStIX-related studies, including such topics as identification and apparent properties of SFiNCs subclusters, age and disk fraction gradients, intrinsic physical properties of the SFiNCs subclusters and their comparison with those of MYStIX, star formation histories in the SFiNCs and MYStIX SFRs, and dynamical modeling of the SFiNCs/MYStIX subclusters.

We thank the anonymous referee for his time and many useful comments that improved this work. We thank Kevin

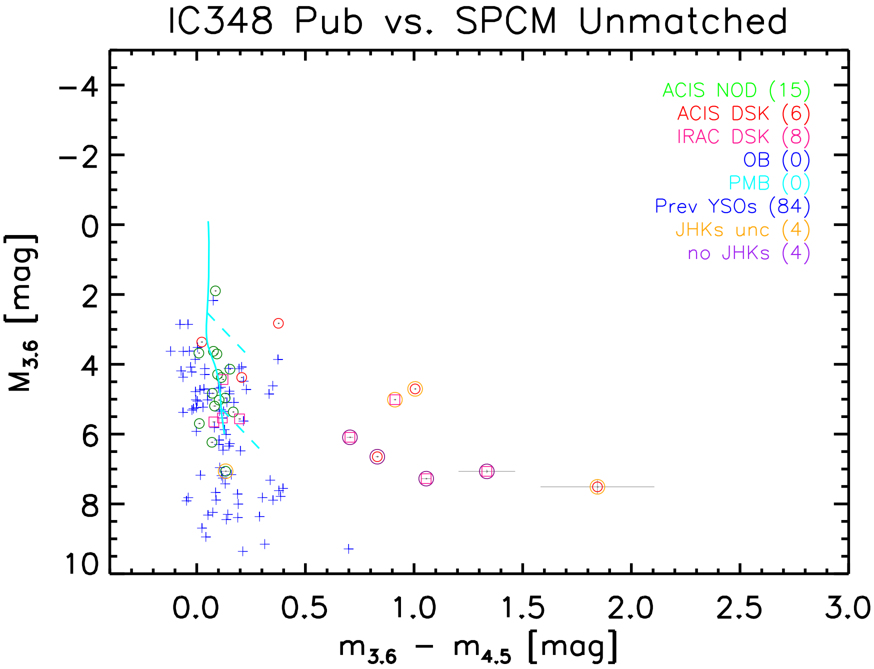

Figure 18. IRAC MIR color–magnitude diagrams in [3.6] and [4.5] for the YSOs that are uncommon between the SPCM and previously published catalogs (Table 9). An example is given for the IC 348 SFR. The figure set presenting other SFiNCs SFRs is available in the online journal; this omits Be 59 and RCW 120 due to the absence of previous IR/X-ray YSO catalogs. YSOs from the previous YSO catalogs are marked by blue crosses. SPCM sources are color-coded according to their YSO class: IRAC disky (pink squares), ACIS disky (red circles), ACIS diskless (green circles), PMBs (cyan circles), and OB-type stars (blue circles). Sources that have uncertain NIR magnitudes are additionally marked by large orange circles (one or more NIR magnitudes are often upper limits) and sources without 2MASS counterparts are marked by large purple circles. For every SFiNCs SFR, the solid cyan curve represents the smoothed version of the locus of the IC 348 diskless SPCMs. The reddening vectors of $A_K = 2$ mag (using the extinction law from Flaherty et al. 2007), originating from the IC 348 locus at ∼1 and 0.1 $M_\odot$ (according to the 3 Myr PMS models of Baraffe et al. 2015), are shown as dashed cyan lines. For SPCMs, the uncertainties on the [3.6] and [4.5] magnitudes are shown as gray error bars. The legends indicate the numbers of plotted sources. The values on *y*-axis are absolute magnitudes (corrected for distance).

(The complete figure set (20 images) is available.)

Luhman for assistance with data analysis. The SFiNCs project is supported at Penn State by NASA grant NNX15AF42G, *Chandra* GO grant SAO AR5-16001X, *Chandra* GO grant GO2-13012X, *Chandra* GO grant GO3-14004X, *Chandra* GO grant GO4-15013X, *Spitzer* GO program 90179, and the *Chandra*-ACIS Team contract SV474018 (G. Garmire & L. Townsley, Principal Investigators), issued by the *Chandra* X-Ray Center, which is operated by the Smithsonian Astrophysical Observatory for and on behalf of NASA under contract NAS8-03060. The Guaranteed Time Observations (GTO) included here were selected by the ACIS Instrument Principal Investigator, Gordon P. Garmire, of the Huntingdon Institute for X-Ray Astronomy, LLC, which is under contract to the Smithsonian Astrophysical Observatory; Contract SV2-82024. This research made use of data products from the *Chandra* Data Archive and the *Spitzer Space Telescope*, which is operated by the Jet Propulsion Laboratory (California Institute of Technology) under a contract with NASA. This research used data products from the Two Micron All Sky Survey, which is a joint project of the University of Massachusetts and the Infrared Processing and Analysis Center/California Institute of Technology, funded by the National Aeronautics and Space Administration and the National Science Foundation. This research has also made use of NASA's Astrophysics Data System Bibliographic Services and SAOImage DS9 software developed by Smithsonian Astrophysical Observatory, and the SIMBAD database (operated at CDS, Strasbourg, France).

Appendix A
Comparison of the X-Ray and MIR Fluxes between SFiNCs and Previously Published Catalogs

The previously published catalogs are abbreviated here as Pub. The measurements of intrinsic (corrected for absorption) X-ray fluxes and X-ray column densities were previously reported for 12 and 7 SFiNCs SFRs, respectively. The comparison of the column densities and fluxes between SFiNCs and Pub is presented in Figures 19 and 20 and Table 10. Two important results are evident from this analysis.

First, both Figures 19 and 20 show clear column density (N_H) and flux ($F_{\rm tc}$) biases. The SFiNCs column densities are generally higher (>40%) than the Pub densities. The SFiNCs fluxes are systematically (>30%) higher than the Pub fluxes. For the vast majority of the Pub sources their N_H and $F_{\rm tc}$ estimates were derived by fitting the data with a one-temperature thermal plasma model using the *XSPEC* (Arnaud 1996) or *Sherpa* (Freeman et al. 2001) packages. Meanwhile, the SFiNCs N_H and $F_{\rm tc}$ measurements were obtained with *XPHOT* using more realistic two-temperature plasma models (Getman et al. 2010). A situation analogous to the SFiNCs-Pub N_H bias can be found in Maggio et al. (2007), where the authors were improving the spectral fits of ∼150 X-ray bright PMS stars in Orion Nebula Cluster by substituting the one- and two-temperature (1T/2T) plasma model fits of Getman et al. (2005) with more realistic two- and three-temperature (2T/3T) model fits. The column densities from the

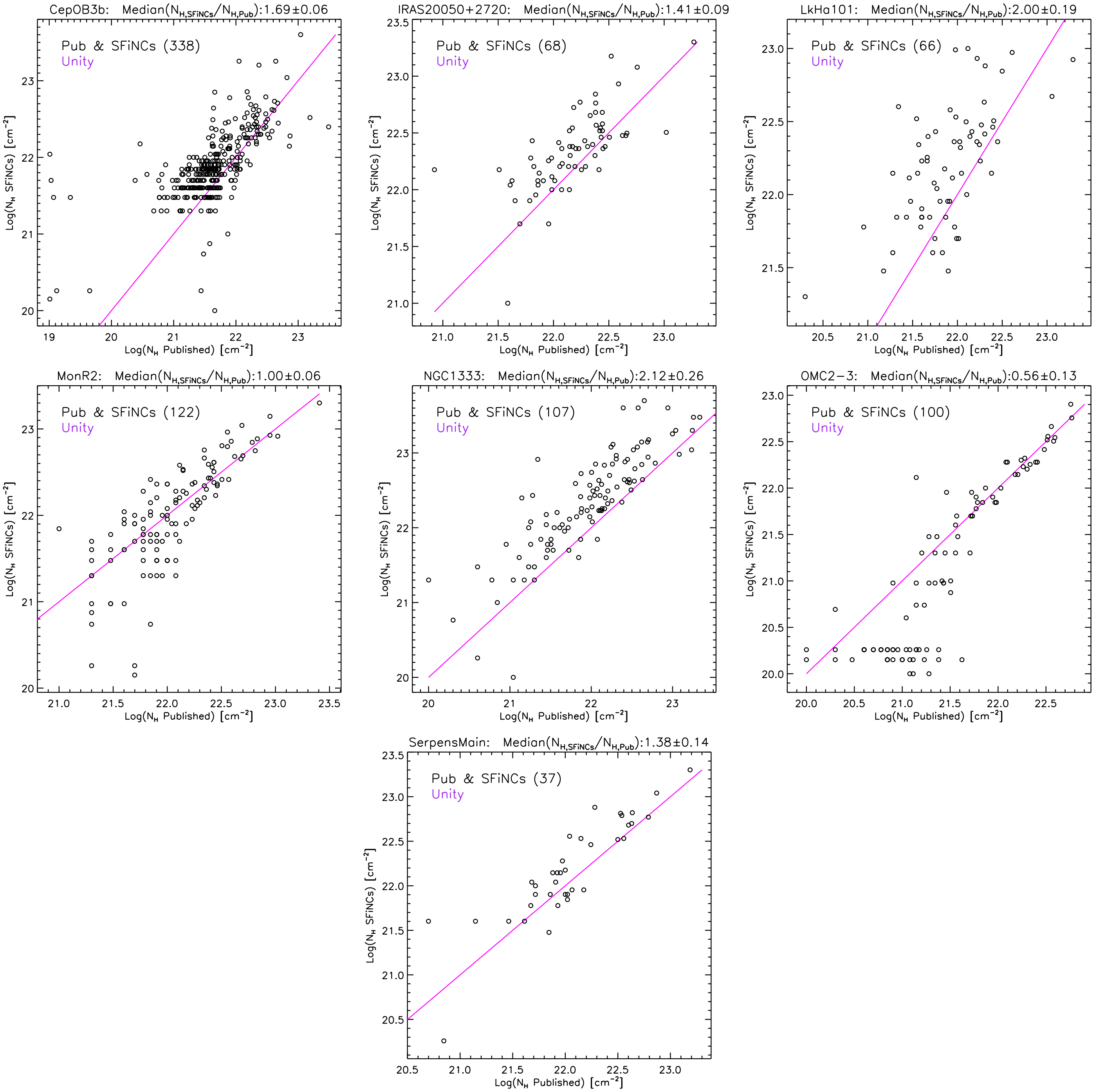

Figure 19. Comparison of the X-ray column densities (N_H) between SFiNCs and previously published catalogs. N_Hs were previously reported for seven SFiNCs SFRs. Sources common between SFiNCs and Pub are shown in black. A handful of Pub sources with the reported N_H values of 0 cm^{-2} were omitted from the analysis. Unity lines are shown in magenta. The median of the N_H ratio between the two catalogs is given in the figure title, as well as in Table 10. The figure legends give the numbers of plotted sources.

2T/3T fits were systematically larger by 0.1 dex (Figure 4 in Maggio et al. 2007). Another example of a systematic increase in flux and column density with the choice of more reasonable X-ray PMS models can be found in (Güdel et al. 2007, their Figures 7 and 8), where for over 100 Taurus PMS stars the authors compare the X-ray spectral results between the traditional 1- and 2-T model fits and the fits with more realistic distributions of the differential emission measure.

Further, it is interesting to note that the choice of the thermal plasma emission model (for instance, MEKAL versus APEC) for the same number of model components appears to have a negligible effect on the N_H outcome (Figure 7(a) in Hasenberger et al. 2016). The choice of the adopted Solar abundances would affect N_H estimates (Figure 7(b) in Hasenberger et al. 2016), but all Pub studies use the same solar abundance table (Anders & Grevesse 1989) that *XPHOT* is calibrated to; and the value of coronal metal abundance is generally similar across the Pub studies (0.3 of solar photospheric abundances) and is consistent with that of *XPHOT*. Based on these lines of evidence, we believe that the observed N_H and F_{tc} biases between SFiNS and

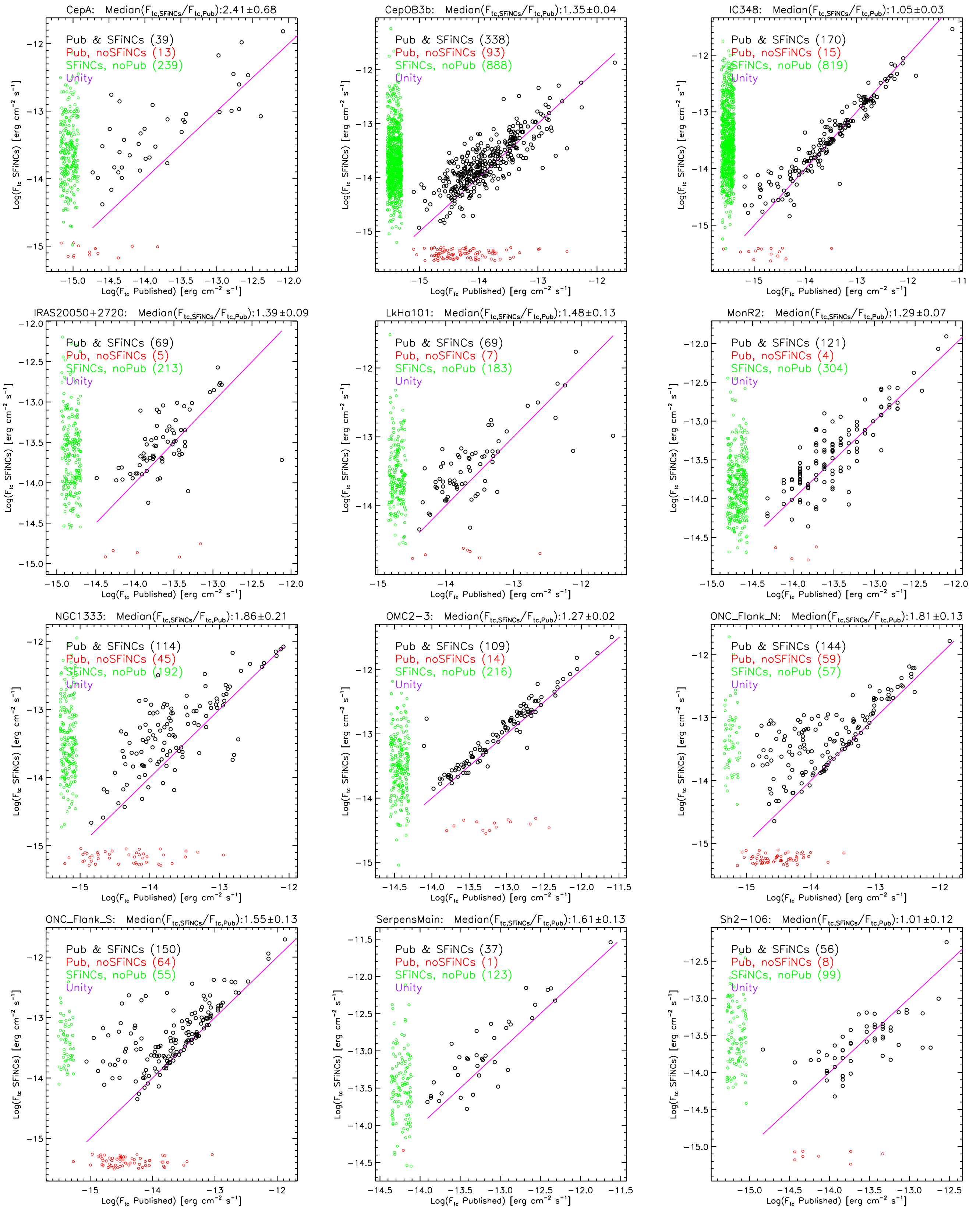

Figure 20. Comparison of the intrinsic X-ray fluxes between SFiNCs and previously published catalogs. Intrinsic X-ray fluxes were previously reported for 12 SFiNCs SFRs. Sources that are common between the two catalogs are shown in black. The unique SFiNCs sources with available SFiNCs flux estimates are in green and unique previously published sources with available Pub flux estimates are in red. Unity lines are shown in magenta. The median of the flux ratio between the two catalogs is given in the figure title, as well as in Table 10. The figure legends give the numbers of plotted sources.

Table 10
X-Ray Flux Comparison between SFiNCs and Earlier Published Catalogs

Region (1)	SFiNCs (All/ACIS-I) (sources) (2)	Pub (Total) (sources) (3)	Pub Ref (4)	SFiNCs and Pub (Matches) (sources) (5)	$N;F_{\rm tc,SFiNCs}/F_{\rm tc,Pub}$ (6)	$N;N_{H,\rm SFiNCs}/N_{H,\rm Pub}$ (7)
NGC 1333	683/671	180	Wi10	139	114; 1.86 ± 0.21	107; 2.12 ± 0.26
IC 348	1554/1534	290	St12	280	170; 1.05 ± 0.03	…
LkHα 101	581/574	213	Wo10	193	69; 1.48 ± 0.14	66; 2.00 ± 0.19
ONC Flank S	408/387	214	Ra04	204	150; 1.55 ± 0.12	…
ONC Flank N	446/421	203	Ra04	195	144; 1.81 ± 0.14	…
OMC 2-3	569/557	398	Ts02	304	109; 1.27 ± 0.02	100; 0.56 ± 0.13
Mon R2	780/764	368	Na03	359	121; 1.29 ± 0.07	122; 1.00 ± 0.06
Serpens Main	351/341	85	Wi07	79	37; 1.61 ± 0.13	37; 1.38 ± 0.14
IRAS 20050	790/781	348	Gu12	197	69; 1.39 ± 0.09	68; 1.41 ± 0.09
Sh 2-106	337/331	93	Gi04	93	56; 1.01 ± 0.11	…
Cep OB3b	2196/2148	431	Ge06	408	338; 1.35 ± 0.04	338; 1.69 ± 0.06
Cep A	530/521	52	Pr09	46	39; 2.41 ± 0.68	…
LDN 1251B	340/334	43	Si09	43	…	…
Be 59	736/736	…	…	…	…	…
SFO 2	148/148	…	…	…	…	…
NGC 2068-2071	2080/2025	…	…	…	…	…
GGD 12-15	365/359	…	…	…	…	…
RCW 120	678/678	…	…	…	…	…
Serpens South	357/347	…	…	…	…	…
IC 5146	432/408	…	…	…	…	…
NGC 7160	729/715	…	…	…	…	…
Cep C	274/270	…	…	…	…	…

Note. Previously published catalogs are abbreviated here as "Pub." Column 1: SFR. Column 2: total number of SFiNCs X-ray sources. This includes both all X-ray and ACIS-I sources only. In the remaining columns, the numbers are given for the ACIS-I sources only. Column 3: total number of Pub X-ray sources. Column 4: literature reference to the Pub catalog. Column 5: number of source matches between SFiNCs and Pub. Column 6: characterization of the SFiNCs-Pub X-ray flux bias. The column gives the number of SFiNCs-Pub sources with available flux measurements, as well as the median and its bootstrap error for the ratio of these fluxes, $F_{\rm tc,SFiNCs}/F_{\rm tc,Pub}$. Column 7: characterization of the SFiNCs-Pub X-ray column density bias. The column gives the number of SFiNCs-Pub sources with available N_H measurements, as well as the median and its bootstrap error for the $N_{H,\rm SFiNCs}/N_{H,\rm Pub}$ ratio. Reference codes in Column 4: Ge06 (Getman et al. 2006), Gi04 (Giardino et al. 2004), Gu12 (Günther et al. 2012), Na03 (Nakajima et al. 2003), Pr09 (Pravdo et al. 2009), Ra04 (Ramírez et al. 2004), Si09 (Simon 2009), St12 (Stelzer et al. 2012), Ts02 (Tsujimoto et al. 2002), Wi07 (Winston et al. 2007), Wi10 (Winston et al. 2010), and Wo10 (Wolk et al. 2010).

Pub are generally a consequence of inability of one-temperature plasma models to fully recover the soft (often unseen) component of the PMS X-ray emission (Getman et al. 2010). In the case of IC 348, where Stelzer et al. (2012) uses the *XPHOT* package to derive fluxes for the majority of their Pub sources (but not for their faintest ones), the SFiNCs-Pub bias is small.

It is also interesting to note here that the linear quantile regression analysis[11] applied to the disky and diskless SPCMs across all 22 SFiNCs SFRs (Table 8), suggests that the median N_H/A_V ratio, as a function of A_V, ranges between 1.6×10^{21} cm^{-2} mag^{-1} (Vuong et al. 2003) and 2.2×10^{21} cm^{-2} mag^{-1} (Watson 2011) and a wider N_H/A_V spread is present for the disky SPCMs (graph is not shown). Detailed analyses of the N_H/A_V ratios for the individual SFiNCs SFRs will be presented in a future SFiNCs paper.

Second, since SFiNCs produces most sensitive X-ray source catalogs and *XPHOT* allows derivation of fluxes for many faint sources, the number of unique SFiNCs sources with available flux estimates (green) is generally significantly higher than the number of unique Pub sources with available fluxes (red). However, we caution that these intrinsic *XPHOT* flux estimates are valid only in cases where the SFiNCs sources are found to be YSO members of the SFiNCs SFRs.

The comparison of the MIR IRAC magnitudes between SFiNCs and Pub is given in Figure 21 and Table 11. The IRAC photometry was previously published for 21 SFiNCs SFRs (omitting only one SFR, Be 59). Except for the RCW 120 and LDN 1251B SFRs, the previously published source catalogs are limited to YSO samples; the vast majority of these sources are relatively bright MIR sources with [3.6] > 14 mag. For the majority of the SFiNCs regions, their Pub photometry was derived using the aperture photometry tool PhotVis (Gutermuth et al. 2009, and references therein). In the case of the GLIMPSE data of RCW 120, the Pub photometry was obtained through point response function fitting (Benjamin et al. 2003). The SFiNCs-Pub magnitude differences generally have small biases and dispersions (Table 11). Typical biases are of 0.04, 0.03, 0.02, and 0.07 mag in the [3.6], [4.5], [5.8], and [8.0] bands, respectively. Typical dispersions are 0.15, 0.14, 0.16, and 0.19 mag in the [3.6], [4.5], [5.8], and [8.0] bands, respectively.

Appendix B
SPCM Source Atlas

We produce a source atlas in which some tabulated and graphical information is collected onto two pages per source.

---

[11] Description of the quantile regression analysis can be found online at https://en.wikipedia.org/wiki/Quantile_regression.

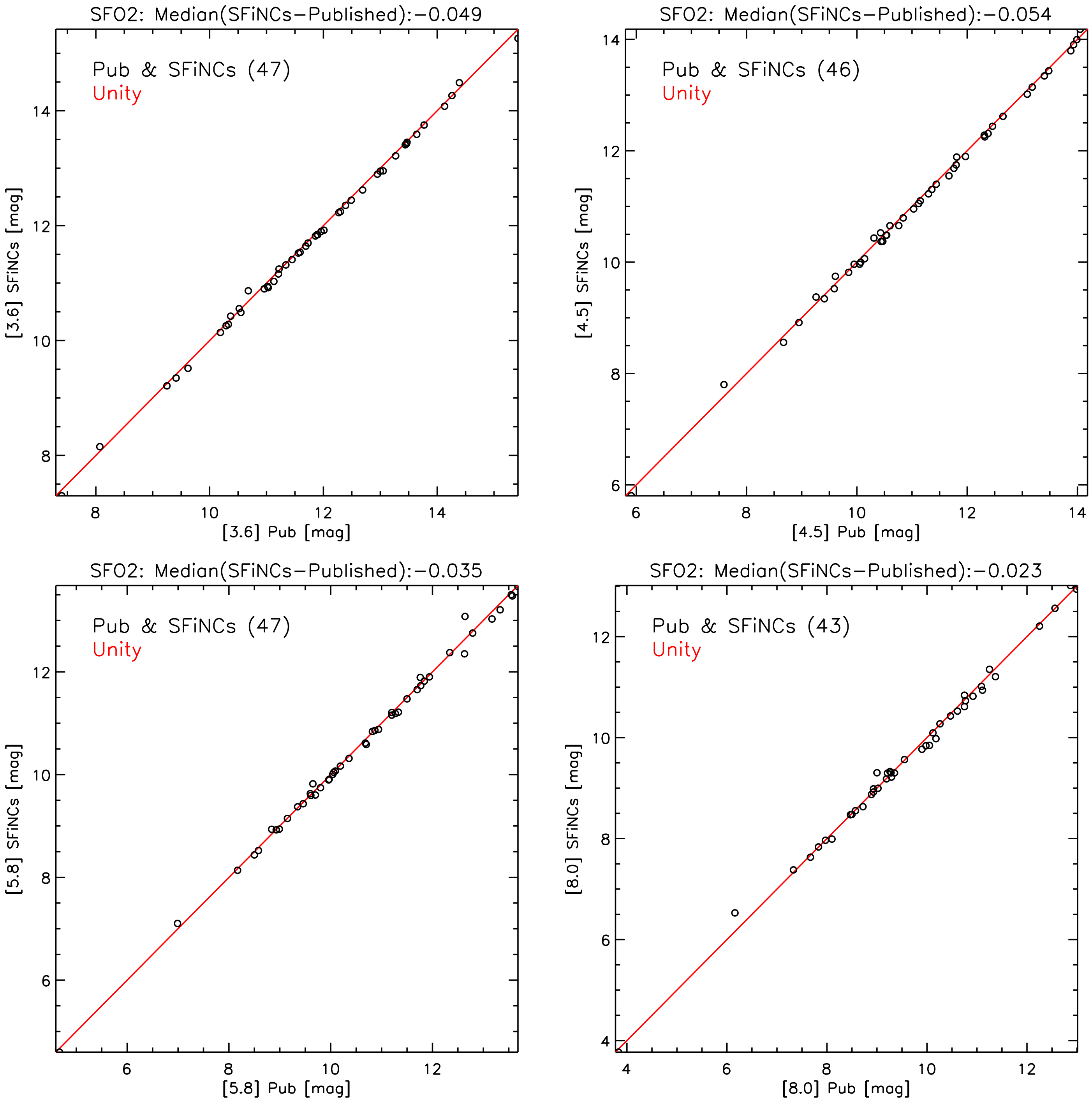

Figure 21. Comparison of the IRAC magnitudes between SFiNCs and previously published catalogs. An example is given for the SFO 2 SFR. The figure set presenting other SFiNCs SFRs with previously published IRAC photometry is available in the online journal. Unity lines are shown in red. Figure legends give the numbers of plotted sources. The median of the magnitude difference between the two catalogs is given in the figure title, whereas the mean and standard deviation of the difference are listed in Table 11.

(The complete figure set (21 images) is available.)

Figure set 22 shows a sample page for the SPCM source #1 in the LDN 1251B SFR. The graphs present various projections of the multi-dimensional SPCM data set, including the SCPM's spatial positions and X-ray/IR photometric properties.

On the first page of the atlas, the upper panel shows the map of the spatial distributions of SPCMs, similar to that of Figure 7, but with the SPCM source of interest additionally marked by orange X. This provides information on the location of the source with respect to both other YSO members and molecular cloud in the region. The bottom-left panel is similar to the X-ray color–magnitude diagram from Figure 9, but with the SPCM source of interest additionally marked by an orange square. This gives information on the X-ray photometric flux and median energy of the source as well as the comparison with the X-ray photometry of other SPCM and non-SPCM sources in the

Table 11

MIR Flux Comparison between SFiNCs and Earlier Published Catalogs

Region (1)	SFiNCs Total (sources) (2)	Pub Total (sources) (3)	Pub Ref (4)	SFiNCs and Pub Matches (sources) (5)	[3.6] N;Δm (sources; mag) (6)	[4.5] N;Δm (sources; mag) (7)	[5.8] N;Δm (sources; mag) (8)	[8.0] N;Δm (sources; mag) (9)
SFO 2	4626	48	Gu09	47	47; −0.039 ± 0.057	46; −0.029 ± 0.075	47; −0.023 ± 0.099	43; −0.019 ± 0.112
NGC 1333	10270	133	Gu09	129	128; −0.047 ± 0.151	129; −0.039 ± 0.096	127; −0.020 ± 0.099	121; −0.064 ± 0.117
IC 348	3300	307	La06	298	294; 0.011 ± 0.107	295; 0.014 ± 0.099	265; −0.078 ± 0.163	213; −0.057 ± 0.282
LkHα 101	3149	103	Gu09	103	103; −0.039 ± 0.088	102; −0.032 ± 0.096	77;0.002 ± 0.140	50; −0.074 ± 0.219
NGC 2068-2071	7686	273	Me12	269	266; −0.014 ± 0.147	267; −0.010 ± 0.127	240; −0.009 ± 0.115	224; 0.036 ± 0.156
ONC Flank S	4810	297	Me12	267	262; 0.006 ± 0.222	260; −0.014 ± 0.137	247; −0.003 ± 0.172	217; −0.134 ± 0.228
ONC Flank N	4113	228	Me12	214	214; −0.031 ± 0.109	214; −0.033 ± 0.117	195; −0.017 ± 0.140	161; −0.107 ± 0.160
OMC 2-3	5654	425	Me12	369	364; −0.015 ± 0.172	367; −0.016 ± 0.111	303; 0.001 ± 0.183	230; −0.099 ± 0.182
Mon R2	14482	235	Gu09	234	229; 0.065 ± 0.244	233; −0.016 ± 0.204	195; −0.037 ± 0.181	171; −0.076 ± 0.247
GGD 12-15	11416	119	Gu09	119	119; −0.037 ± 0.153	119; −0.045 ± 0.150	117; −0.041 ± 0.158	112; −0.080 ± 0.140
RCW 120	29061	20596	Be03	17480	17460; 0.031 ± 0.189	17450; 0.035 ± 0.222	6153; 0.067 ± 0.204	3584; 0.037 ± 0.240
Serpens Main	40691	97	Gu09	96	96; −0.041 ± 0.219	96; −0.052 ± 0.189	94; −0.043 ± 0.241	94; −0.121 ± 0.217
Serpens South	49340	666	Po13	650	650; 0.014 ± 0.160	650;−0.010 ± 0.140	633;−0.001 ± 0.117	575;−0.020 ± 0.170
IRAS 20050+2720	22971	177	Gu09	176	175; 0.128 ± 0.299	176; 0.025 ± 0.295	172; −0.010 ± 0.205	169; −0.075 ± 0.144
Sh 2-106	43543	79	Gu09	78	77; 0.031 ± 0.161	78; 0.010 ± 0.133	55; −0.002 ± 0.188	36; 0.031 ± 0.222
IC 5146	21413	149	Gu09	149	149; −0.061 ± 0.114	149; −0.057 ± 0.118	130; −0.006 ± 0.150	101; −0.084 ± 0.179
NGC 7160	24763	132	Si06	107	107; 0.073 ± 0.135	107; 0.043 ± 0.121	107; −0.024 ± 0.135	107; 0.015 ± 0.185
LDN 1251B	4392	5043	Ev03	2664	2558; 0.068 ± 0.159	2528; 0.008 ± 0.204	625; −0.036 ± 0.254	403; −0.179 ± 0.415
Cep OB3b	57065	2575	Al12	2555	2555; −0.004 ± 0.085	2555; −0.008 ± 0.084	1582; −0.031 ± 0.088	1225; −0.017 ± 0.132
Cep A	35824	96	Gu09	95	94; 0.013 ± 0.140	94; −0.023 ± 0.153	92; −0.029 ± 0.122	80; −0.114 ± 0.175
Cep C	7175	114	Gu09	113	113; −0.043 ± 0.117	113; −0.034 ± 0.102	113; 0.006 ± 0.116	108; −0.082 ± 0.103

Note. Previously published catalogs are abbreviated here as “Pub.” Column 1: SFR. Column 2: total number of sources in the SFiNCs IRAC cut-out catalogs. Column 3: total number of MIR sources in Pub. Column 4: literature reference to the Pub catalog. Column 5: number of source matches between SFiNCs and Pub. Columns 6–9: comparison of IRAC magnitudes. The column gives the number of SFiNCs-Pub sources with available magnitude estimates, as well as the mean and standard deviation of the magnitude difference, $m_{\rm SFiNCs}$–$m_{\rm Pub}$. Reference code in Column 4: Al12 (Allen et al. 2012), Be03 (Benjamin et al. 2003), Ev03 (Evans et al. 2003), Gu09 (Gutermuth et al. 2009), La06 (Lada et al. 2006), Me12 (Megeath et al. 2012), Po13 (Povich et al. 2013), and Si06 (Sicilia-Aguilar et al. 2006).

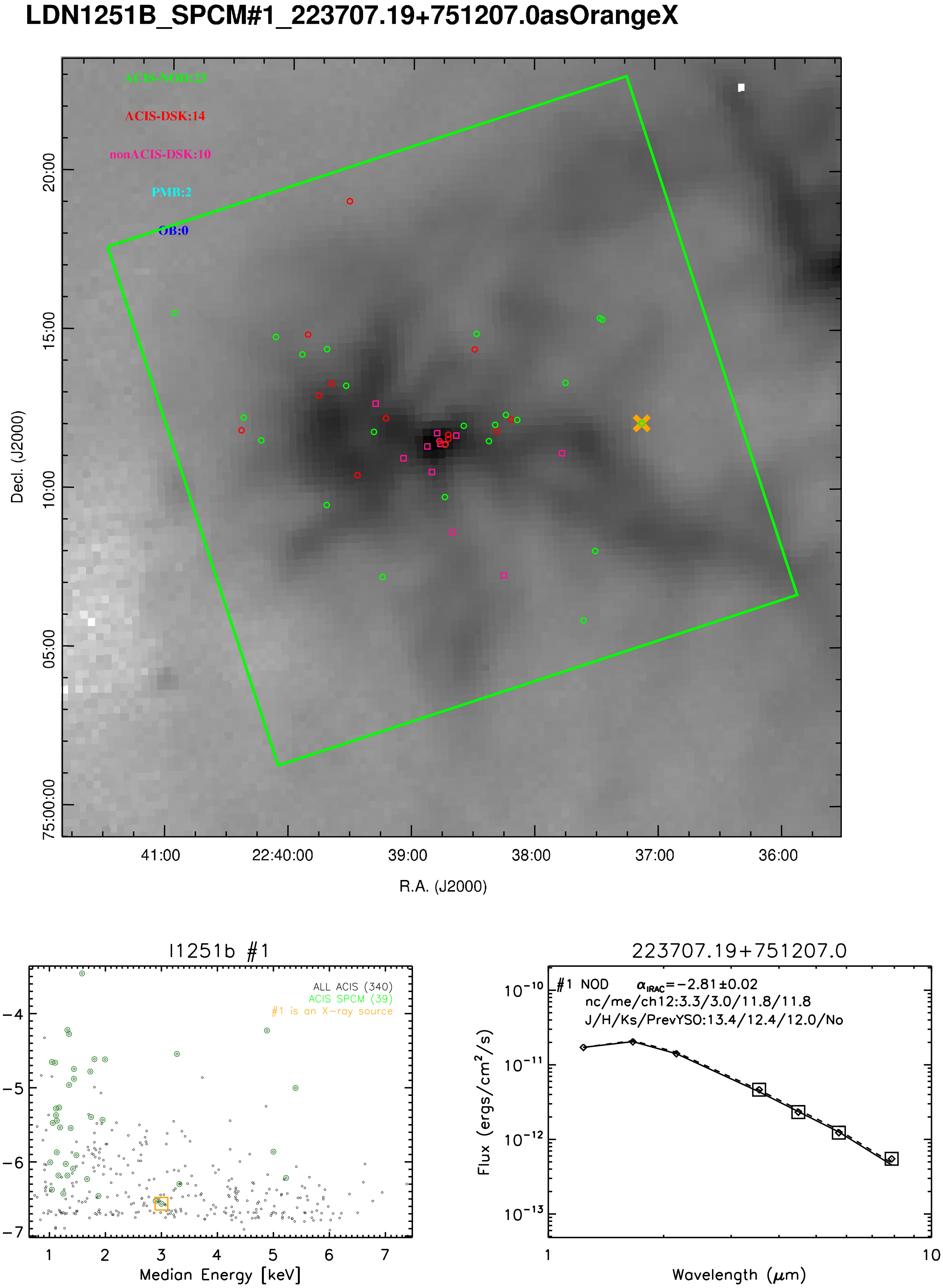

Figure 22. SPCM source atlas. An example is given here for the SPCM source #1 in LDN 1251B SFR. The entire atlas for all 8492 SPCMs is available for viewing and downloading at Zenodo (Getman et al. 2017). The description of the atlas is given in Appendix B.

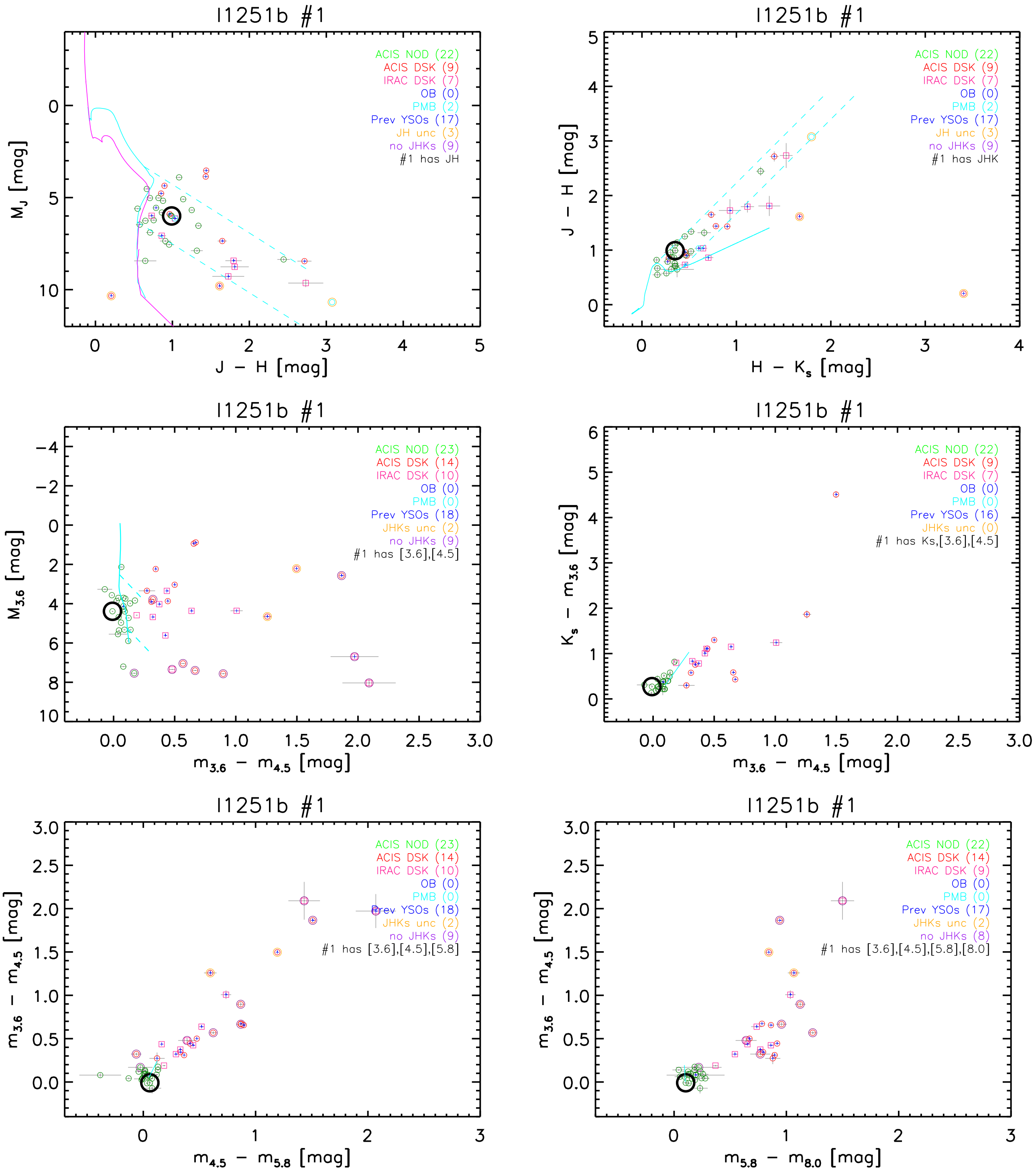

Figure 22. (Continued.)

region. The bottom-right panel presents the IR SED of the SPCM source of interest (along with the tabulated values of its apparent SED slope and disk class), similar to that of Figure 5. In this paper, IR SED is used as the primary source for distinguishing between disky and diskless YSOs (Section 4.1). The figure legends further give various useful tabulated quantities such as X-ray net counts, X-ray median energy, IR magnitudes in the *J*, *H*, K_s, [3.6], and [4.5] bands, and the flag indicating the presence/absence of a counterpart in the previously published YSO catalogs that are listed in Table 9.

On the second page of the atlas, the six panels present the IR color–magnitude and color–color diagrams from Figures 10–15, where the SPCM source of interest is additionally marked by a large black circle. On these diagrams, the information on the location of the source of interest with respect to other SPCMs and to the expected theoretical loci of YSOs helps us to elucidate the nature of the source (typically, a foreground star versus a YSO member), reaffirm its disk classification derived from the SED analysis, infer its approximate mass and absorption values, and compare the IR and X-ray (as the X-ray median energy from the previous page) absorption estimates.

For all 8492 SPCMs, the 16984 pages of the SPCM atlas are available in PDF format at Zenodo (Getman et al. 2017).

References

Alam, S., Albareti, F. D., Allende Prieto, C., et al. 2015, ApJS, 219, 12

Allen, T. S., Gutermuth, R. A., Kryukova, E., et al. 2012, ApJ, 750, 125

Anders, E., & Grevesse, N. 1989, GeCoA, 53, 197

André, P., Men'shchikov, A., Bontemps, S., et al. 2010, A&A, 518, L102

Arnaud, K. A. 1996, adass, 101, 17

Baraffe, I., Homeier, D., Allard, F., & Chabrier, G. 2015, A&A, 577, A42

Bate, M. R. 2009, MNRAS, 392, 590

Bate, M. R., Bonnell, I. A., & Bromm, V. 2003, MNRAS, 339, 577

Bell, C. P. M., Naylor, T., Mayne, N. J., Jeffries, R. D., & Littlefair, S. P. 2013, MNRAS, 434, 806

Benjamin, R. A., Churchwell, E., Babler, B. L., et al. 2003, PASP, 115, 953

Bonnell, I. A., Bate, M. R., & Vine, S. G. 2003, MNRAS, 343, 413

Bressan, A., Marigo, P., Girardi, L., et al. 2012, MNRAS, 427, 127

Broos, P., Townsley, L., Getman, K., & Bauer, F. 2012, AE: ACIS Extract, Astrophysics Source Code Library, ascl:1203.001

Broos, P. S., Getman, K. V., Povich, M. S., et al. 2013, ApJS, 209, 32

Broos, P. S., Townsley, L. K., Feigelson, E. D., et al. 2010, ApJ, 714, 1582

Broos, P. S., Townsley, L. K., Feigelson, E. D., et al. 2011, ApJS, 194, 2

Cardelli, J. A., Clayton, G. C., & Mathis, J. S. 1989, ApJ, 345, 245

Clarke, C. J., Bonnell, I. A., & Hillenbrand, L. A. 2000, in Protostars and Planets IV, ed. V. Mannings, A. Boss, & S. S. Russell (Tucson, AZ: Univ. Arizona Press), 151

Contreras, M. E., Sicilia-Aguilar, A., Muzerolle, J., et al. 2002, AJ, 124, 1585

Dunham, M. M., Allen, L. E., Evans, N. J., II, et al. 2015, ApJS, 220, 11

Dzib, S., Loinard, L., Mioduszewski, A. J., et al. 2010, ApJ, 718, 610

Dzib, S., Loinard, L., Rodríguez, L. F., Mioduszewski, A. J., & Torres, R. M. 2011, ApJ, 733, 71

Evans, N. J., II, Allen, L. E., Blake, G. A., et al. 2003, PASP, 115, 965

Fazio, G. G., Hora, J. L., Allen, L. E., et al. 2004, ApJS, 154, 10

Feigelson, E. D. 1996, ApJ, 468, 306

Feigelson, E. D., & Montmerle, T. 1999, ARA&A, 37, 363

Feigelson, E. D., Townsley, L. K., Broos, P. S., et al. 2013, ApJS, 209, 26

Flaherty, K. M., Pipher, J. L., Megeath, S. T., et al. 2007, ApJ, 663, 1069

Freeman, P., Doe, S., & Siemiginowska, A. 2001, Proc. SPIE, 4477, 76

Freeman, P. E., Kashyap, V., Rosner, R., & Lamb, D. Q. 2002, ApJS, 138, 185

Gaia Collaboration, Brown, A. G. A., Vallenari, A., et al. 2016, A&A, 595, A2

García-Rojas, J., Simón-Díaz, S., & Esteban, C. 2014, A&A, 571, A93

Garmire, G. P., Bautz, M. W., Ford, P. G., Nousek, J. A., & Ricker, G. R. 2003, Proc. SPIE, 4851, 28

Getman, K., Broos, P., Kuhn, M., et al. 2017, Star Formation In Nearby Clouds (SFiNCs): X-ray And Infrared Source Catalogs And Membership. SPCM Atlas Data Set, Zenodo, doi:10.5281/zenodo.345398

Getman, K. V., Broos, P. S., Feigelson, E. D., et al. 2011, ApJS, 194, 3

Getman, K. V., Feigelson, E. D., Broos, P. S., Townsley, L. K., & Garmire, G. P. 2010, ApJ, 708, 1760

Getman, K. V., Feigelson, E. D., Kuhn, M. A., et al. 2014a, ApJ, 787, 108

Getman, K. V., Feigelson, E. D., & Kuhn, M. A. 2014b, ApJ, 787, 109

Getman, K. V., Feigelson, E. D., Sicilia-Aguilar, A., et al. 2012, MNRAS, 426, 2917

Getman, K. V., Feigelson, E. D., Townsley, L., et al. 2006, ApJS, 163, 306

Getman, K. V., Flaccomio, E., Broos, P. S., et al. 2005, ApJS, 160, 319

Giardino, G., Favata, F., & Micela, G. 2004, A&A, 424, 965

Giardino, G., Favata, F., Micela, G., Sciortino, S., & Winston, E. 2007, A&A, 463, 275

Grosso, N., Montmerle, T., Feigelson, E. D., & Forbes, T. G. 2004, A&A, 419, 653

Guarcello, M. G., Damiani, F., Micela, G., et al. 2010, A&A, 521, A18

Güdel, M., Briggs, K. R., Arzner, K., et al. 2007, A&A, 468, 353

Günther, H. M., Wolk, S. J., Spitzbart, B., et al. 2012, AJ, 144, 101

Gutermuth, R. A., Megeath, S. T., Myers, P. C., et al. 2009, ApJS, 184, 18

Gutermuth, R. A., Myers, P. C., Megeath, S. T., et al. 2008, ApJ, 674, 336

Hasenberger, B., Forbrich, J., Alves, J., et al. 2016, A&A, 593, A7

Herbig, G. H., & Bell, K. R. 1988, LicOB, 1111, 90

Herbst, W., Herbst, D. K., Grossman, E. J., & Weinstein, D. 1994, AJ, 108, 1906

Herbst, W. 2008, in Handbook of Star-forming Regions, Vol. I, The Northern Sky, ed. B. Reipurth (San Francisco, CA: ASP), 372

Hernández, J., Hartmann, L., Megeath, T., et al. 2007, ApJ, 662, 1067

Hills, J. G. 1980, ApJ, 235, 986

Hirota, T., Bushimata, T., Choi, Y. K., et al. 2008, PASJ, 60, 37

King, R. R., Naylor, T., Broos, P. S., Getman, K. V., & Feigelson, E. D. 2013, ApJS, 209, 28

Kruijssen, J. M. D. 2012, MNRAS, 426, 3008

Kruijssen, J. M. D., Maschberger, T., Moeckel, N., et al. 2012, MNRAS, 419, 841

Krumholz, M. R., Bate, M. R., Arce, H. G., et al. 2014, in Protostars and Planets IV, ed. H. Beuther et al. (Tucson, AZ: Univ. Arizona Press), 914

Krumholz, M. R., & Tan, J. C. 2007, ApJ, 654, 304

Kuhn, M. A., Feigelson, E. D., Getman, K. V., et al. 2014, ApJ, 787, 107

Kuhn, M. A., Feigelson, E. D., Getman, K. V., et al. 2015a, ApJ, 812, 131

Kuhn, M. A., Getman, K. V., Broos, P. S., Townsley, L. K., & Feigelson, E. D. 2013a, ApJS, 209, 27

Kuhn, M. A., Getman, K. V., & Feigelson, E. D. 2015b, ApJ, 802, 60

Kuhn, M. A., Povich, M. S., Luhman, K. L., et al. 2013b, ApJS, 209, 29

Kun, M., Kiss, Z. T., & Balog, Z. 2008, in Handbook of Star-forming Regions, Vol. I, The Northern Sky, ed. B. Reipurth (San Francisco, CA: ASP), 136

Lada, C. J. 1987, in IAU Symp. 115, Star-forming Regions, ed. M. Peimbert & J. Jugaku (Dordrecht: Reidel), 1

Lada, C. J., & Lada, E. A. 2003, ARA&A, 41, 57

Lada, C. J., Muench, A. A., Luhman, K. L., et al. 2006, AJ, 131, 1574

Luhman, K. L., Allen, L. E., Allen, P. R., et al. 2008, ApJ, 675, 1375

Luhman, K. L., Esplin, T. L., & Loutrel, N. P. 2016, ApJ, 827, 52

Maggio, A., Flaccomio, E., Favata, F., et al. 2007, ApJ, 660, 1462

Majaess, D. J., Turner, D. G., Lane, D. J., & Moncrieff, K. E. 2008, JAVSO, 36, 90

McMillan, S. L. W., Vesperini, E., & Portegies Zwart, S. F. 2007, ApJL, 655, L45

Megeath, S. T., Gutermuth, R., Muzerolle, J., et al. 2012, AJ, 144, 192

Menten, K. M., Reid, M. J., Forbrich, J., & Brunthaler, A. 2007, A&A, 474, 515

Moscadelli, L., Reid, M. J., Menten, K. M., et al. 2009, ApJ, 693, 406

Nakajima, H., Imanishi, K., Takagi, S.-I., Koyama, K., & Tsujimoto, M. 2003, PASJ, 55, 635

Naylor, T., Broos, P. S., & Feigelson, E. D. 2013, ApJS, 209, 30

Noel, B., Joblin, C., Maillard, J. P., & Paumard, T. 2005, A&A, 436, 569

Pandey, A. K., Sharma, S., Ogura, K., et al. 2008, MNRAS, 383, 1241

Povich, M. S., Kuhn, M. A., Getman, K. V., et al. 2013, ApJS, 209, 31

Pravdo, S. H., Tsuboi, Y., Uzawa, A., & Ezoe, Y. 2009, ApJ, 704, 1495

Preibisch, T., & Feigelson, E. D. 2005, ApJS, 160, 390

Preibisch, T., Kim, Y.-C., Favata, F., et al. 2005, ApJS, 160, 401

Racine, R. 1968, AJ, 73, 233

Ramírez, S. V., Rebull, L., Stauffer, J., et al. 2004, AJ, 128, 787

Richert, A. J. W., Feigelson, E. D., Getman, K. V., & Kuhn, M. A. 2015, ApJ, 811, 10

Romine, G., Feigelson, E. D., Getman, K. V., Kuhn, M. A., & Povich, M. S. 2016, ApJ, 833, 193

Schneider, N., Simon, R., Bontemps, S., Comerón, F., & Motte, F. 2007, A&A, 474, 873

Sicilia-Aguilar, A., Hartmann, L., Calvet, N., et al. 2006, ApJ, 638, 897

Sicilia-Aguilar, A., Hartmann, L. W., Briceño, C., Muzerolle, J., & Calvet, N. 2004, AJ, 128, 805

Siess, L., Dufour, E., & Forestini, M. 2000, A&A, 358, 593

Simon, T. 2009, ApJ, 694, 425

Skiff, B. A. 2009, yCat, 1, 2023

Skinner, S. L., Sokal, K. R., Megeath, S. T., et al. 2009, ApJ, 701, 710

Skrutskie, M. F., Cutri, R. M., Stiening, R., et al. 2006, AJ, 131, 1163

Stelzer, B., Preibisch, T., Alexander, F., et al. 2012, A&A, 537, A135

Telleschi, A., Güdel, M., Briggs, K. R., Audard, M., & Palla, F. 2007, A&A, 468, 425

Thum, C., Neri, R., Báez-Rubio, A., & Krips, M. 2013, A&A, 556, A129

Townsley, L. K., Broos, P. S., Corcoran, M. F., et al. 2011, ApJS, 194, 1

Townsley, L. K., Broos, P. S., Garmire, G. P., et al. 2014, ApJS, 213, 1

Tsujimoto, M., Koyama, K., Tsuboi, Y., Goto, M., & Kobayashi, N. 2002, ApJ, 566, 974

Tutukov, A. V. 1978, A&A, 70, 57
Vuong, M. H., Montmerle, T., Grosso, N., et al. 2003, A&A, 408, 581
Watson, D. 2011, A&A, 533, A16
Weisskopf, M. C., Brinkman, B., Canizares, C., et al. 2002, PASP, 114, 1
Wilking, B. A., Blackwell, J. H., Mundy, L. G., & Howe, J. E. 1989, ApJ, 345, 257
Winston, E., Megeath, S. T., Wolk, S. J., et al. 2007, ApJ, 669, 493
Winston, E., Megeath, S. T., Wolk, S. J., et al. 2009, AJ, 137, 4777
Winston, E., Megeath, S. T., Wolk, S. J., et al. 2010, AJ, 140, 266
Wolk, S. J., Winston, E., Bourke, T. L., et al. 2010, ApJ, 715, 671
Ybarra, J. E., Lada, E. A., Román-Zúniga, C. G., et al. 2013, ApJ, 769, 140
Zavagno, A., Pomarès, M., Deharveng, L., et al. 2007, A&A, 472, 835
Zinnecker, H., & Yorke, H. W. 2007, ARA&A, 45, 481